Aeroradiometric Measurements in the Framework of the Swiss Exercises ARM16 and LAURA

Gernot Butterweck, Benno Bucher, Ladislaus Rybach, Cristina Poretti,
Stéphane Maillard, Georg Schwarz, Bénédicte Hofstetter-Boillat,
Eike Hohmann, Sabine Mayer, Gerald Scharding

Aeroradiometric Measurements in the Framework of the Swiss Exercises ARM16 and LAURA

Gernot Butterweck[1], Benno Bucher[2], Ladislaus Rybach[3], Cristina Poretti[4],
Stéphane Maillard[5], Georg Schwarz[2], Bénédicte Hofstetter-Boillat[1],
Eike Hohmann[1], Sabine Mayer[1], Gerald Scharding[4]

1   Division for Radiation Safety and Security, Paul Scherrer Institute (PSI),
5232 Villigen PSI, Switzerland
2   Swiss Federal Nuclear Safety Inspectorate (ENSI), Industriestrasse 19,
5200 Brugg, Switzerland
3   Institute of Geophysics, Swiss Federal Institute of Technology Zürich (ETHZ),
8092 Zürich, Switzerland
4   Swiss National Emergency Operations Center (NEOC),
8044 Zürich, Switzerland
5   Nuclear Biological Chemical - Explosive Ordnance Disposal (NBC-EOD) Centre of Competence,
3700 Spiez, Switzerland

Abstract

The measurement flights of the exercise ARM16 were performed between June 27th and July 1st, 2016. The exercise was organized by the National Emergency Operations Centre (NEOC) under coordination from the Expert Group for Aeroradiometrics (FAR). Representatives of KompZen ABC-Kamir participated with a second Super Puma helicopter carrying the prototype of a new airborne gamma-spectroscopy system (RLL) in parts of the exercise. According to the alternating schedule of the annual ARM exercises, the environs of the nuclear power plants Beznau (KKB) and Leibstadt (KKL) and the nuclear facilities of the Paul Scherrer Institute (PSI) and the Zwischenlager Würenlingen AG (Zwilag) were surveyed. Both reactor blocks of KKB were in maintenance shutdown during the flights. The series of radiological background measurements over Swiss cities was complemented with measurements over Luzern, Emmen, Cham, Baar and Zug.

A permanent dose rate probe of the Swiss NADAM Network near Vicosoprano measures the highest values observed in this network. The vicinity of the probe was inspected with airborne gamma-spectrometry and the elevated dose rate was confirmed and could be attributed to elevated concentrations of natural radionuclides.

The emergency exercise LAURA, consisting mainly of the search for radioactive sources, was conducted at Emmen military airfield in cooperation with local first responders.

Several measuring flights were performed to test the evaluation procedures. Especially the parameters for background and altitude corrections were inspected.

Contents

List of Figures

List of Tables

1   Introduction

Swiss airborne gamma spectrometry measurements started in 1986. Methodology and software for calibration, data acquisition and mapping were developed at the Institute of Geophysics of the Swiss Federal Institute of Technology Zurich (ETHZ). Between 1989 and 1993 the environs of Swiss nuclear installations were measured annually on behalf of the Swiss Federal Nuclear Safety Inspectorate (ENSI). This schedule was changed to biannual inspections in 1994, together with an organizational inclusion of the airborne gamma-spectrometric system (ARM) into the Emergency Organization Radioactivity (EOR) of the Federal Office for Civil Protection (FOCP). The deployment of the airborne gamma-spectrometric system is organized by the National Emergency Operations Centre (NEOC). NEOC is also responsible for the recruitment and instruction of the measurement team and the operational readiness of the system. Aerial operations are coordinated and performed by the Swiss Air Force. The gamma-spectrometric equipment is stationed at the military airfield of Dübendorf. The gamma-spectrometry system can be airborne within four hours. Responsibility for scientific support, development and maintenance of the aeroradiometric measurement equipment passed from ETHZ to the Radiation Metrology Section of the Paul Scherrer Institute (PSI) in 2003 in cooperation with ENSI. General scientific coordination and planning of the annual measuring flights is provided by the Expert Group for Aeroradiometrics (FAR). FAR was a working group of the Swiss Federal Commission for NBC-protection (ComNBC) and consists of experts from all Swiss institutions concerned with aeroradiometry. FAR was re-organized as an expert group of the NEOC in 2008. Additional information can be found at `http://www.far.ensi.ch/`.

The NBC-EOD Centre of Competence (KompZen ABC-Kamir) is in the process to purchase new airborne gamma-spectroscopy systems (Radiometrie Land Luft, RLL), which are planned to replace also the old systems (ARM) employed by the National Emergency Operations Centre (NEOC).

This report focuses on methodological aspects and thus complements the short report of NEOC about the annual flight surveys (available from the NEOC website `https://www.naz.ch`).

1.1   Measuring System ARM

The measuring system ARM consists of four NaI-detectors with a total volume of 16.8 l. The measurements were performed with detector package (Detector D, Radiation Solutions RSX4) which includes digital spectrometers with a maximum resolution of 1024 channels for each detector. To render the data evaluation compatible to the old systems, the spectral resolution is reduced to 256 channels. The measurement control, data acquisition and storage are performed with an industrial grade personal computer. A second, identically configured PC is present in the electronics rack (Figure 1) as redundancy. Under normal operation conditions, this PC is used for real-time evaluation and mapping of the data. The positioning uses GPS (Global Positioning System) in the improved EGNOS (European Geostationary Navigation Overlay Service) mode. Together with spectrum and position, air pressure, air temperature and radar altitude are registered. The measuring system is mounted in an Aerospatiale AS 332 Super Puma helicopter of the Swiss Air Force (Figure 2). This helicopter has excellent navigation properties and allows emergency operation during bad weather conditions and nighttime. The detector is mounted in the cargo bay below the center of the helicopter. The cargo bay is covered with a lightweight honeycomb plate to minimize photon absorption losses.
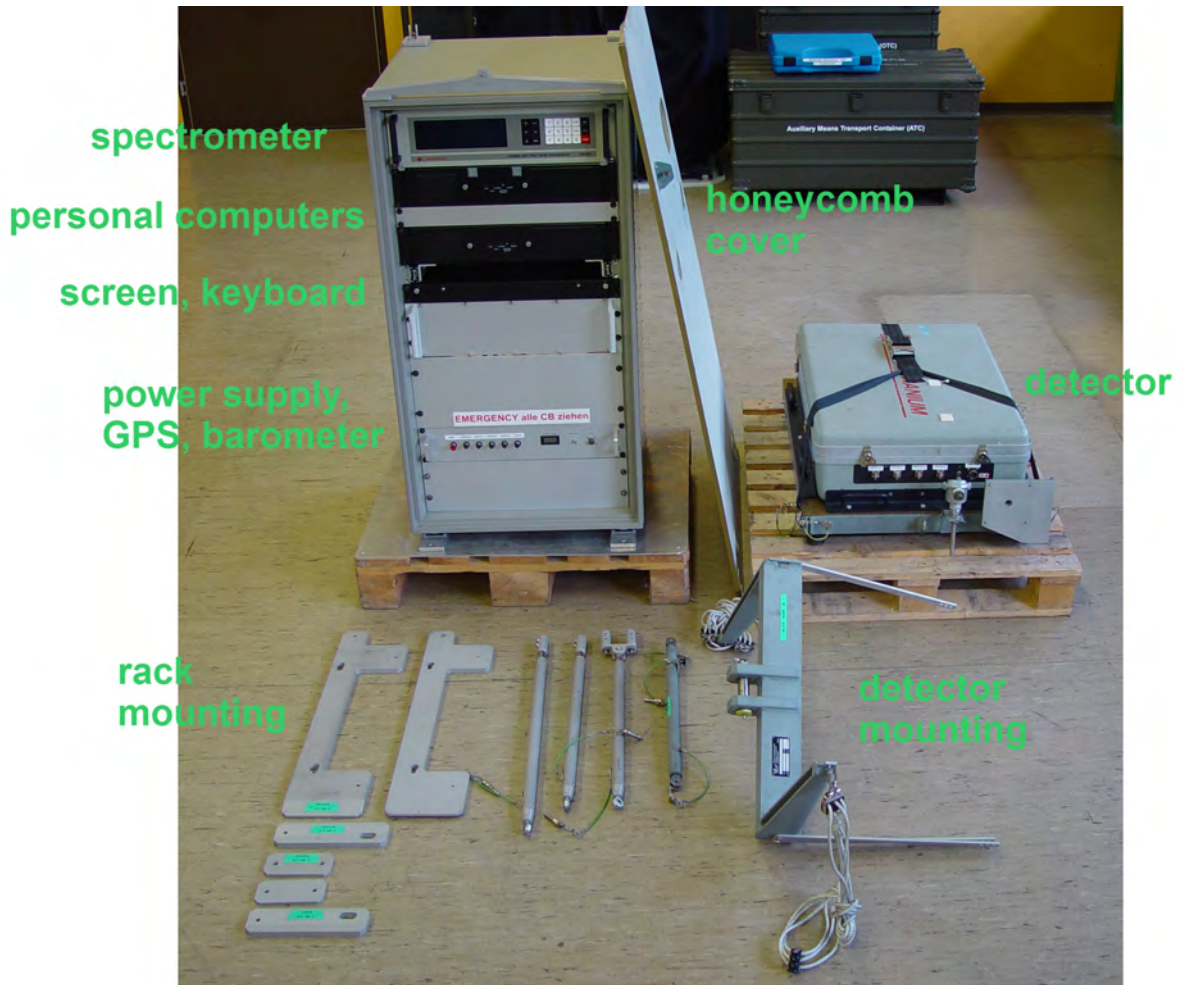
Figure 1: Measurement system of the Swiss team.

Figure 2: Super Puma helicopter of the Swiss Air Force.

1.2 Measuring System RLL

The measuring system RLL consists of four NaI (Tl) radiation detectors with volumes of four liters, associated photo-multipliers and multichannel analyzers manufactured by Mirion Technologies. Additionally, a Geiger-Müller tube with counting electronics is installed for measurements in high dose rate environments. The measuring system RLL is integrated in an Aerospatiale AS 332 Super Puma helicopter (TH 06) of the Swiss Air Force. The detectors, Geiger-Müller tube and associated electronics are installed in a thermally insulated aluminum case mounted in the cargo bay below the center of the helicopter (Fig. 3).

The RLL system uses position, air pressure, air temperature and radar altitude provided by the ARINC data bus of the helicopter. The equipment control, data acquisition and storage are performed with a military grade computer working as a data server. Two further client computers are used as operator interface for real-time evaluation, data mapping and communication. The computers are installed in an equipment rack including a battery backed-up power supply. Two operators can operate the system simultaneously with separate client computers, displays, keyboards and trackballs (Fig. 4). An additional third central display of the console is mirrored on a screen in the cockpit for information exchange with the pilots. For storage and transport of the RLL systems, special storage crates are used (Fig. 5). A dedicated tool for mounting the detector box into the storage bay is available for each system.
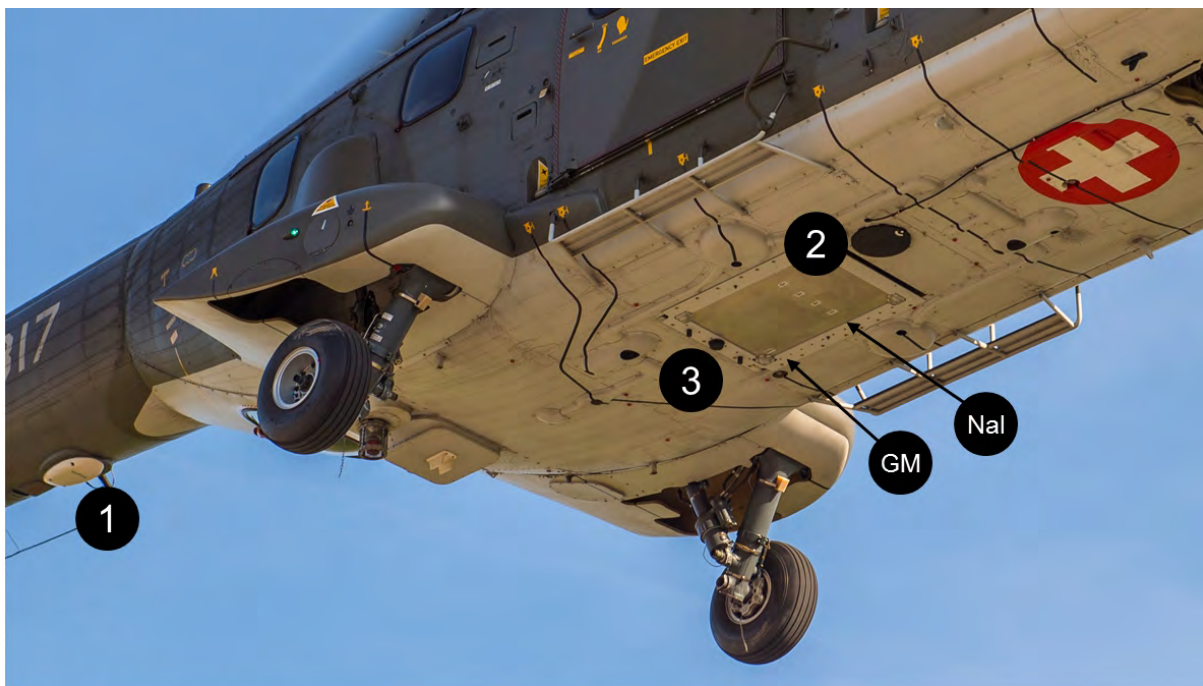
1. Radar altimeter
2. Detection container
   (with marked detector reference points)
3. UMTS antenna

Figure 3: Sensor location of the RLL system.
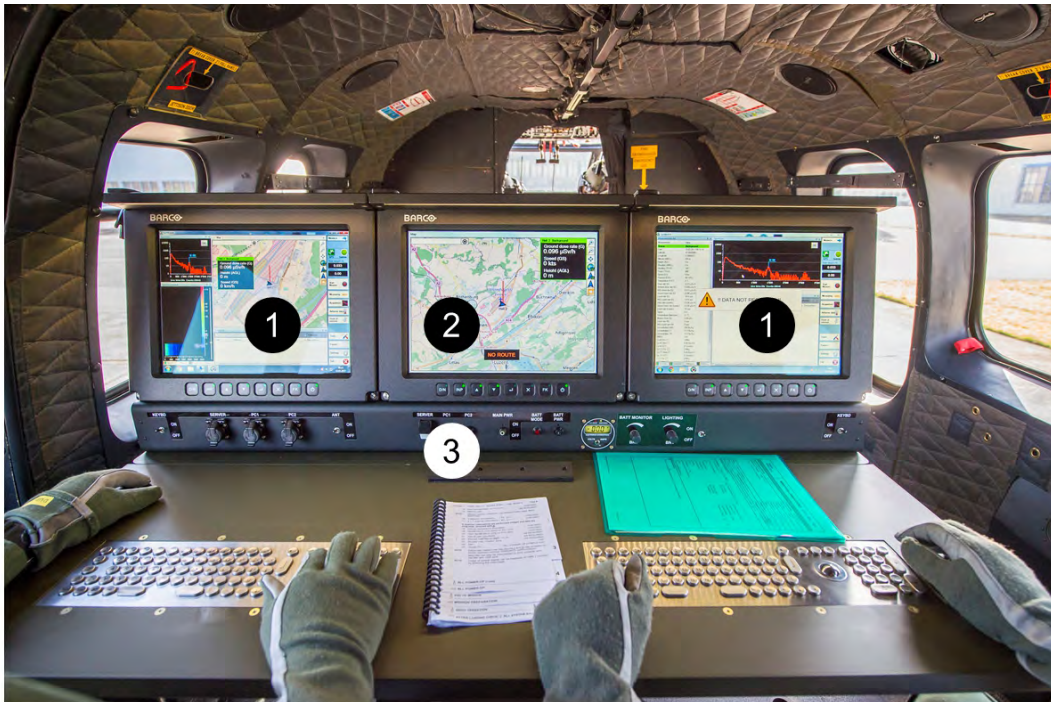
1. Display of client computers
2. Common display
3. Control panel (power, light, USB, communication…)

Figure 4: RLL console inside of the helicopter.

1. Lifting platform for detection container
2. Floor plates and accessories case
3. Monitors and operator's console
4. Detection container
5. Operators seats and equipment rack

Figure 5: RLL system packed into storage crates.

1.3 Measuring flights

The advantage of aeroradiometric measurements lies in the high velocity of measurements in a large area, even over rough terrain. Uniform radiological information of an area is obtained from a regular grid of measuring points. This grid is composed from parallel flight lines which are 100 m to 500 m apart, depending on the scope of the measurement. The flight altitude above ground is aspired to be constant during the measuring flight. Typical values lie between 50 m and 100 m above ground. The spectra are recorded in regular time intervals of typical one second, yielding integration over 28 meters of the flight line at a velocity of 100 km/h.

1.4 Data evaluation

The data evaluation follows the methodology described in Schwarz (1991). Since the year 2000, software developed by the Research Group for Geothermics and Radiometry of the Institute of Geophysics of the Swiss Federal Institute of Technology Zurich (ETHZ) with on-line mapping options (Bucher, 2001) is used.

1.5 Data presentation

A first brief report (Kurzbericht) of the measurement results is compiled by the measurement team and published immediately after the end of the exercise on the homepage of NEOC. These reports are archived at http://www.far.ensi.ch. Results of a further data evaluation are published in the form of a PSI-report. For all measuring areas, a map of the total dose rate (measuring quantity H*(10) at 1 m above ground) and the flight lines is presented together with a map of the Man-Made-Gross-Count (MMGC) ratio. A map of the ^{232}Th activity concentration (measuring quantity activity per dry mass) yields quality information as it can be expected that this quantity is constant over time. As an additional quality measure, an appendix with the basic parameters of the data evaluation is added to simplify a re-evaluation of the data in the future. If the MMGC-ratio indicates elevated values, maps of individual radionuclides are added based on the average photon spectrum over the affected area. In the case of large changes of topography in the measured area, a map of the terrestrial dose rate consisting of the total dose rate reduced of the altitude dependent cosmic component is included. In the case of measuring flights with the main purpose of mapping natural radionuclide concentrations, a supplementary map of the ^{40}K activity concentration (measuring quantity activity per wet mass) is presented. All maps use a gradual color scale from blue for low values to red for high values. The maximum and minimum values are specified in the legend together with the measurement unit of the depicted quantity. The colors for 10 percent steps between minimum and maximum values of the scale are given in Table 1. Minimum and maximum of the color scale for the measured quantity are generally set to standard values to facilitate easier comparison of maps. Maps with different value ranges are added if considered helpful to the reader.
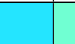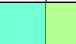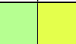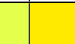
Percentage	≤0	10	20	30	40	50	60	70	80	90	≥100
Color											

Table 1: Quantification of the color scale.

2 Results of the measuring flights during the exercises ARM16 and LAURA

The flights of the exercises ARM16 and LAURA were performed with a Super Puma helicopter of the Swiss Air Force between June 27th and July 1st, 2016. Flight velocity of all measuring flights was around 30 m/s with a ground clearance of 90 m. The counting interval of the spectra was one second.

Personnel of the military unit Stab BR NAZ performed the measurements supported by experts from ENSI, PSI and NEOC. A short report of the measurement results was placed on the NEOC website `https://www.naz.ch/` on July 1st, 2016.

Representatives of KompZen ABC-Kamir participated with a second Super Puma helicopter carrying the prototype of a new airborne gamma-spectroscopy system (RLL) in parts of the exercise.

Flight parameters of the exercises ARM16 and LAURA are listed in Table 2.

Location	Flight number	Date	Measuring time [s]	Length of run [km]	Area [km^2]
KKB, KKL, PSI and Zwilag	2016011 2016012	27.6.2016	9902	467	116
Baar, Cham, Zug	2016018 2016020	28.6.2016	5018	241	61
Emmen, Luzern	2016028 2016030	30.6.2016	7453	309	97
Vicosoprano	2016016	28.6.2016	2069	74	20
Exercise LAURA	2016021 2016022 2016023	29.6.2016	818	29	1
Highway A13	2016015	28.6.2016	2532	103	-
Lake Neuchâtel	2016025	29.6.2016	407	27	-
Limpach valley	2016026	29.6.2016	548	30	-
PSI (sources)	2016013	27.6.2016	2811	105	12

Table 2: Flight data of ARM16 and LAURA.

2.1 Recurrent measurement area KKB, KKL, PSI and Zwilag

According to a biannual rotation of routine measurements, the environs of the nuclear power plants Beznau (KKB) and Leibstadt (KKL), the Paul Scherrer Institute and the intermediate storage facility Zwilag were inspected in 2016. Both reactor blocks of KKB were in maintenance shutdown during the measuring flight.

The dose rate map (Figure 6) shows elevated values over KKL and Rotbergegg, whereas KKB, PSI and Zwilag are unobtrusive. The elevated dose rate over the premises of KKL is caused by high energy photon radiation of the activation product ^{16}N, a typical result for operating boiling water reactors. The high energy photon radiation of ^{16}N leads also to misinterpretations in the maps of ^{232}Th (Figure 8).

The elevated dose rate at Rotbergegg is due to a known anomaly of the natural radionuclide ^{232}Th, which can be seen more clearly in the ^{232}Th map (Figure 8).

Additional to the premises of KKL, the map of the MMGC-ratio (Figure 7) shows elevated values near the Paul Scherrer Institute. The MMGC-ratio is an indicator for the presence of artificial radionuclides. The elevated MMGC-values observed are due to radioactive gases produced in the accelerators of the PSI West site. These gases are a controlled and permitted release from the stack of PSI West. The released gas mixture contains mainly the short-lived positron emitting Isotopes ^{15}O, ^{11}C, ^{13}N and ^{18}F. Apart from photon emissions of natural radionuclides, the annihilation radiation at 511 keV is clearly detectable in the average spectrum measured over the area with elevated MMGC-ratios (Figure 9).
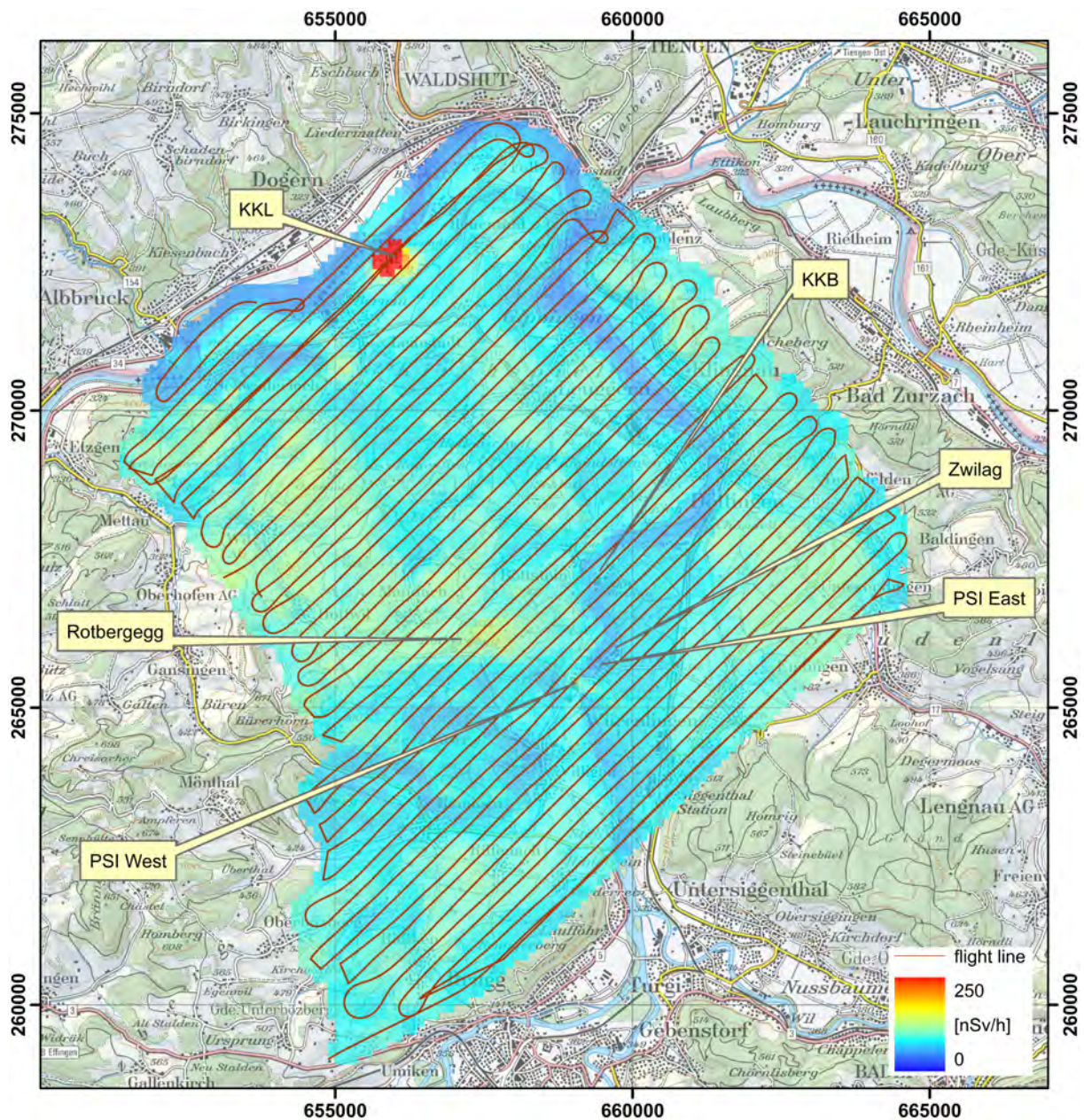
Figure 6: Dose rate in the vicinity of KKB, KKL, PSI and Zwilag.
PK100 ©2016 swisstopo (JD100042).

Figure 7: MMGC-ratio in the vicinity of KKB, KKL, PSI and Zwilag.
PK100 ©2016 swisstopo (JD100042).

8
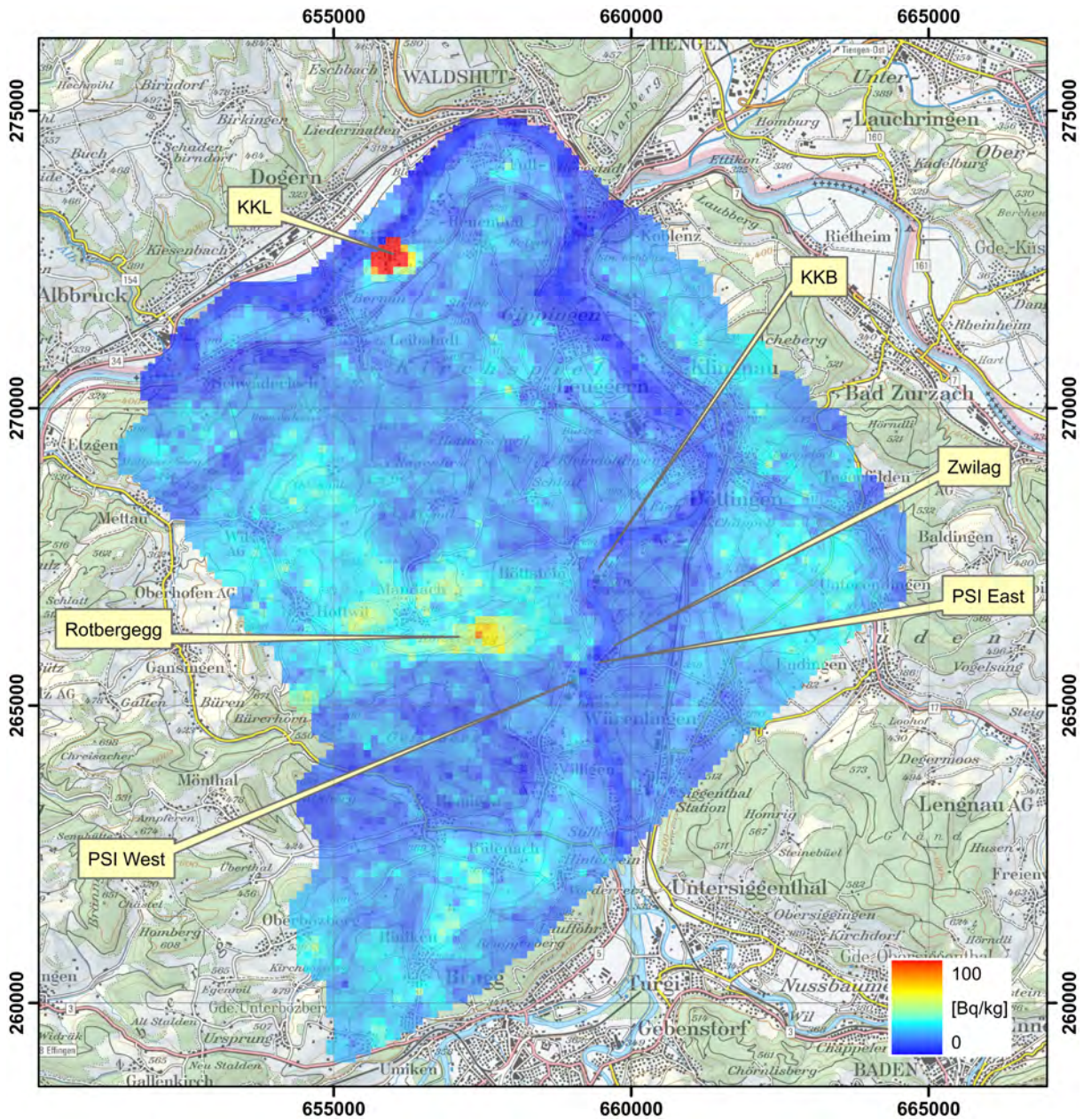
Figure 8: ^{232}Th activity concentration in the vicinity of KKB, KKL, PSI and Zwilag. The high ^{232}Th activity concentrations depicted over KKL are an artefact caused by a misinterpretation of photons emitted from ^{16}N.
PK100 ©2016 swisstopo (JD100042).
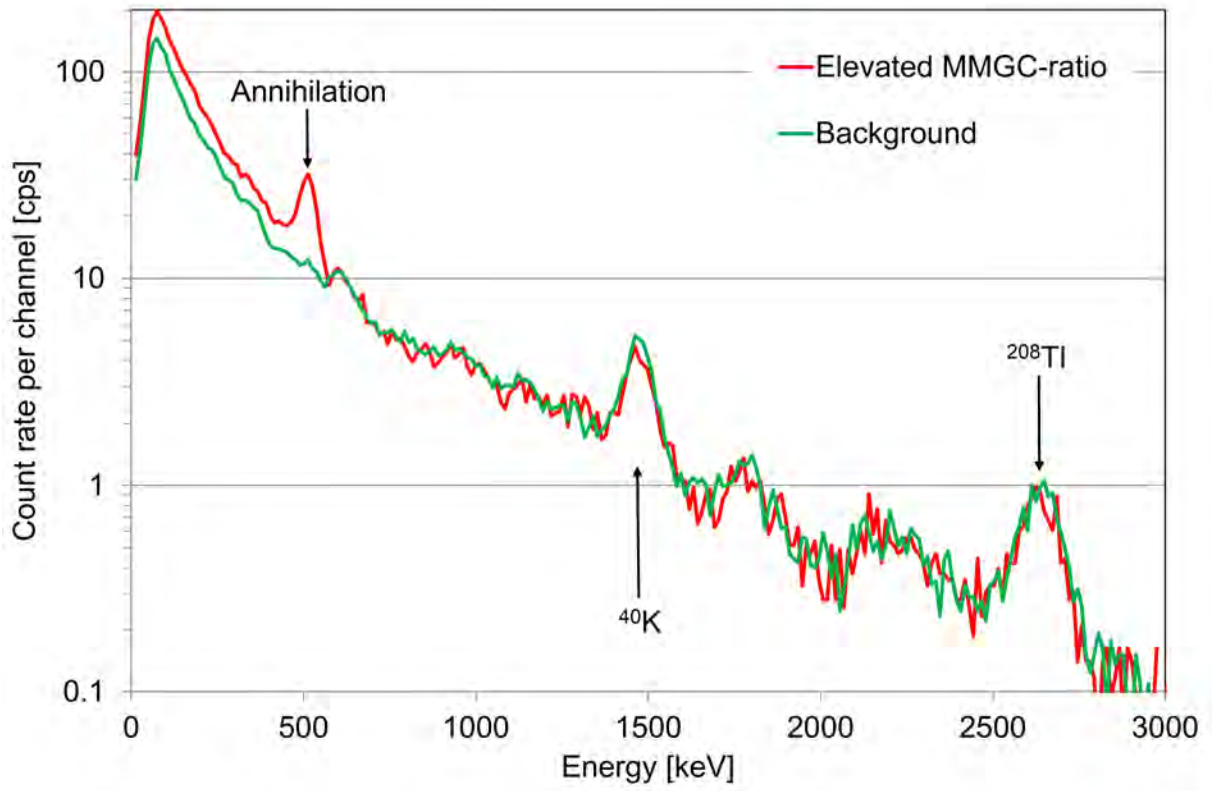
Figure 9: Photon spectrum over the area with elevated MMGC-ratios compared to a background spectrum.

2.2 Baar, Cham and Zug

For the extension of the series of radiological background maps over Swiss cities, the vicinity of Baar, Cham and Zug was measured during ARM16. The map of the ambient dose rate (Figure 10) shows reduced values over the measured areas of Lake Zug. The dose rate reduction is caused by the attenuation of photon radiation originating from natural radionuclides in rock and soil in the overlaying water layer. The map of the MMGC-ratio (Figure 11), an indicator for the presence of artificial radionuclides, does not show any elevated values in the measured area. The map of the ^{232}Th activity concentration (Figure 12) depicts typical values over land and reduced readings over Lake Zug due to the attenuation of the water layer of the lake.
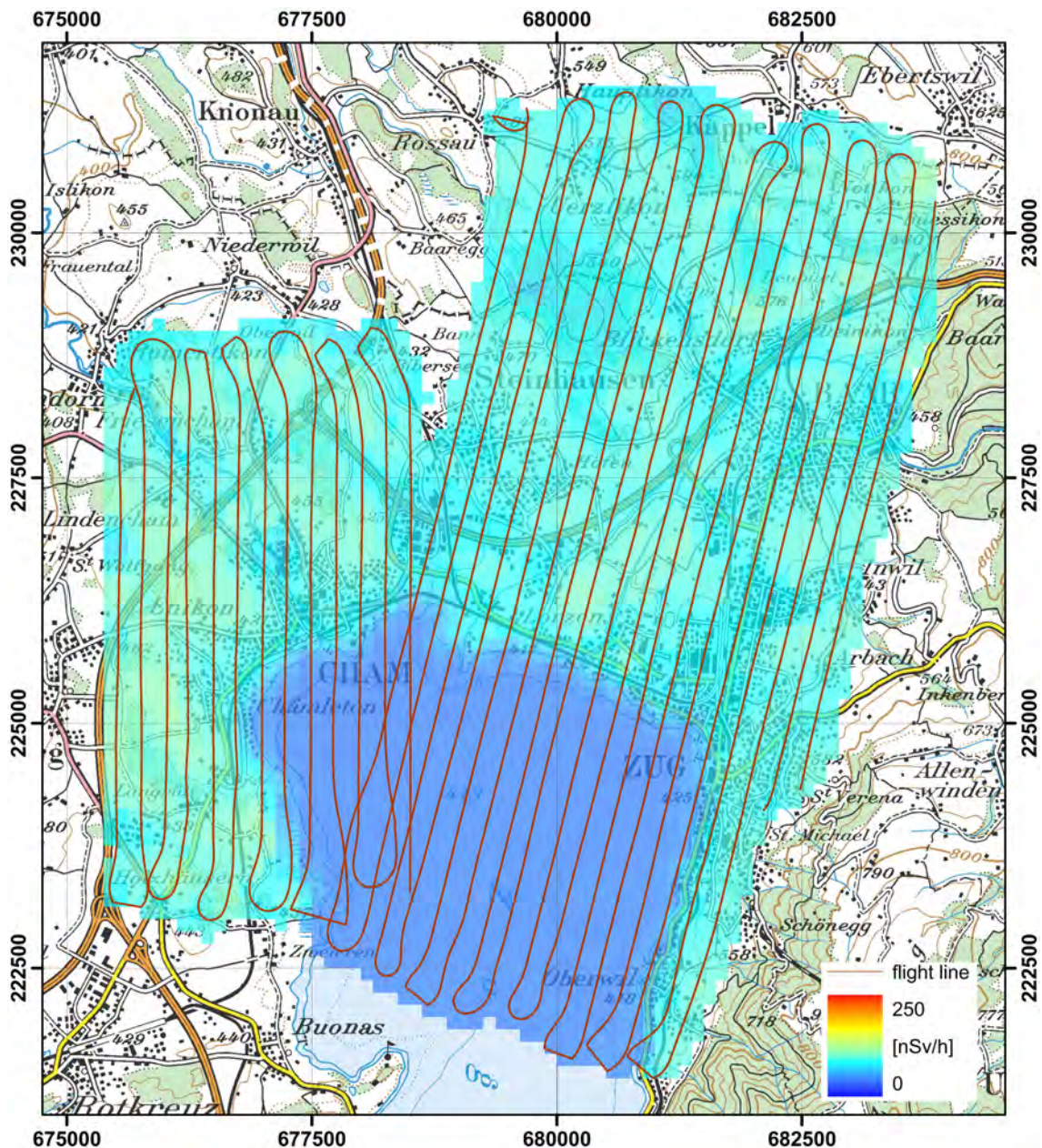
Figure 10: Dose rate in the vicinity of Baar, Cham and Zug.
PK100 ©2016 swisstopo (JD100042).

11
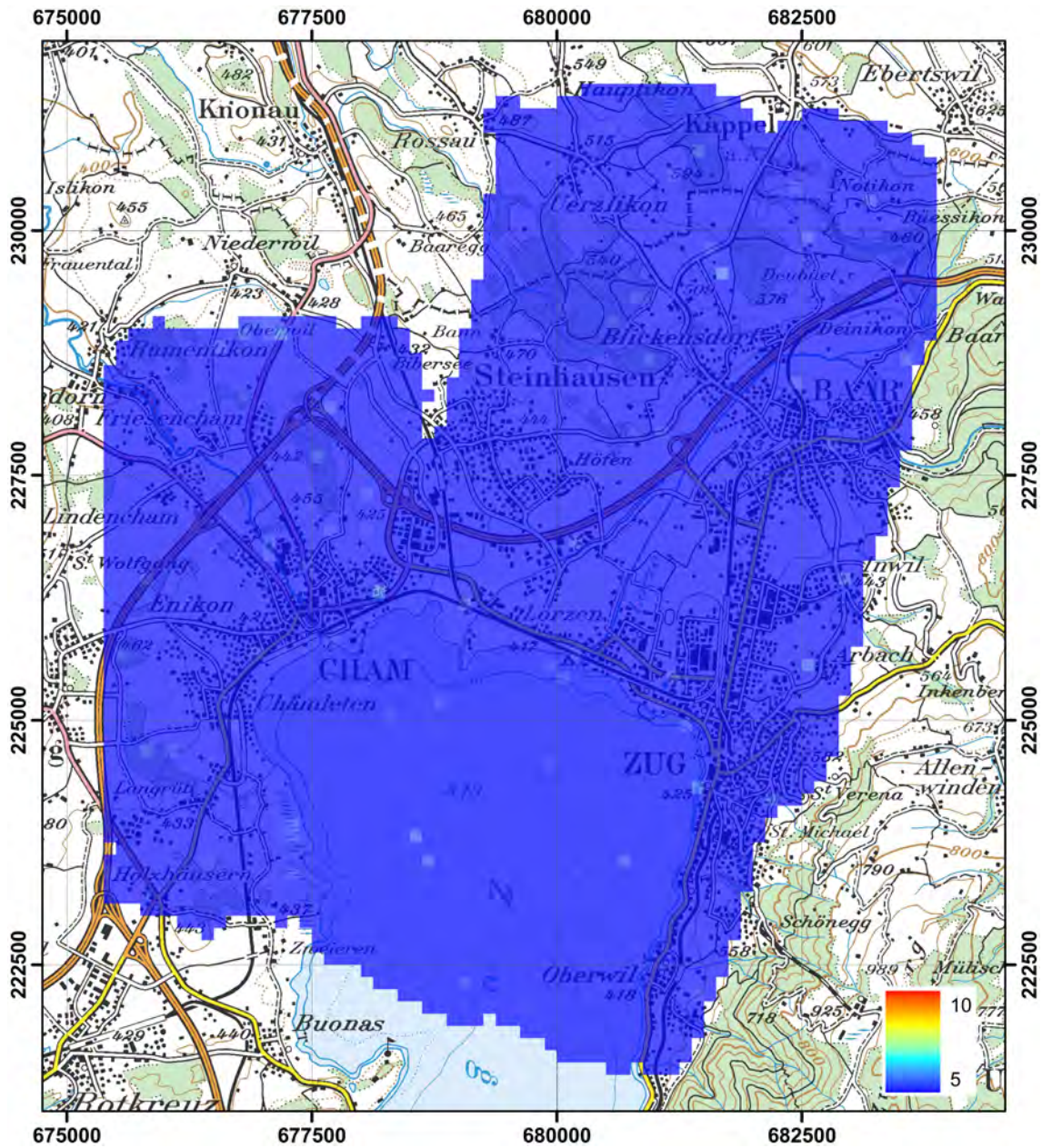
Figure 11: MMGC-ratio in the vicinity of Baar, Cham and Zug.
PK100 ©2016 swisstopo (JD100042).
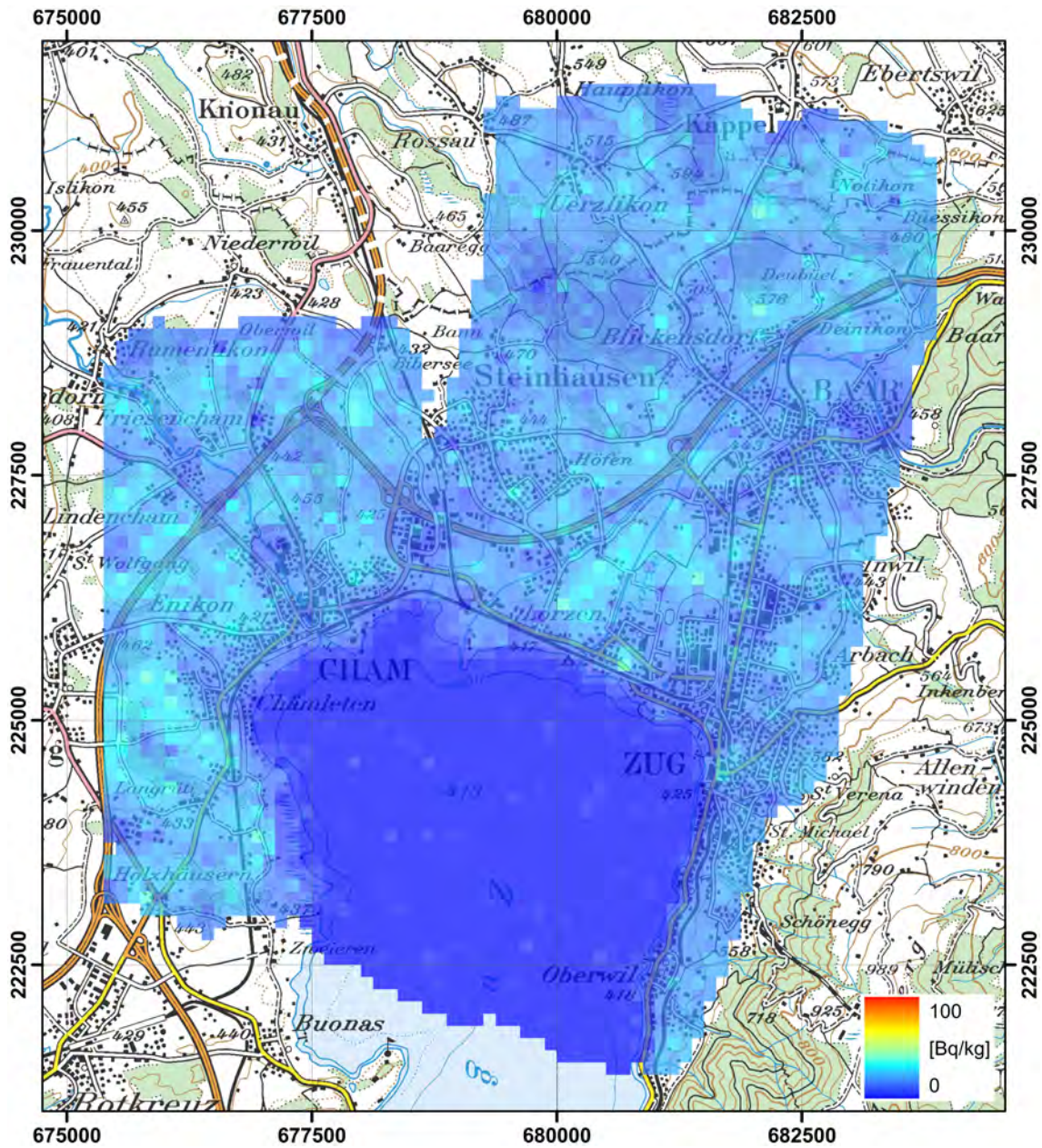
Figure 12: ^{232}Th activity concentration in the vicinity of Baar, Cham and Zug. PK100 ©2016 swisstopo (JD100042).

2.3 Emmen and Luzern

For the extension of the series of radiological background maps over Swiss cities, also the vicinity of Emmen and Luzern was measured during ARM16. The map of the ambient dose rate (Figure 13) shows reduced values over the measured areas of Lake Lucerne. The dose rate reduction is caused by the attenuation of photon radiation originating from natural radionuclides in rock and soil in the overlaying water layer. The map of the MMGC-ratio (Figure 14), an indicator for the presence of artificial radionuclides, does not show any elevated values in the measured area. The map of the ^{232}Th activity concentration (Figure 15) depicts typical values over land and reduced readings over Lake Lucerne due to the attenuation of the water layer.
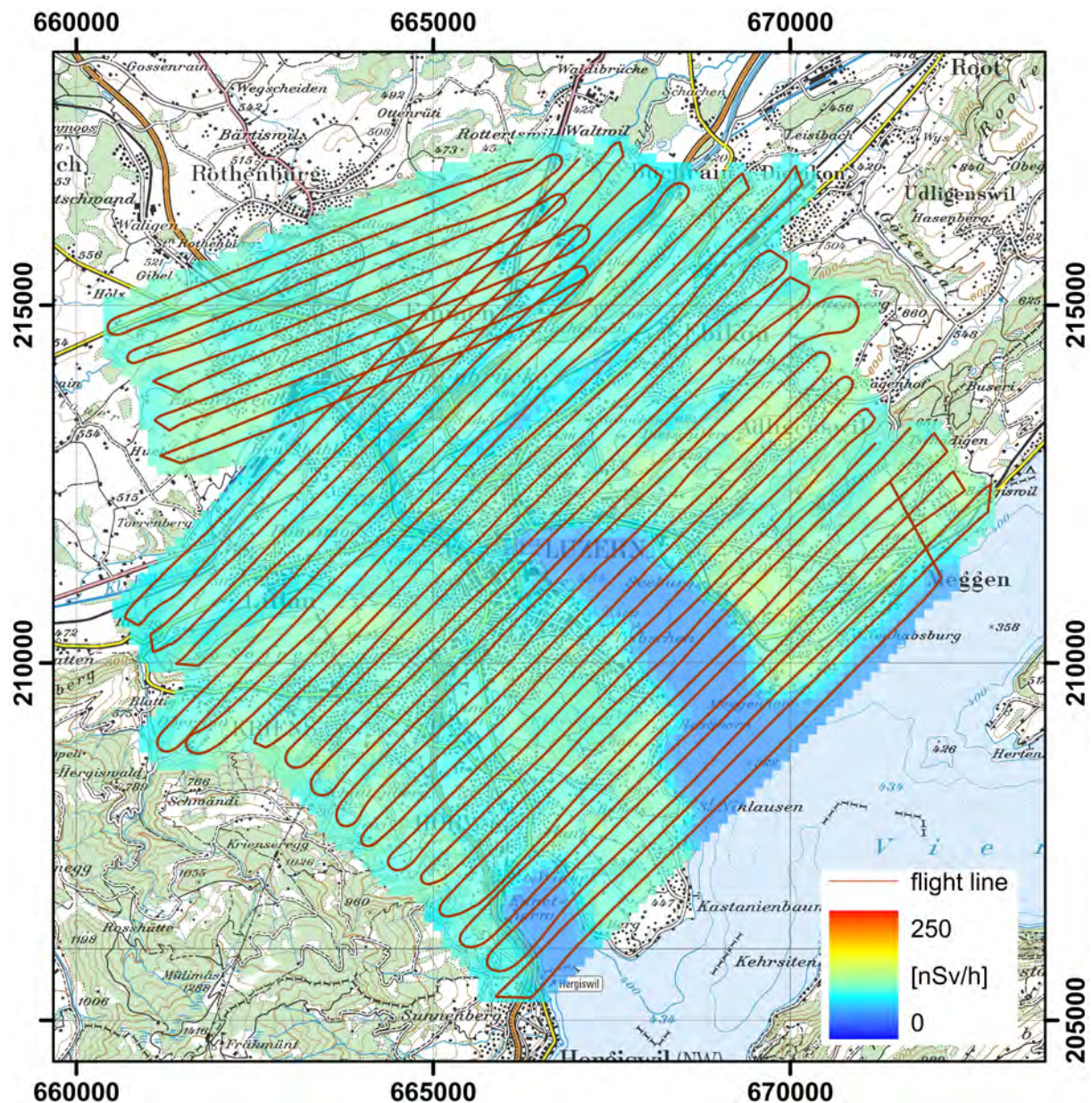
Figure 13: Dose rate in the vicinity of Emmen and Luzern.
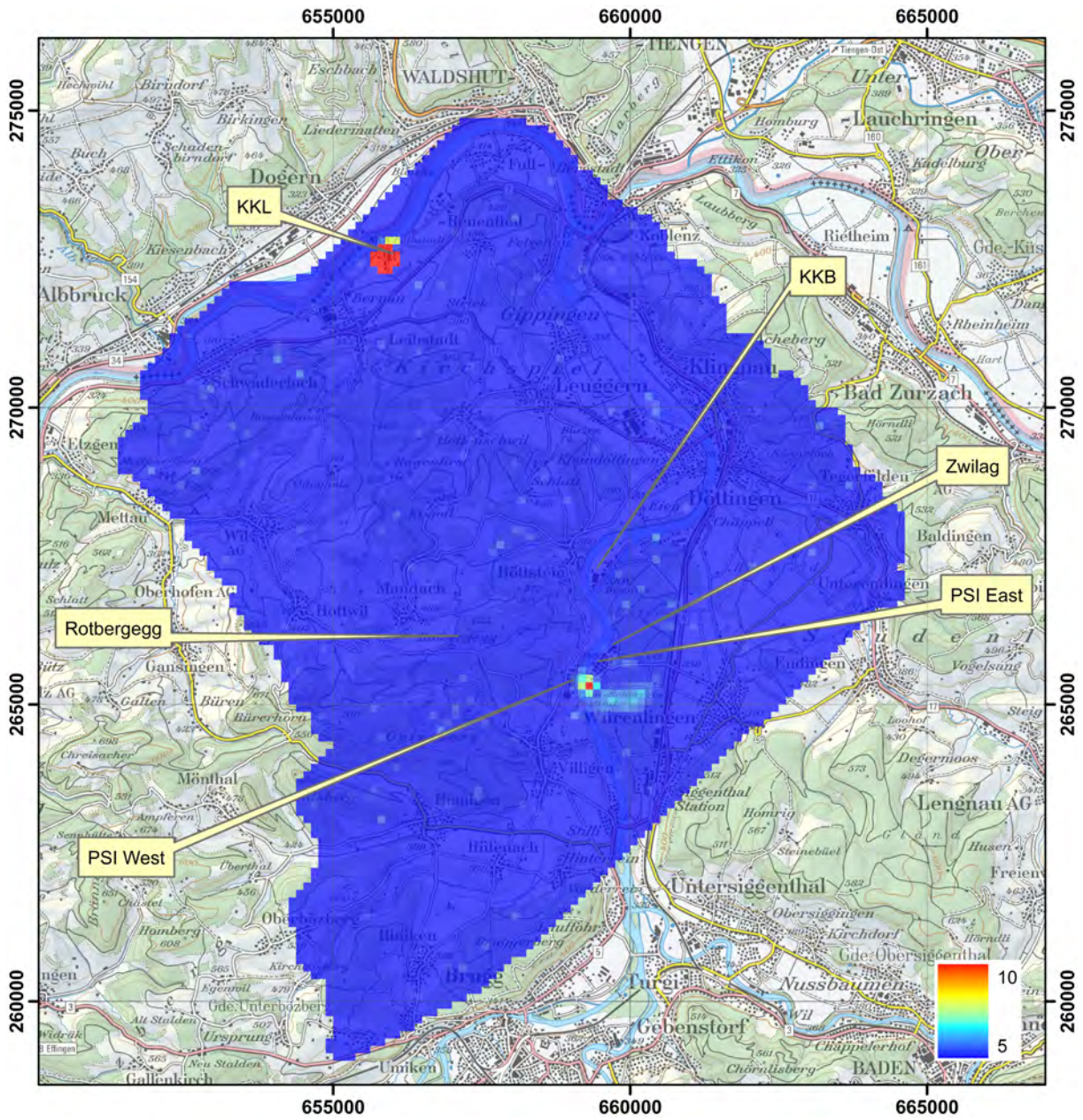PK100 ©2016 swisstopo (JD100042).
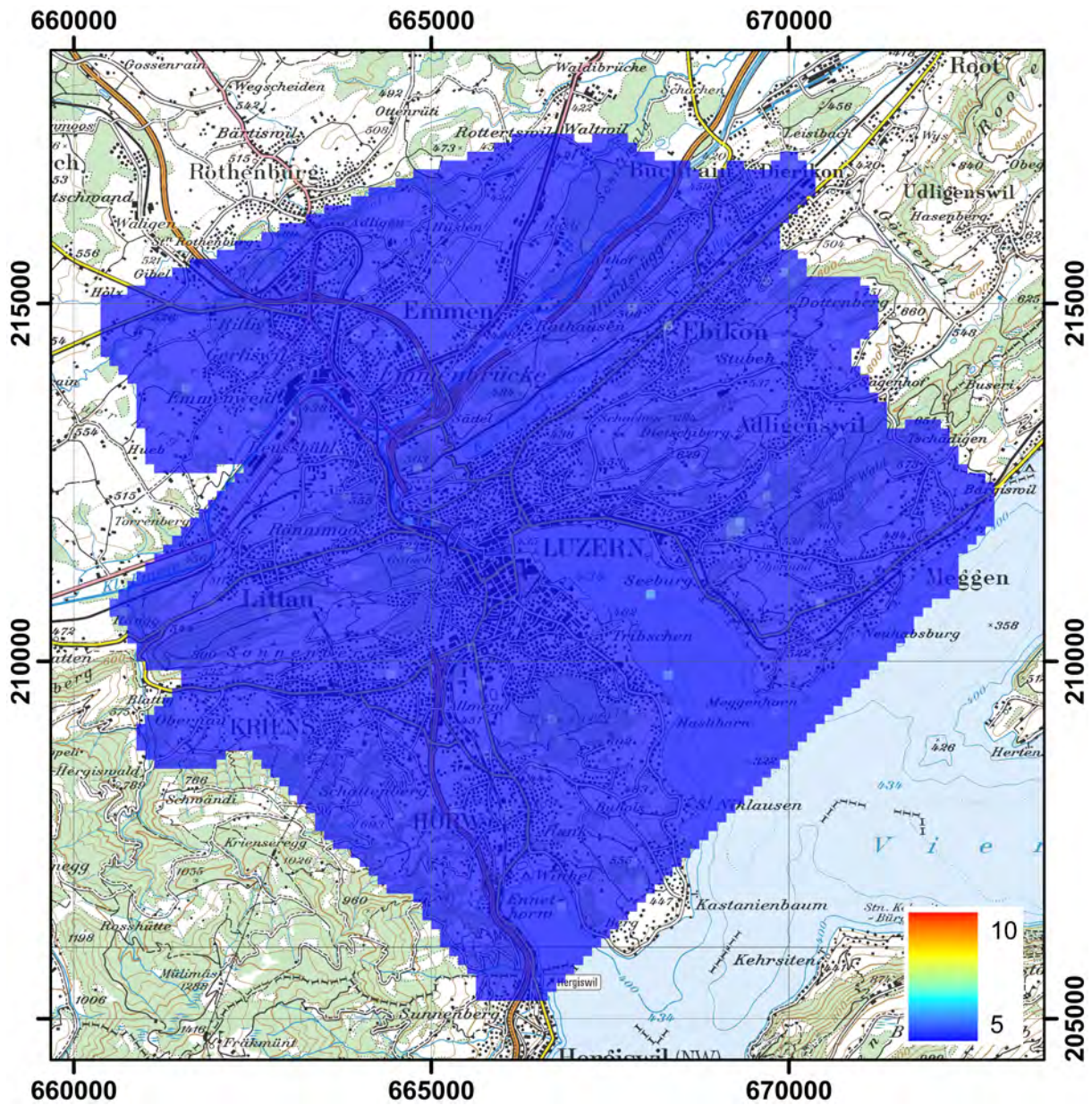
Figure 14: MMGC-ratio in the vicinity of Emmen and Luzern.
PK100 ©2016 swisstopo (JD100042).
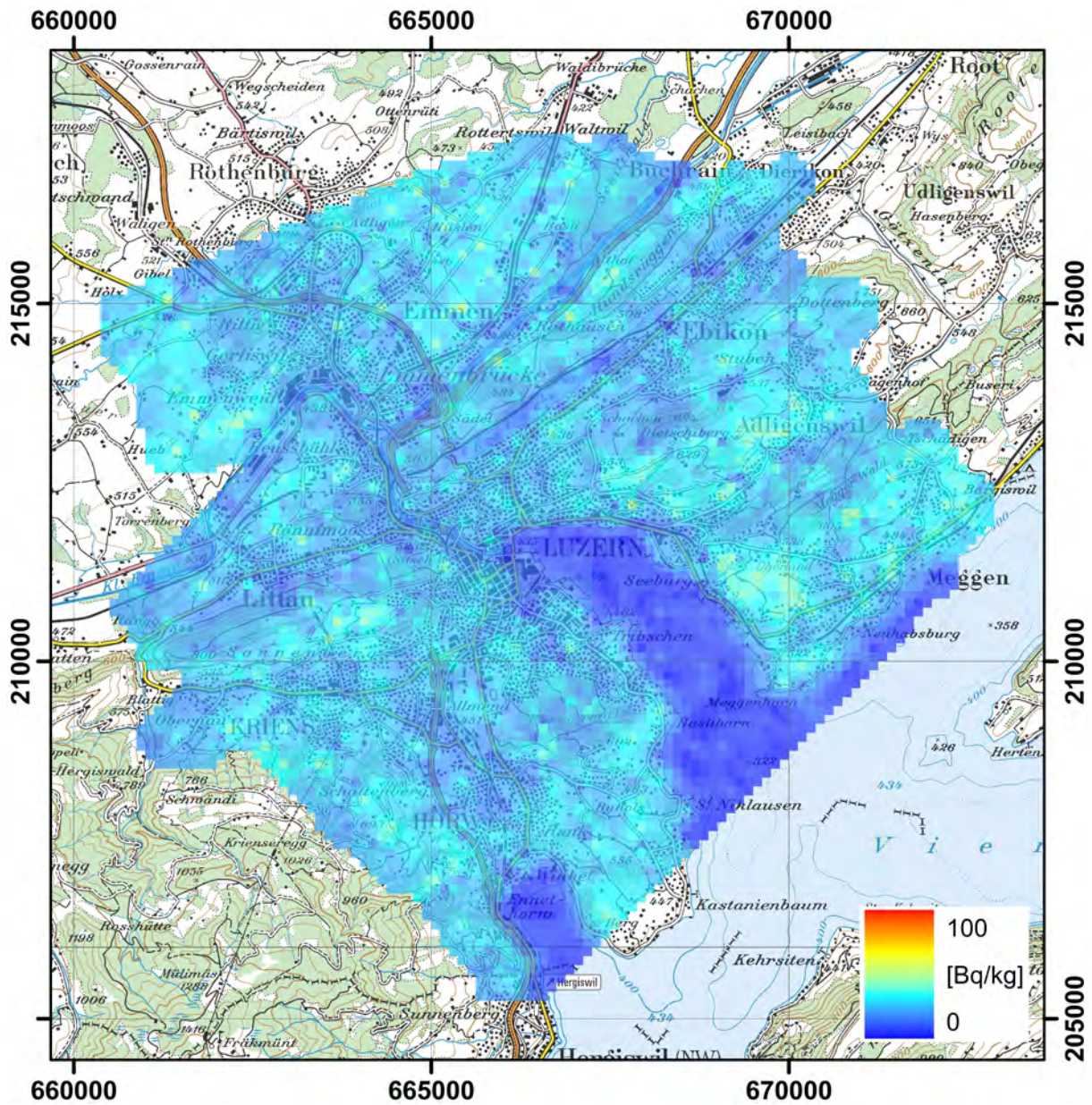
Figure 15: ^{232}Th activity concentration in the vicinity of Emmen and Luzern.
PK100 ©2016 swisstopo (JD100042).

2.4 Vicosoprano

Vicosoprano is located in the Bregaglia valley in south-eastern Switzerland. A probe of the Swiss national dose rate surveillance net NADAM located at Vicosoprano shows typical values around 200 nSv/h, the highest value of all 66 probes distributed in Switzerland. This value cannot be explained by the increase of the cosmic dose rate due to the elevation of Vicosoprano (1067 m) alone. The airborne measurements had the task to check the measured dose rate of the NADAM probe and to identify the source of the increased dose rate. The maps of the ambient dose rate measured with both systems ARM and RLL (Figures 16 and 17) show that the NADAM probe is located in an area with elevated dose rates. The value of 214 nSv/h measured with the ARM system at the location of the probe confirms the readings of the probe. The ambient dose rate is composed of a contribution from cosmic rays and a terrestrial component generated by radionuclides in rock and soil. Whereas the cosmic component is altitude dependent, the terrestrial component is only influenced by the radionuclide content of rock and soil. The map of the terrestrial dose rate (Figure 18) indicates clearly elevated radionuclide activity concentration in the area of the NADAM probe. The map of the MMGC-ratio (Figure 19) as an indicator for artificial radionuclides shows no elevated values, suggesting natural radionuclides as cause for the dose rate increase. The maps of the activity concentration of the main natural radionuclides ^{40}K (Figure 20), ^{232}Th (Figure 21) and ^{238}U (Figure 22) show clearly elevated values in the area of the NADAM probe. Thus, the observed dose rate increase can be associated with an elevated natural radionuclide content. No indication for the presence of artificial radionuclides was observed.
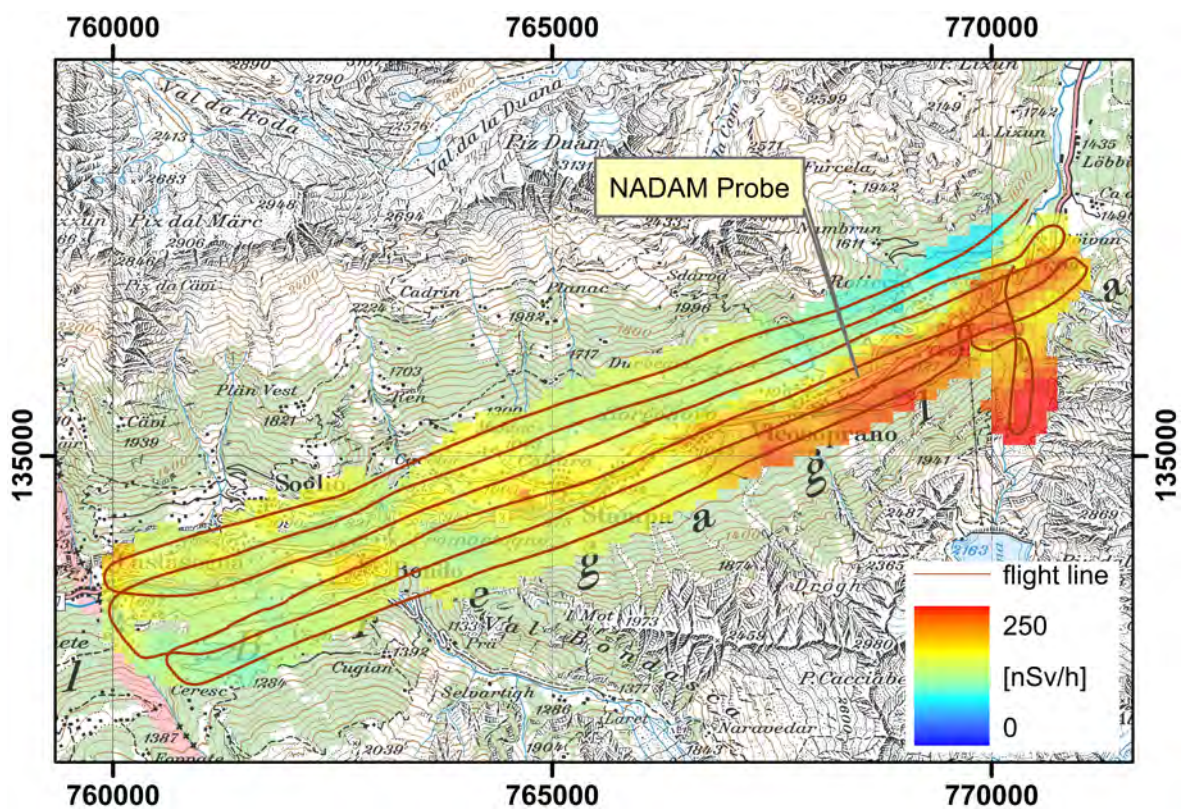
Figure 16: Dose rate in the vicinity of Vicosoprano measured by the ARM system. PK100 ©2016 swisstopo (JD100042).

17
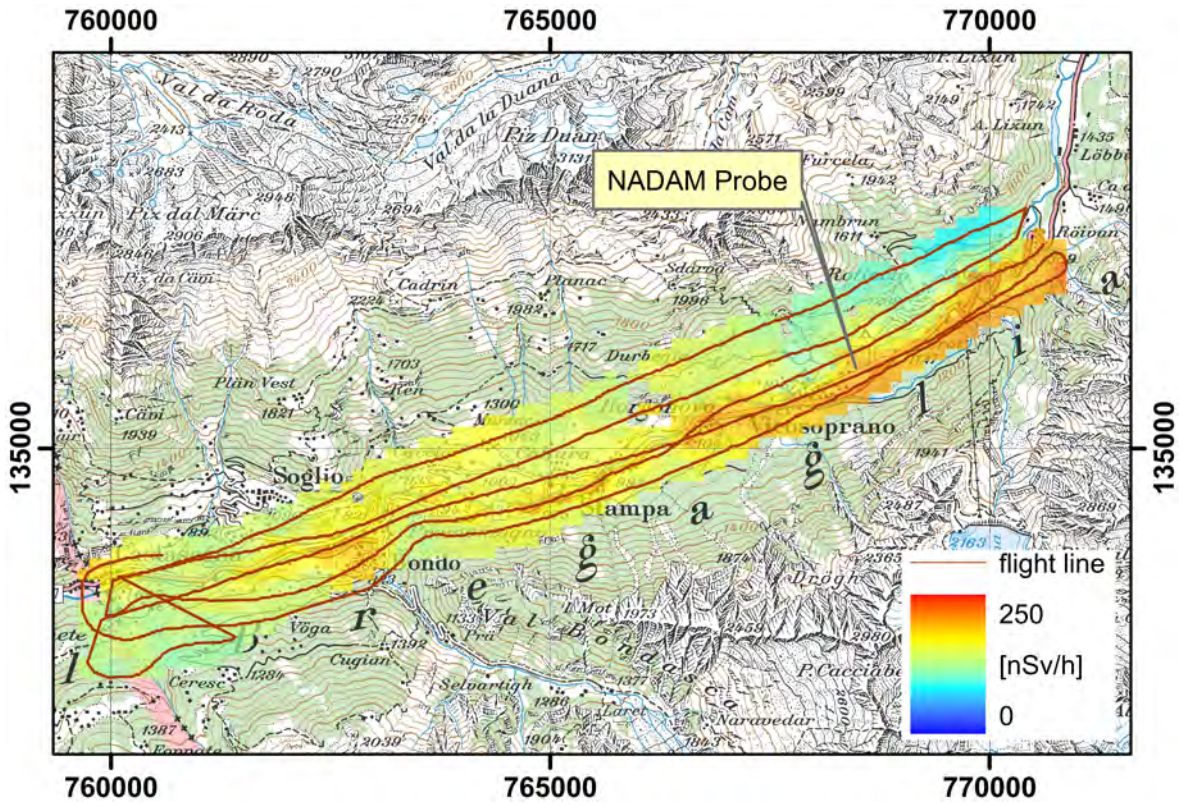
Figure 17: Dose rate in the vicinity of Vicosoprano measured by the RLL system.
PK100 ©2016 swisstopo (JD100042).
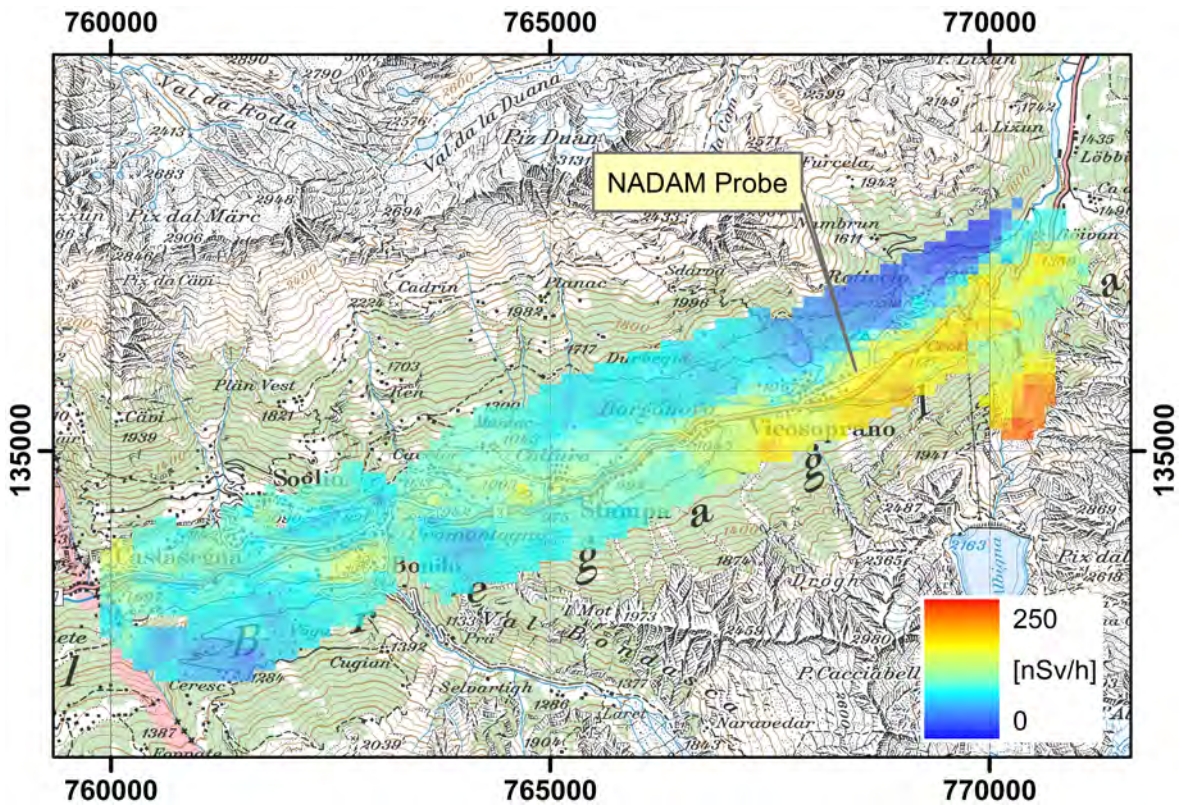
Figure 18: Terrestrial component of the dose rate in the vicinity of Vicosoprano measured
by the ARM system. PK100 ©2016 swisstopo (JD100042).
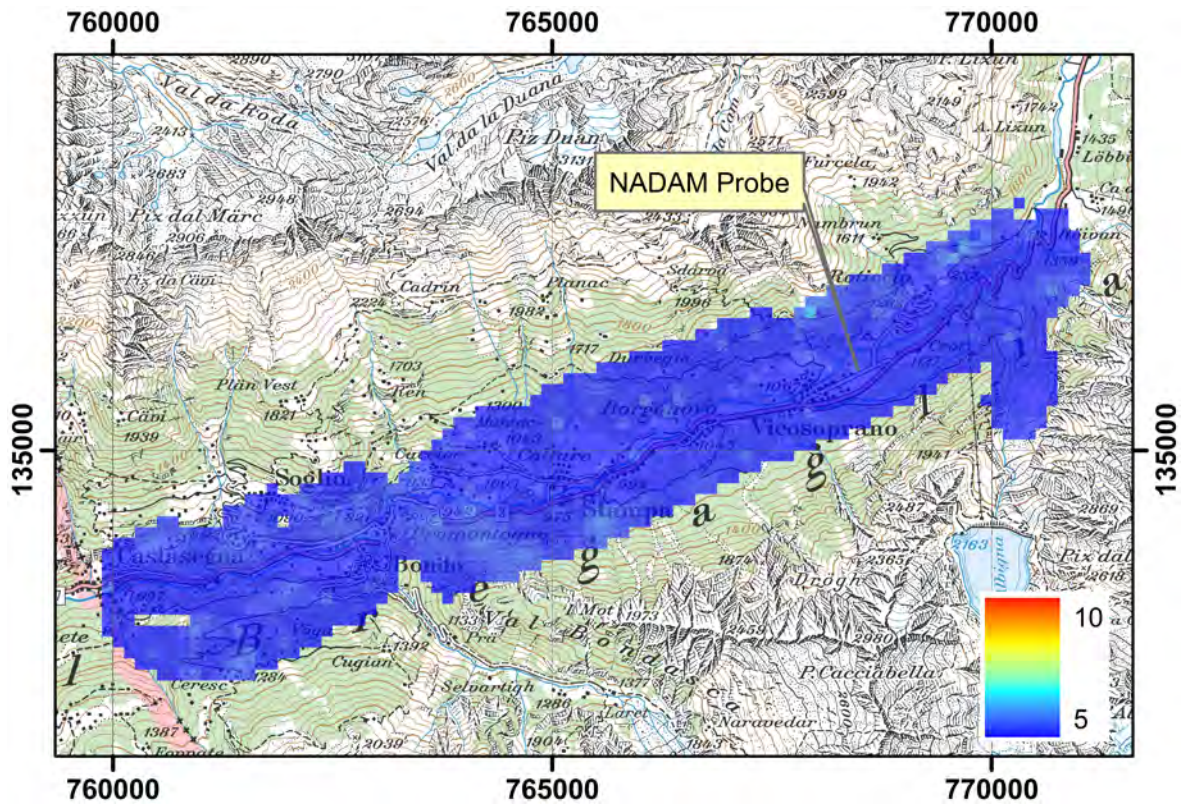
Figure 19: MMGC-ratio in the vicinity of Vicosoprano measured by the ARM system. PK100 ©2016 swisstopo (JD100042).
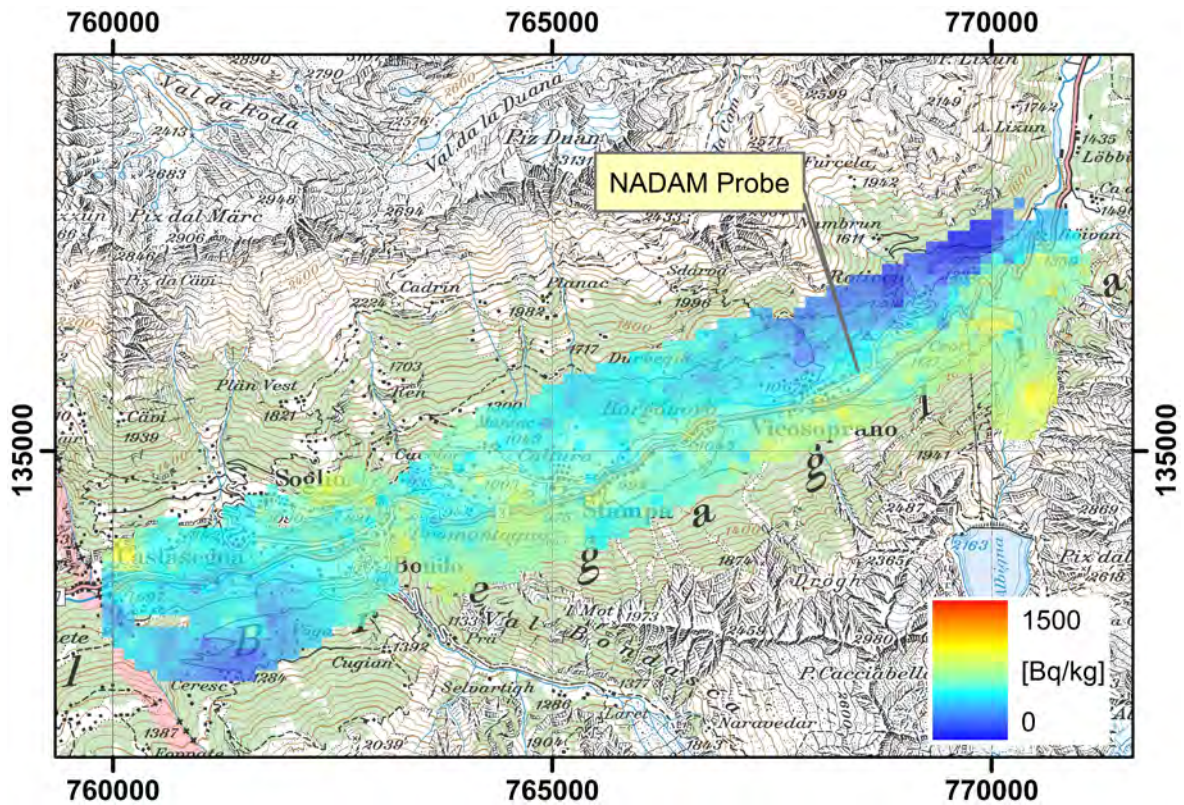
Figure 20: ^{40}K activity concentration in the vicinity of Vicosoprano measured by the ARM system. PK100 ©2016 swisstopo (JD100042).

Figure 21: ^{232}Th activity concentration in the vicinity of Vicosoprano measured by the ARM system. PK100 ©2016 swisstopo (JD100042).

Figure 22: ^{238}U activity concentration in the vicinity of Vicosoprano measured by the ARM system. PK100 ©2016 swisstopo (JD100042).
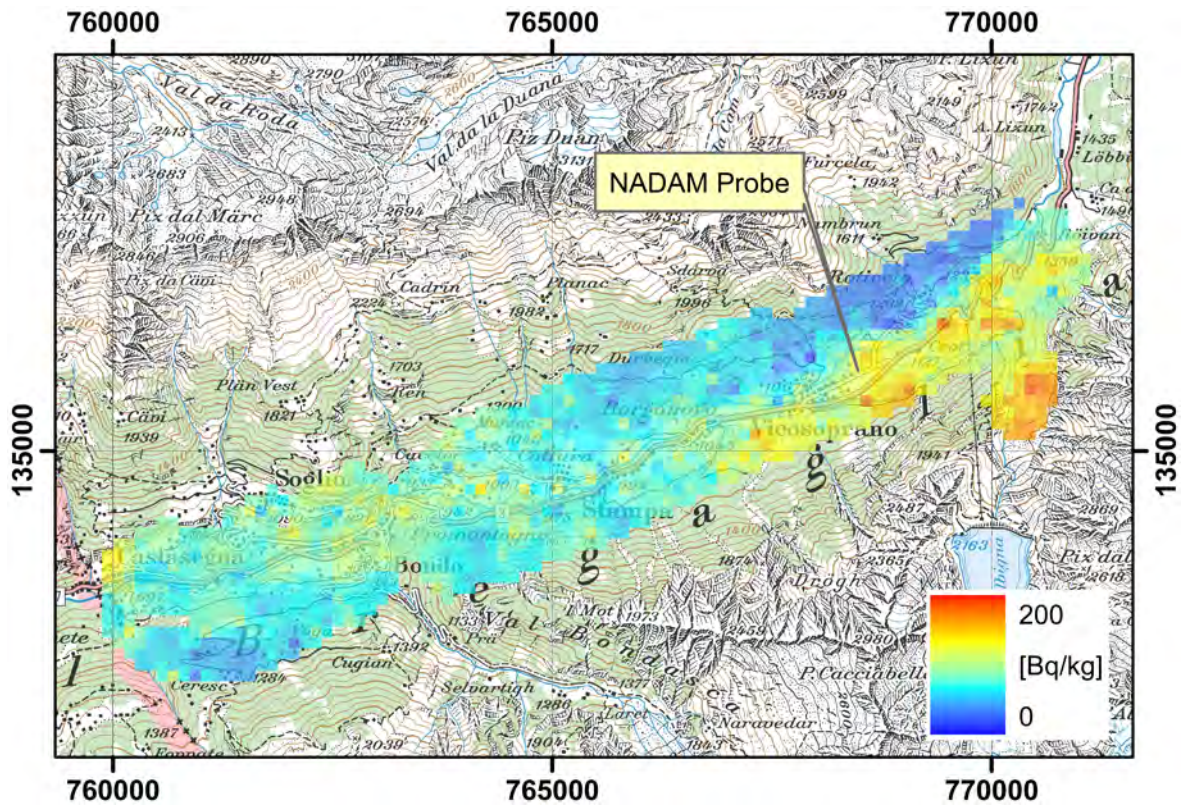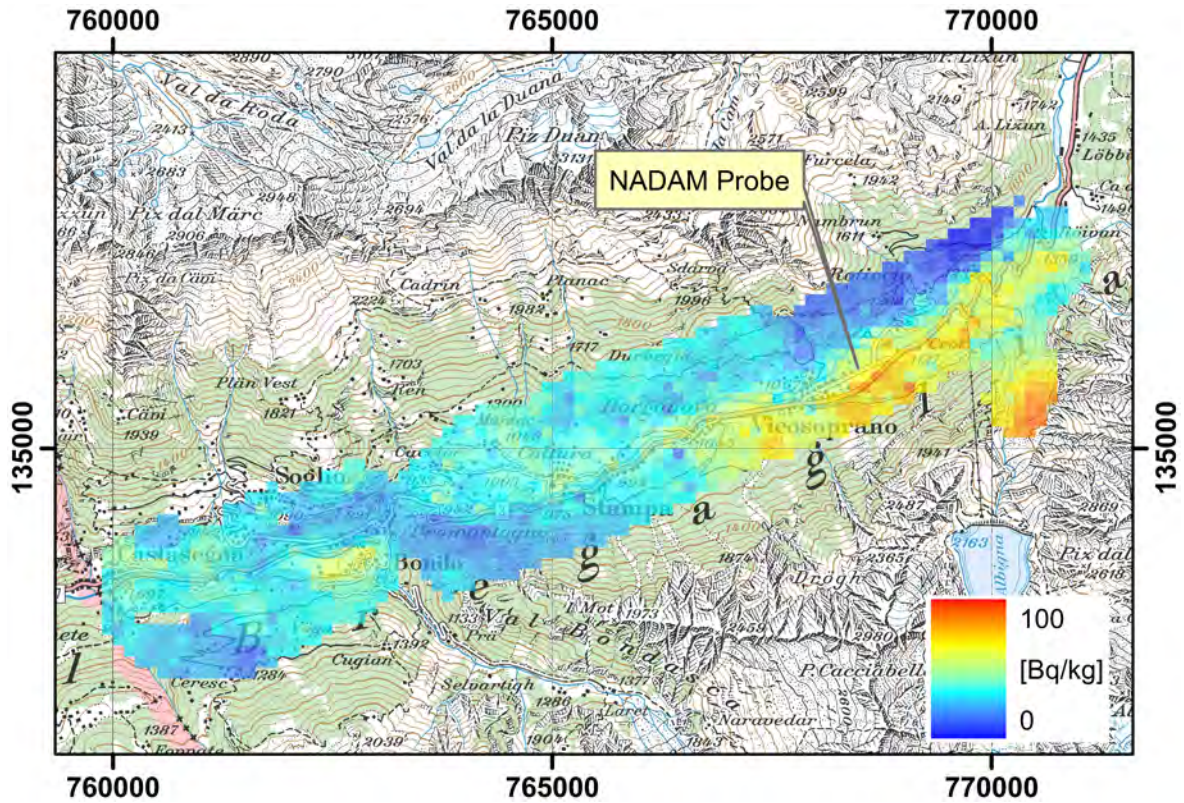
2.5 Exercise LAURA

The scenario of the emergency exercise LAURA was the crash of an airplane with a cargo of radioactive sources on the Emmen military airfield. The emergency exercise was supported by personnel of NAZ, RUAG aerospace and PSI. One major target of the exercise was the test of decision making and inclusion of special forces according to the actual assessment of the situation. The fire brigade of Lucerne were the first responders on the site of the simulated crash. As it became clear that radioactive materials could be an issue, the radiation emergency unit for central Switzerland (Strahlenwehr Region Zentralschweiz) and the National Emergency Operations Centre (NAZ) were alarmed. Appropriate to the exercise scenario, NAZ deployed additionally its airborne gamma spectroscopy unit and the standby radiation protection expert team of PSI. Besides caring for casualties and cordoning the crash site, the Lucerne fire brigade set up a mobile command center during the time needed for the additional forces to arrive. The helicopter of the airborne gamma spectrometry team landed near the mobile command center and the team set up a flight plan after being instructed on the situation at hand. Figure 23 shows the flight line and the measured dose rate over the simulated crash site. An increase of dose rate can be identified in the center of the site. The map of the MMGC-ratio (Figure 23) indicates the presence of artificial radionuclides at this position. A closer look to maps of specific radionuclide point source activities shows in the center of the exercise area elevated values for the radionuclide ^{137}Cs with a maximum value of point source activity of 3 GBq (Figure 25) at coordinate (665821,215463). About 100 m distant to the maximum of ^{137}Cs, the maximum of 0.4 GBq ^{60}Co- point source activity was measured at coordinate (665723, 215501) (Figure 26). The photon emissions of the sources can clearly identified in the average spectra over the indicated areas (Figure 28). Due to the small exercise area compared to the field of view of the airborne gamma-spectrometry (approximately 300 m), all displayed spectra show some signal originating from the sources. The locations of measured activity maxima are marked in (Figure 27).

For a realistic simulation of a debris field, radioactive sources were placed at ten positions inside of the exercise area. The sum of source activities positioned in the field were 0.4 GBq ^{60}Co and 3.4 GBq ^{137}Cs, agreeing well with the measured activity maxima. A ^{99m}Tc-source with an activity of 100 MBq was not detected due to its low activity combined with the main photon emission located at the low energy of 141 keV.
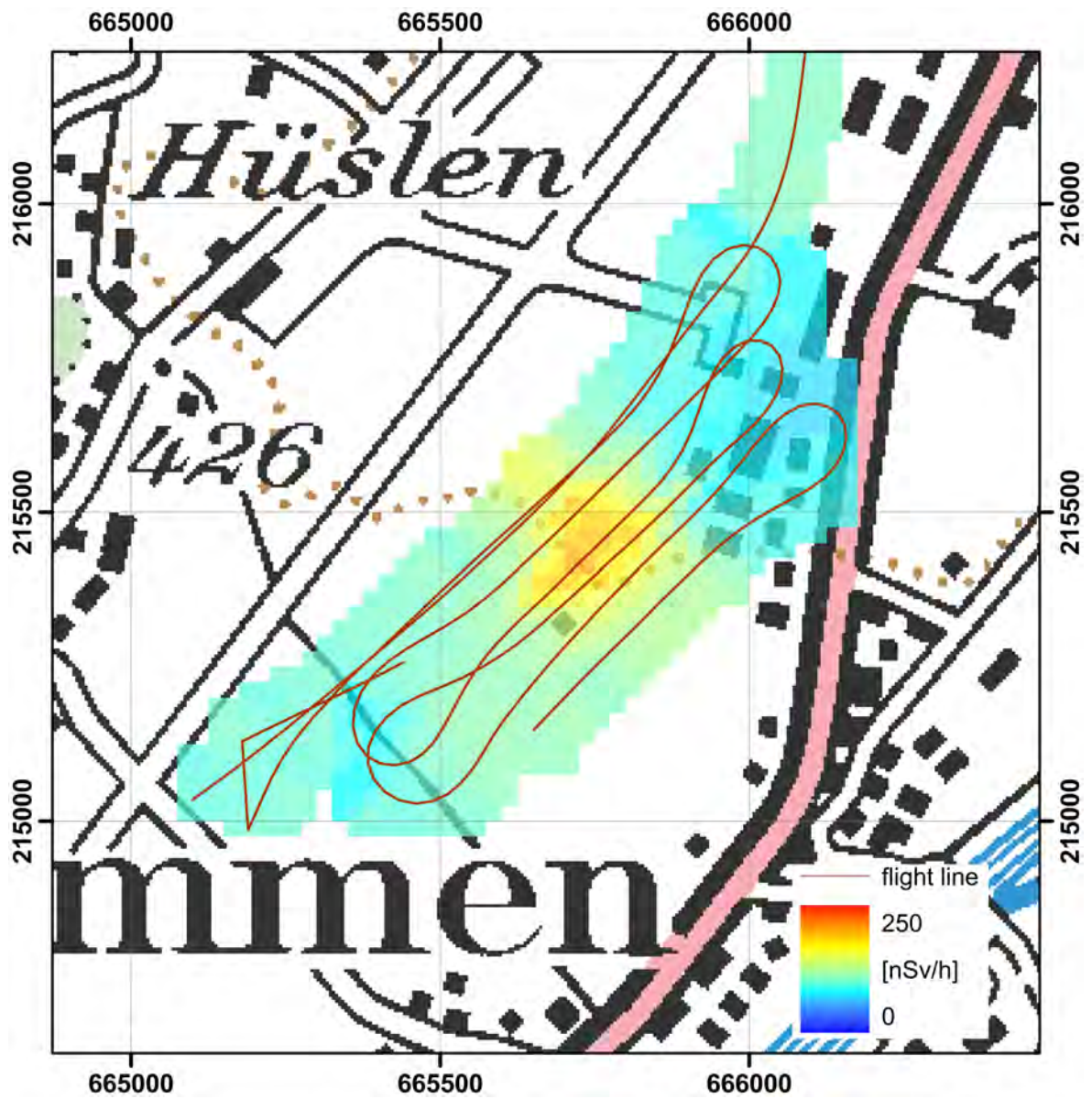
Figure 23: Dose rate over the site of emergency exercise LAURA.
PK100 ©2016 swisstopo (JD100042).
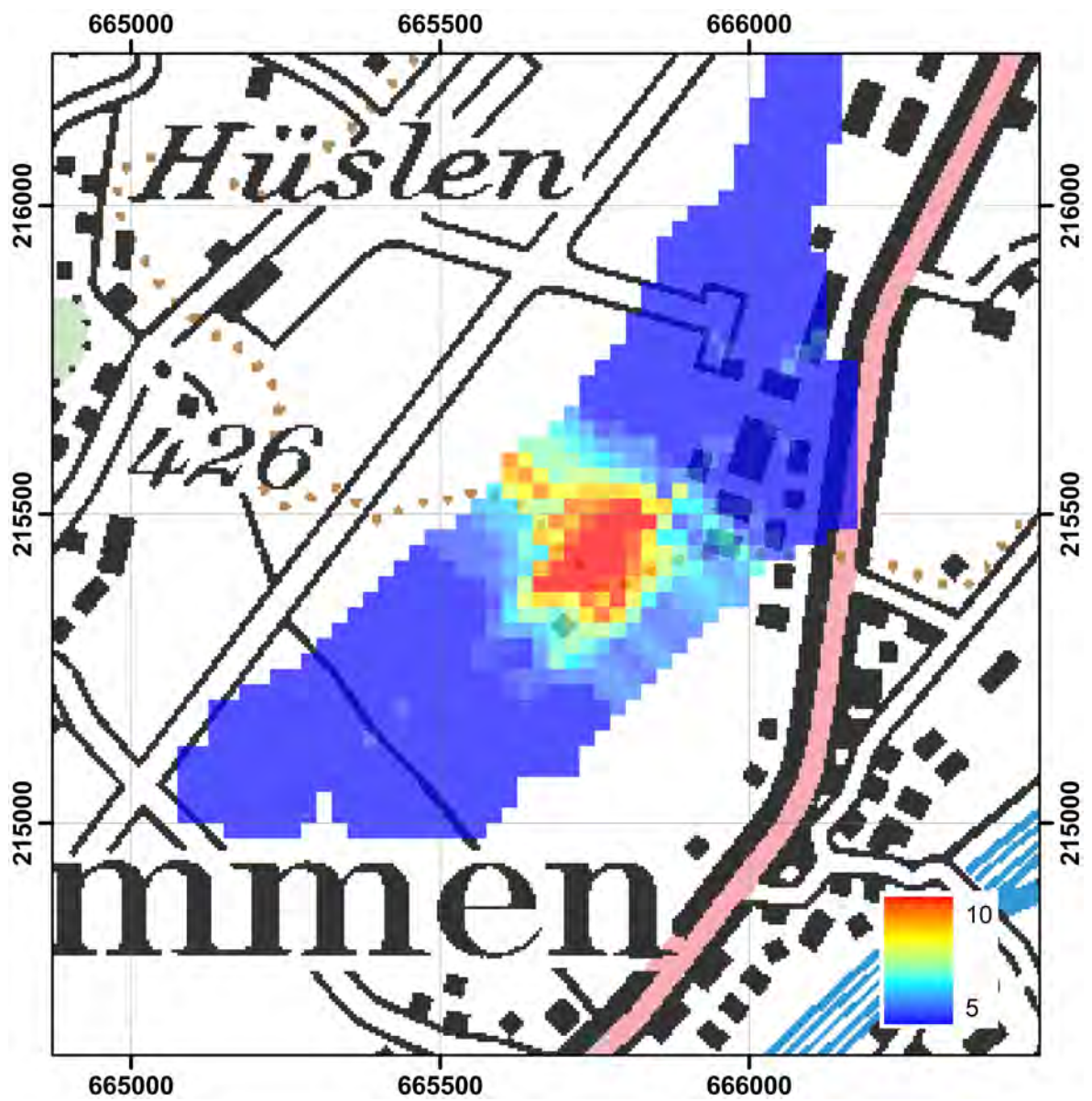
Figure 24: MMGC-ratio over the site of emergency exercise LAURA.
PK100 ©2016 swisstopo (JD100042).
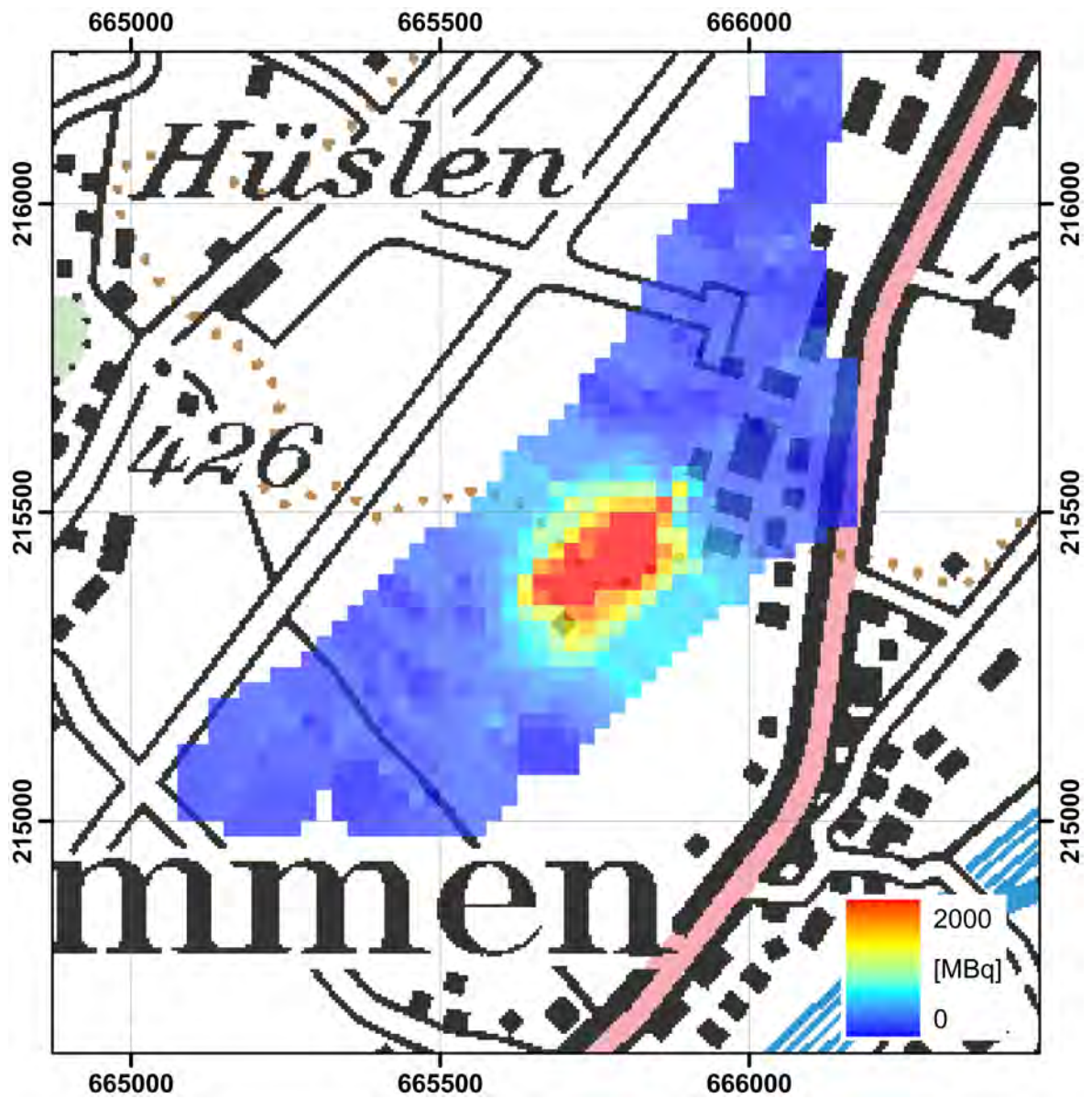
Figure 25: ^{137}Cs-point source activity over the site of emergency exercise LAURA.
PK100 ©2016 swisstopo (JD100042).
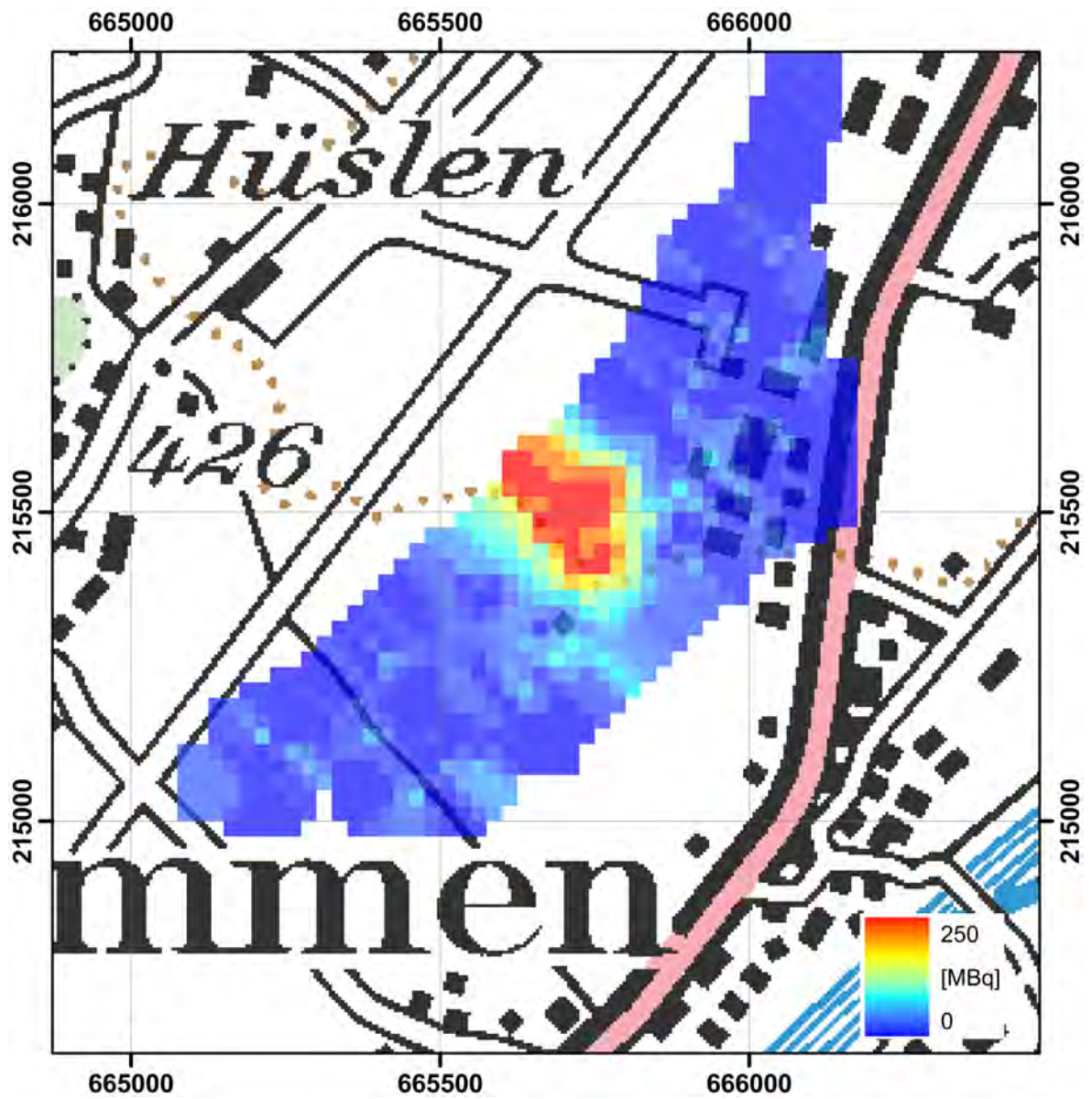
Figure 26: ⁶⁰Co-point source activity over the site of emergency exercise LAURA.
PK100 ©2016 swisstopo (JD100042).

Figure 27: Location of maximum point source activity over the site of emergency exercise LAURA.
PK100 ©2016 swisstopo (JD100042).
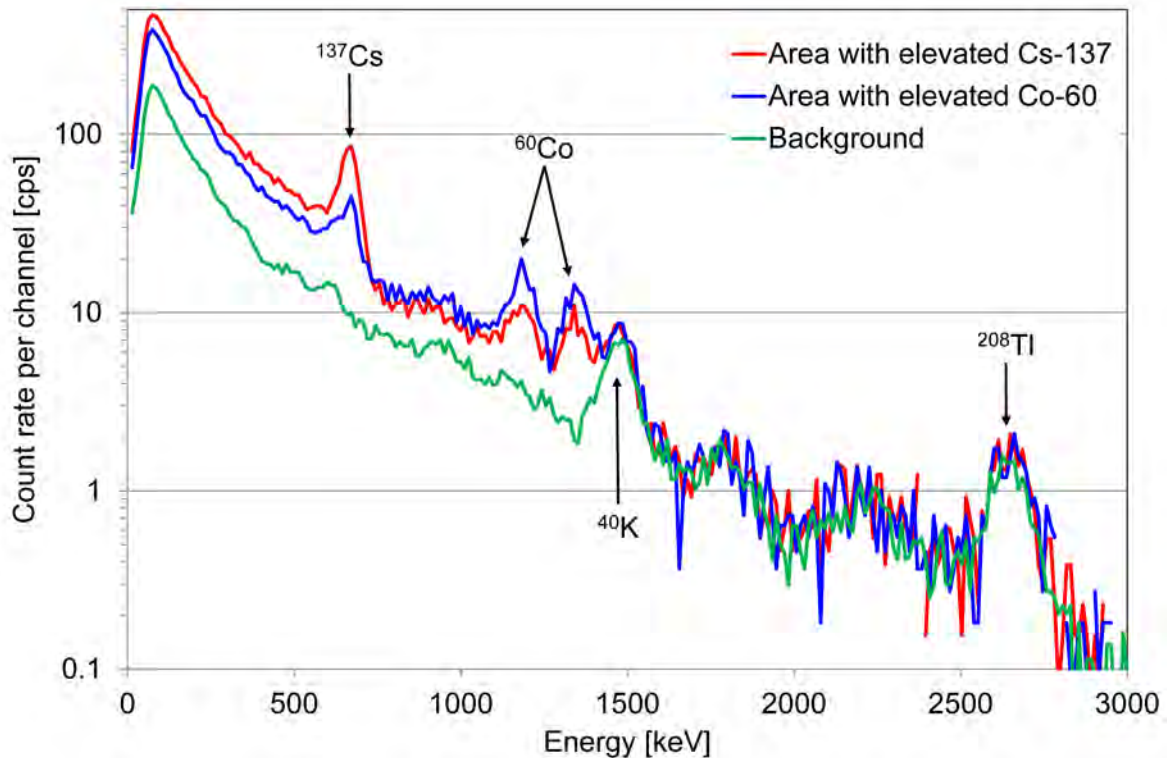
Figure 28: Photon spectra over the site of emergency exercise LAURA.

2.6 Highway A13, Lake Neuchâtel and Limpach valley

Three measuring flights of the exercise ARM16 were dedicated to study the influence of measuring height and topography on the quality of the derived quantities.

The flight from the airfield in Dübendorf to the measuring area around Vicosoprano was used as a profile measuring flight in difficult topography. The profile (Figure 29) starts in the northwest at Rheineck near Lake Constance and follows the highway A13 to the south to Sargans. South of Sargans the profile is discontinued. A second leg of the profile begins at Fürstenau and ends at the San Bernardino Pass in the south. The terrestrial dose rate along the profile (Figure 30) shows a distinct increase between positions 70 km and 80 km of the profile. The increase corresponds to a deviation of the ground clearance from the standard value of 100 m above ground (Figure 31) indicating a possible artefact generated by insufficient correction of the influence of ground clearance and topography. The deviation from the standard ground clearance was caused by the alpine topography, which is difficult to follow precisely with a helicopter. A scatter-gram of the measured terrestrial dose rate versus the ground clearance (Figure 32) shows clearly a dependence for part of the profile. This scatter-gram shows values of the terrestrial dose rate without the generally applied correction of topographic effects according to Schwarz (1991). The application of this topographic correction reduces the influence of the ground clearance on terrestrial dose rate, but is not able to compensate completely (Figure 33). This result indicates the necessity to revise the implementation of the algorithm in the applied software, the associated parameters and the employed algorithm itself. Further evaluation and interpretation of the data measured over the profile along the highway A13 is postponed until completion of this project.
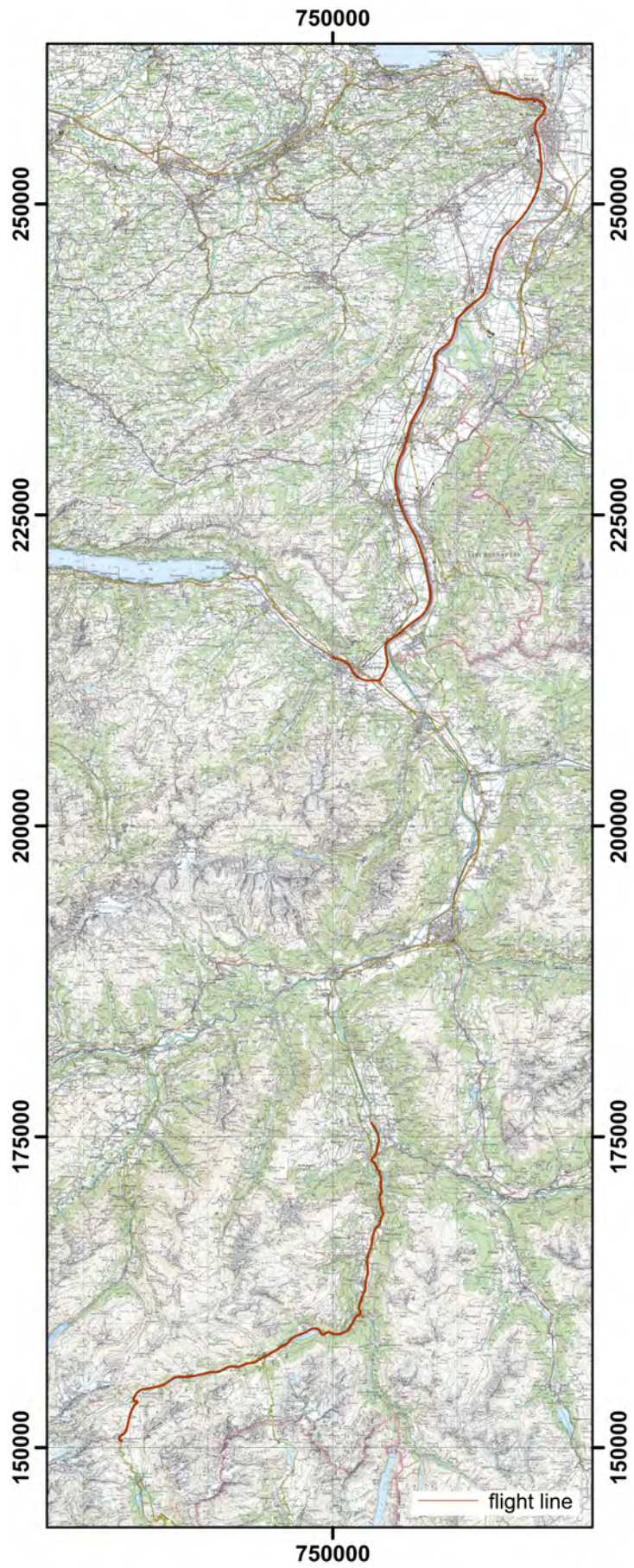
Figure 29: Flight line of the profile along highway A13.
PK100 ©2016 swisstopo (JD100042).
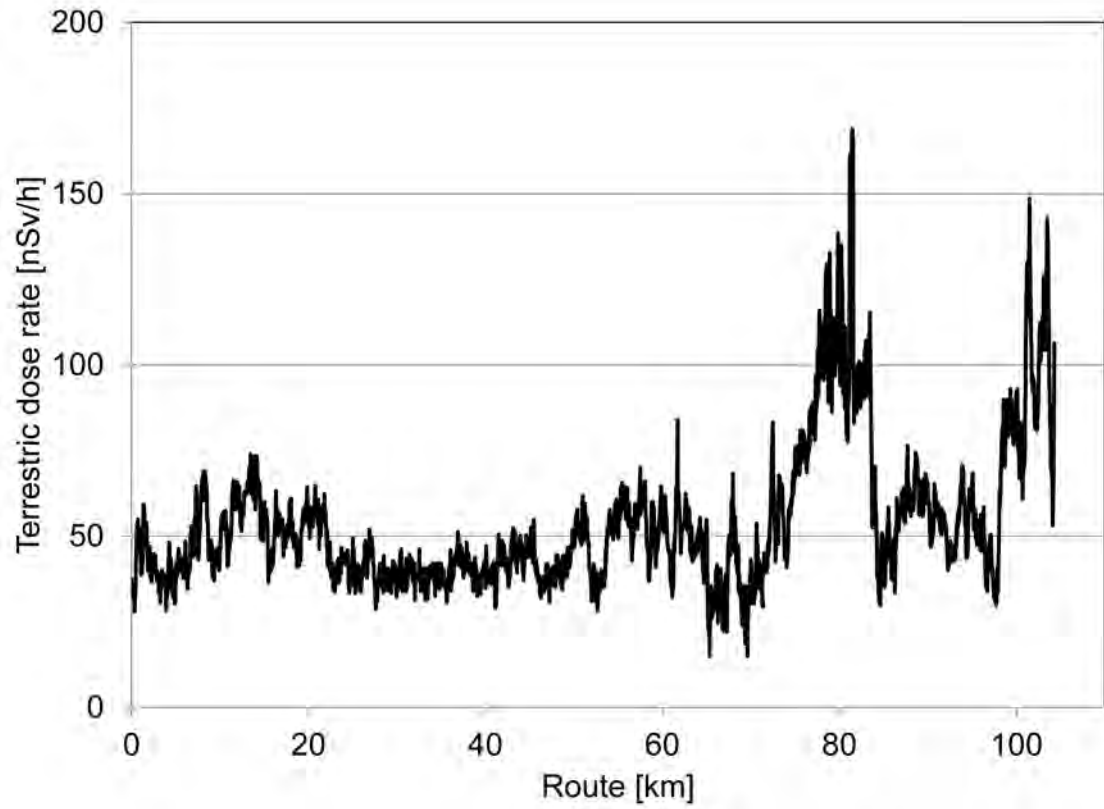
Figure 30: Terrestrial dose rate along highway A13.
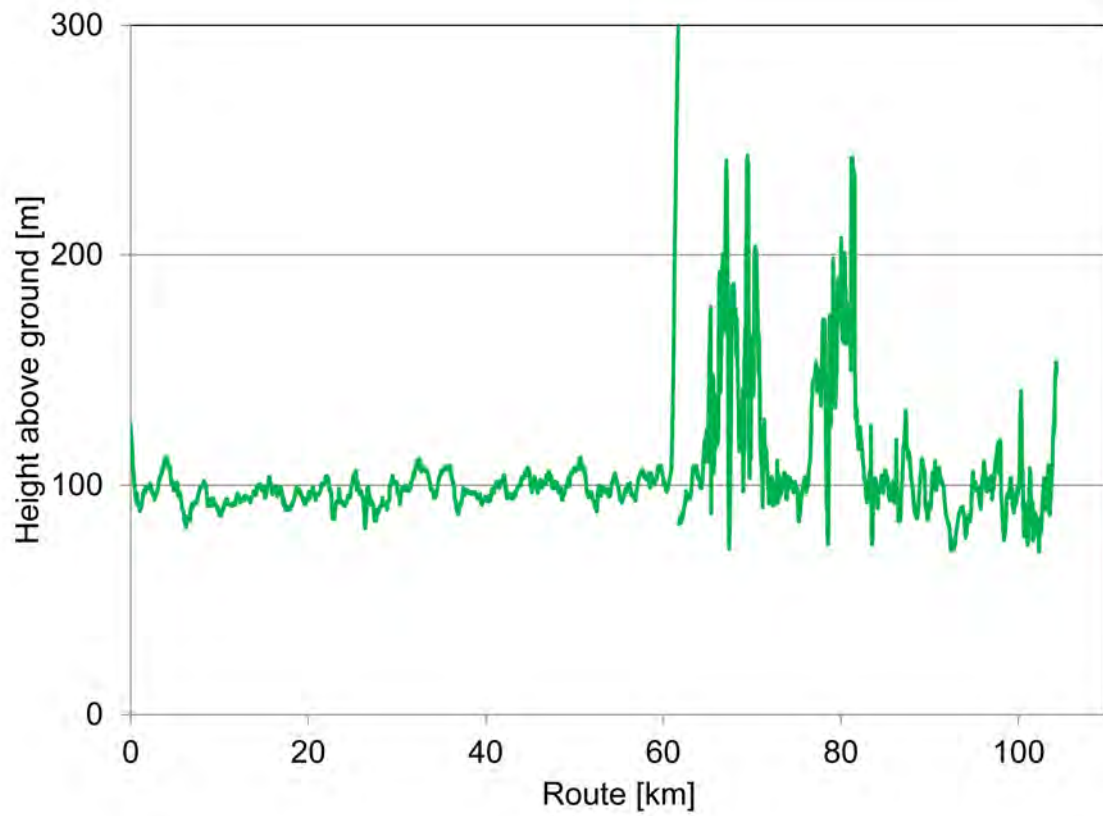
Figure 31: Ground clearance of the profile.
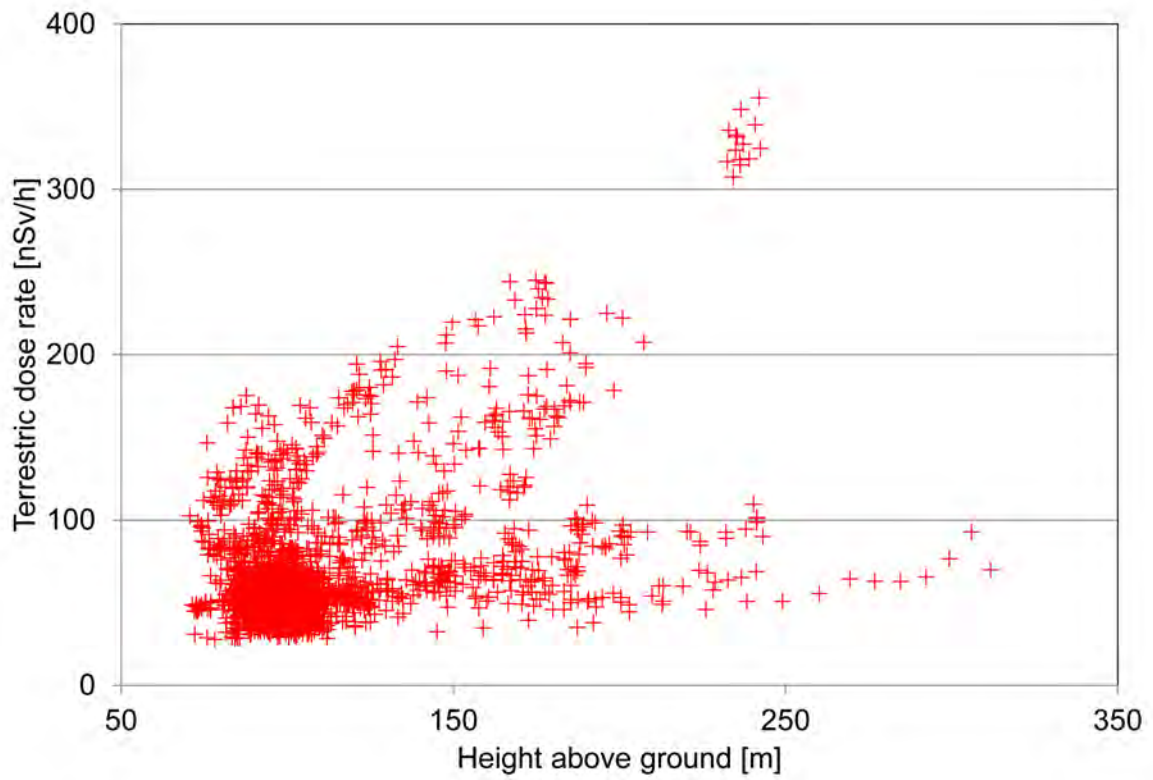
Figure 32: Terrestrial dose rate in dependence on ground clearance without correction of topographic effects.
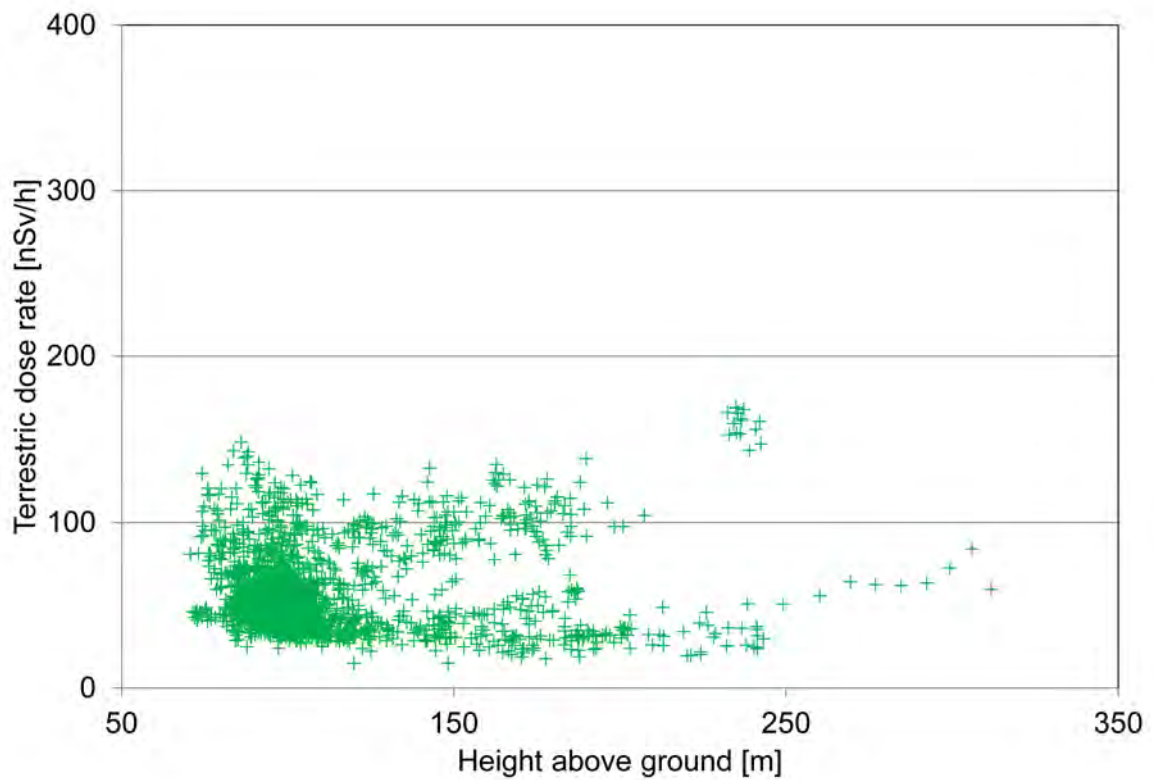
Figure 33: Terrestrial dose rate in dependence on ground clearance with correction of topographic effects.

A profile with a length of 3.6 km was flown at different altitudes above Lake Neuchâtel (elevation 480 m a.s.l.) (Figure 34) with both measuring systems ARM and RLL. The intention of these flights was a reassessment of parameters used to correct for helicopter background and the influence of cosmic radiation in the energy windows used for data evaluation. The evaluation of the measured spectra utilises eight different energy windows (Table 3) together with a single channel summing up all impulses with energies above 3 MeV (cosmic window). The profile was positioned with a minimum distance of 2.5 km from the lake shore to ensure complete attenuation of photons originating from radionuclides in rock and soil. The remaining signal in the detector depends then on an altitude dependent portion originating from cosmic radiation and potentially from airborne radon progeny, and a constant fraction due to radionuclides contained in the detector, the helicopter and the crew. An analysis of the altitude dependence allows to separate between the two components as described in Schwarz, 1991.

The count rate in the energy range above 3 MeV (cosmic window) shows a clear altitude dependence and similar values for both systems ARM and RLL (Figure 35). The count rate in the total window (Figure 36) shows for both systems a clear altitude dependence with different absolute values and slopes of the altitude dependence.

The constant background and height dependent correction for cosmic radiation used in the data evaluation was determined in 2002 from measurements over the English Channel. The expected count rate in the total window is about 20% lower than the measured values (Figure 37). The count rate in the thorium energy window also differs between both systems and the altitude dependence is less clearly pronounced (Figure 38). The applied correction parameters yield good agreement with about 6% higher expected count rates compared to the measured values (Figure 39). The count rates in the potassium window show a similar behaviour as the count rate in the thorium window with an over-correction of 7% (Figures 40 and 41). The count rates in the uranium window show a less consistent altitude dependence and in contrast an under-correction of 34% (Figures 42 and 43). The error bars drawn in Figures 35 to 43 represent the standard deviation of the altitude average, calculated from the standard deviation of all points averaged at the specific altitude divided by the square root of their number reduced by one. The error bars derived for the altitude are too small to be seen in the respective diagrams. A summary of the measured count rates and expectations for the correction is listed for all energy windows in Table 4.

The underestimation of the correction is most distinct in the uranium and caesium energy windows, indicating that airborne radon progeny may have influenced the measurement. These decay products, mainly ^{214}Pb and ^{214}Bi emit photons at multiple energies over the complete energy range (Figure 44). The sum over the emissions in the different energy windows are listed in Table 5 as a first crude estimate of the potential influence of radon progeny in an energy window. For a complete assessment, also Compton scattering and other sources of impulses in the respective energy window would have to be taken into account. Nevertheless, the pattern of significantly underestimated corrections coincides with energy windows containing a larger amount of photon emissions from radon progeny. A direct comparison of the photon spectrum measured at an altitude of 1499 m over Lake Neuchâtel to the spectrum accumulated at an altitude of 1888 m over the Irish sea in 2002 is shown in Figure 45. The peak areas of the photon emissions of ^{40}K at 1460 keV and ^{208}Tl at 2615 keV of both spectra are very similar, especially considering that they were obtained with different detectors and helicopters. These radionuclides can be assigned to the radionuclide content of detector, helicopter and crew. The annihilation peak at 511 keV has as main source the cosmic radiation and the count rate can be expected to be altitude dependent. As the flight altitudes for the accumulation of both spectra are similar, the ob-

served roughly identical peak areas could be expected. In contrast to the spectrum over the Irish sea, various emissions of the short-lived radon decay products ^{214}Pb and ^{214}Bi can be identified in the spectrum acquired over Lake Neuchâtel. This confirms a significant influence of radon progeny on the measurement. The radon progeny interference afflicts especially situations, where the signal originating from terrestrial radionuclides is reduced. The interference of airborne radon progeny can be mitigated with different experimental techniques. Most common is the addition of a detector to the measurement system which is shielded in the downward direction (up-looking detector) to measure airborne gamma emitters directly. This solution was discussed as an improvement to the ARM system in the past. Unfortunately, the Super Puma helicopter used with ARM and RLL systems has engines located on top of the passenger and cargo space. The material of the massive engines shields a detector against photon radiation coming from above, rendering the installation of an up-looking detector in the cargo bay or the passenger area ineffective. Thus, an appropriate method for a quantitative correction of airborne radionuclides has still to be found.
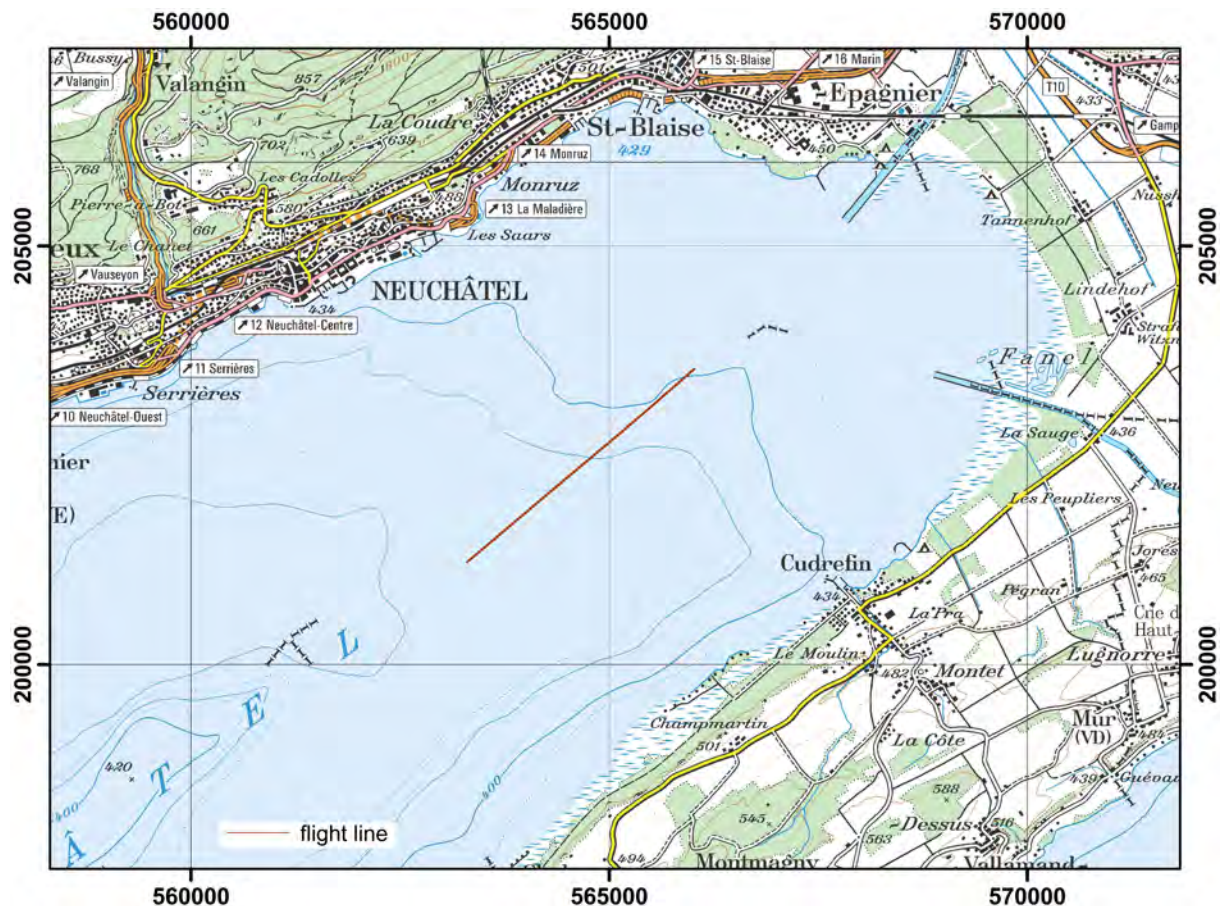
Figure 34: Flight line of the profile above Lake Neuchâtel.
PK100 ©2016 swisstopo (JD100042).

Window	Lower energy limit [keV]	Upper energy limit [keV]	Peak energy [keV]
Total	400	3000	-
Potassium (^{40}K)	1369	1558	1461
Uranium (^{214}Bi)	1664	1853	1765
Thorium (^{208}Tl)	2407	2797	2615
Caesium (^{137}Cs)	600	720	662
Cobalt (^{60}Co)	1100	1400	1173, 1332
MMGC1	400	1400	-
MMGC2	1400	3000	-

Table 3: Energy windows for data evaluation.
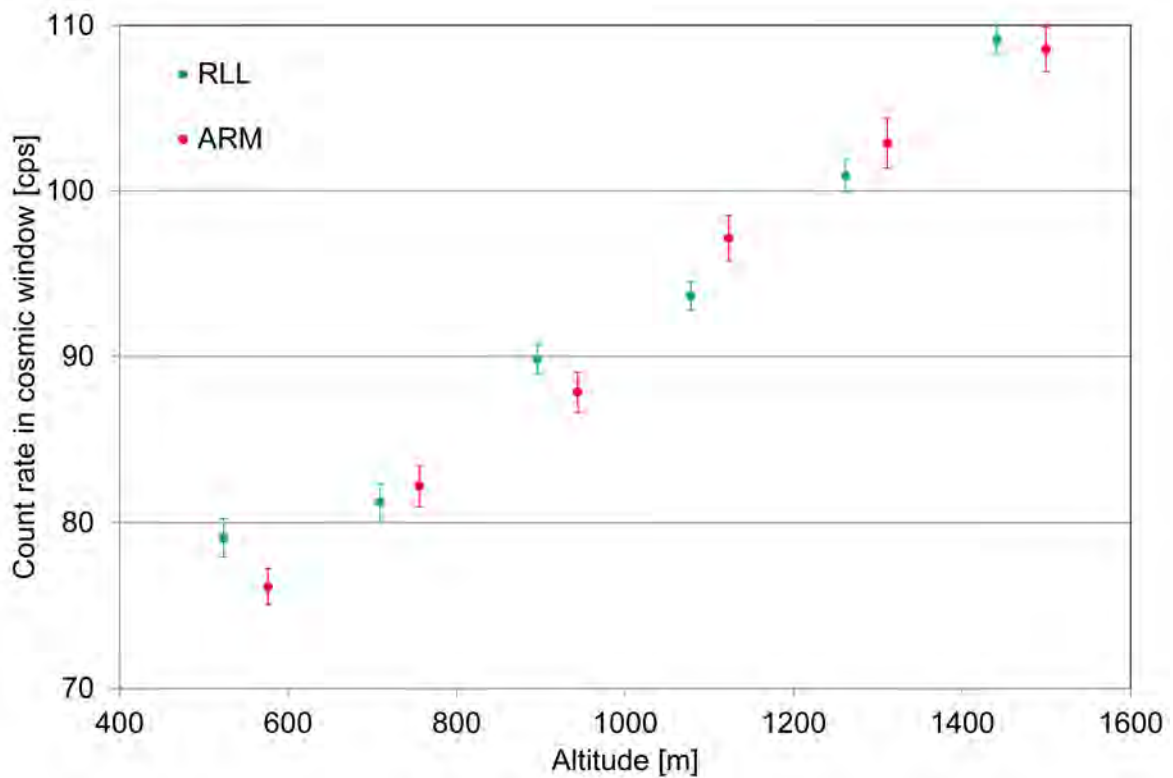
Figure 35: Count rate in the cosmic window in dependence on flight altitude. The depicted error bars represent the standard deviation of the average.
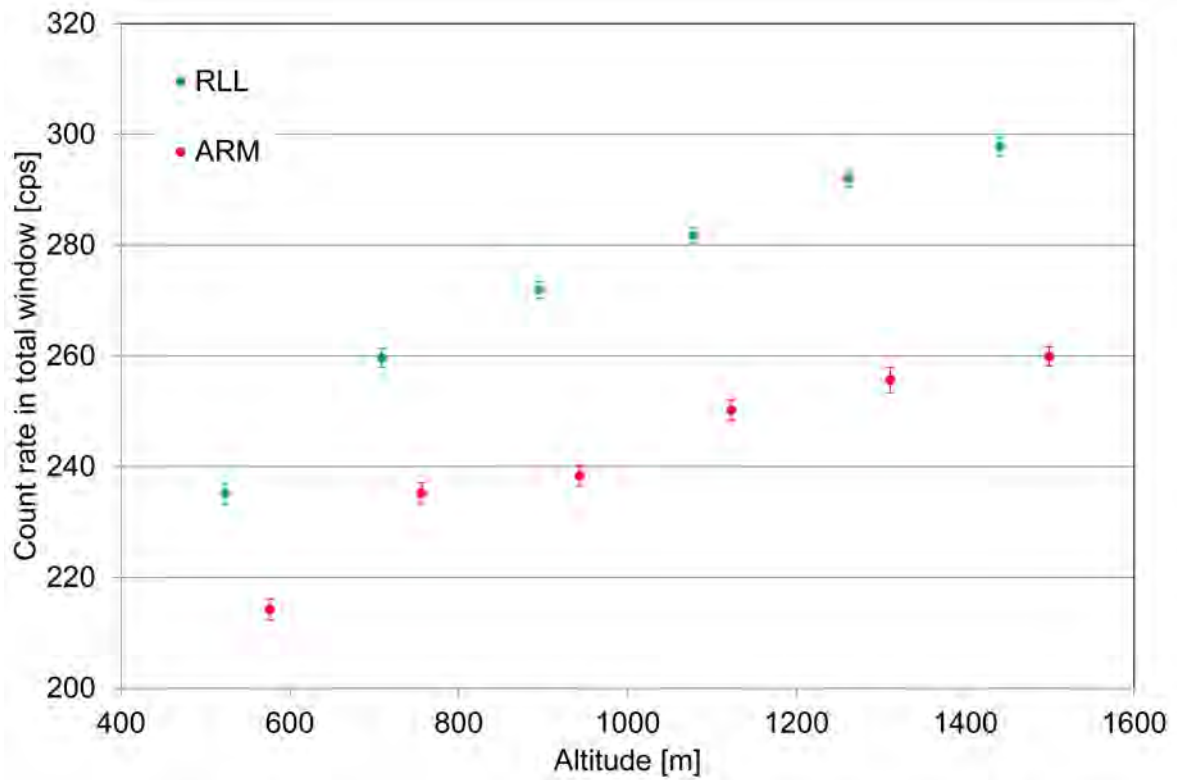
Figure 36: Count rate in the total window in dependence on flight altitude. The depicted error bars represent the standard deviation of the average.
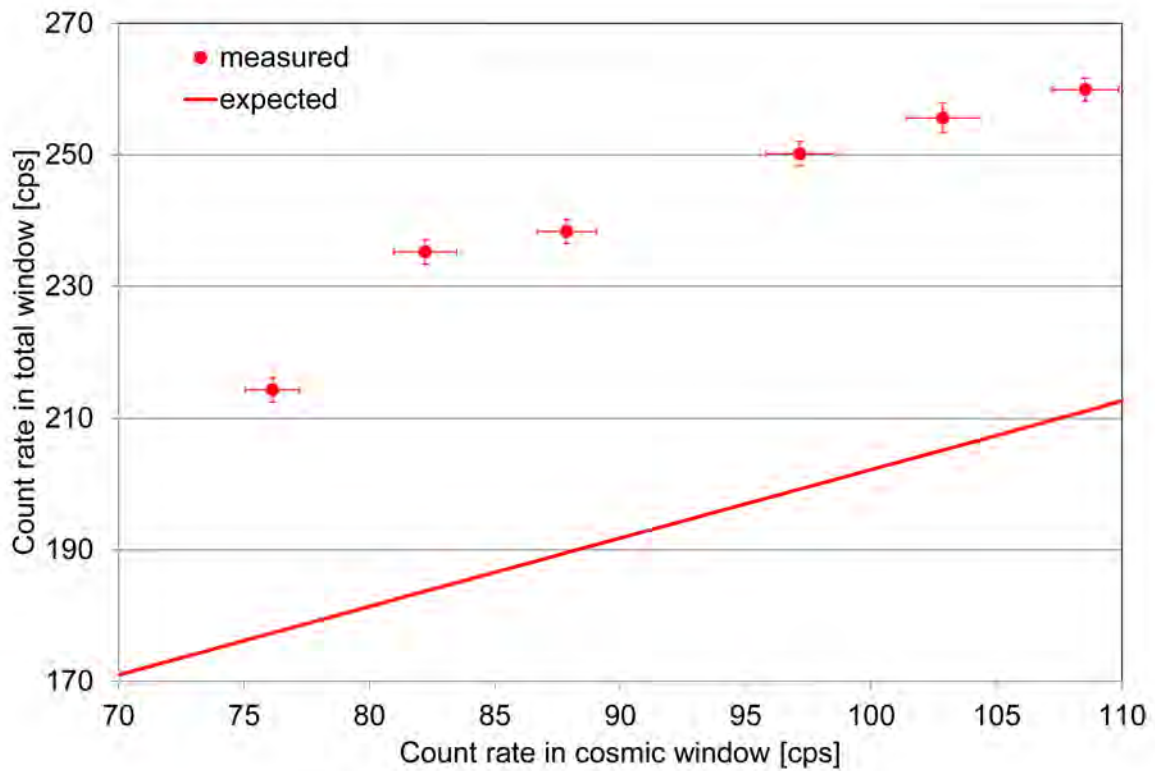
Figure 37: Count rate in the total window in dependence on the count rate in the cosmic window. The depicted error bars represent the standard deviation of the average.
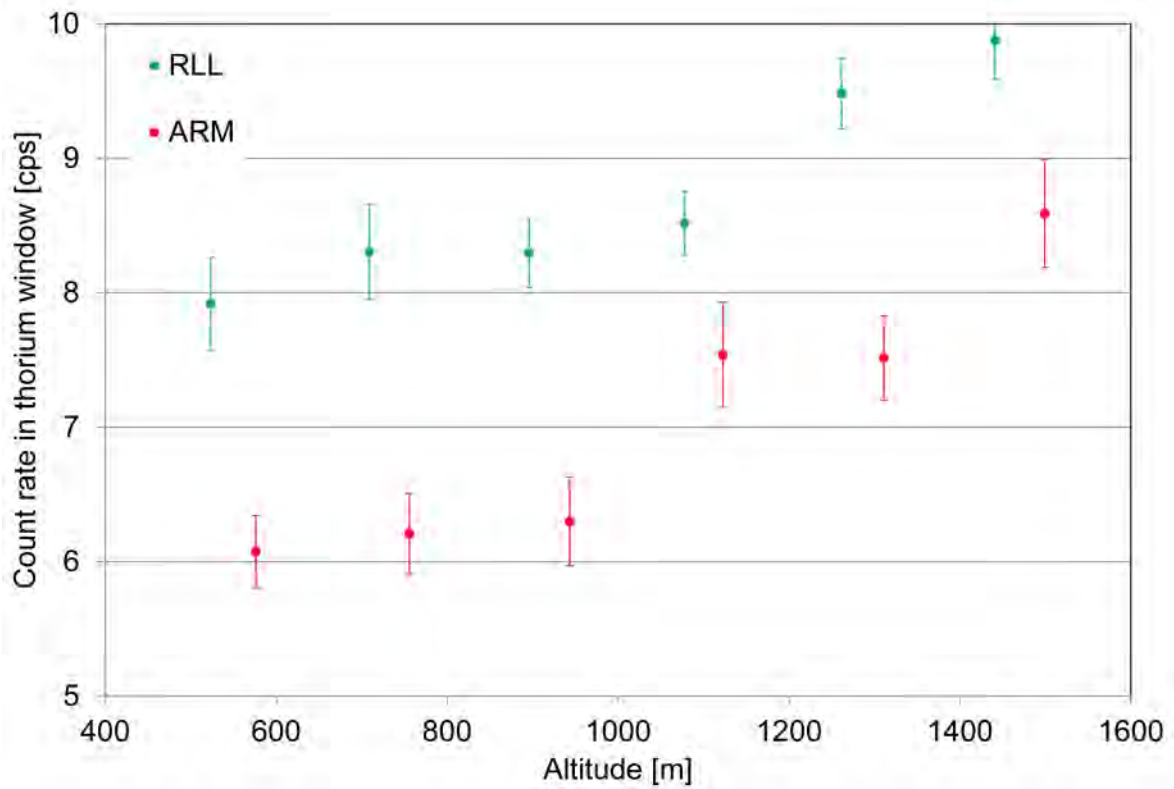
Figure 38: Count rate in the thorium window in dependence on flight altitude. The depicted error bars represent the standard deviation of the average.
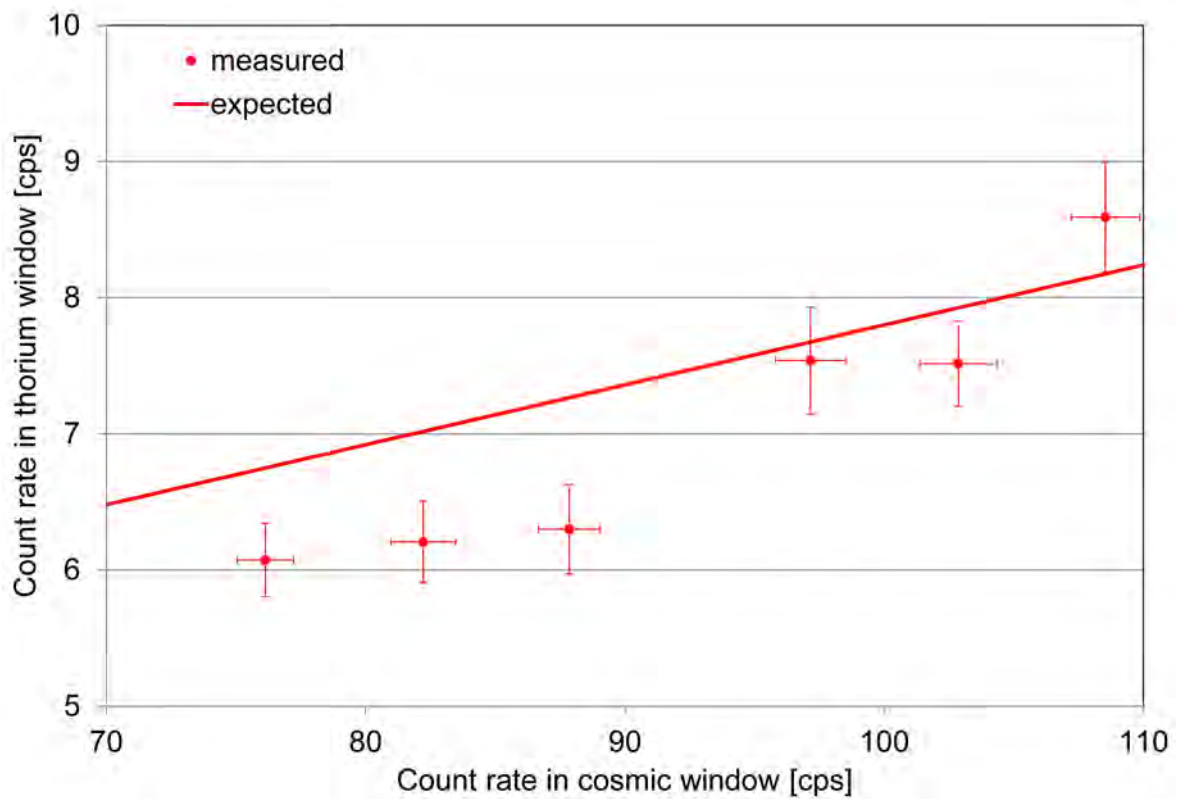
Figure 39: Count rate in the thorium window in dependence on the count rate in the cosmic window. The depicted error bars represent the standard deviation of the average.
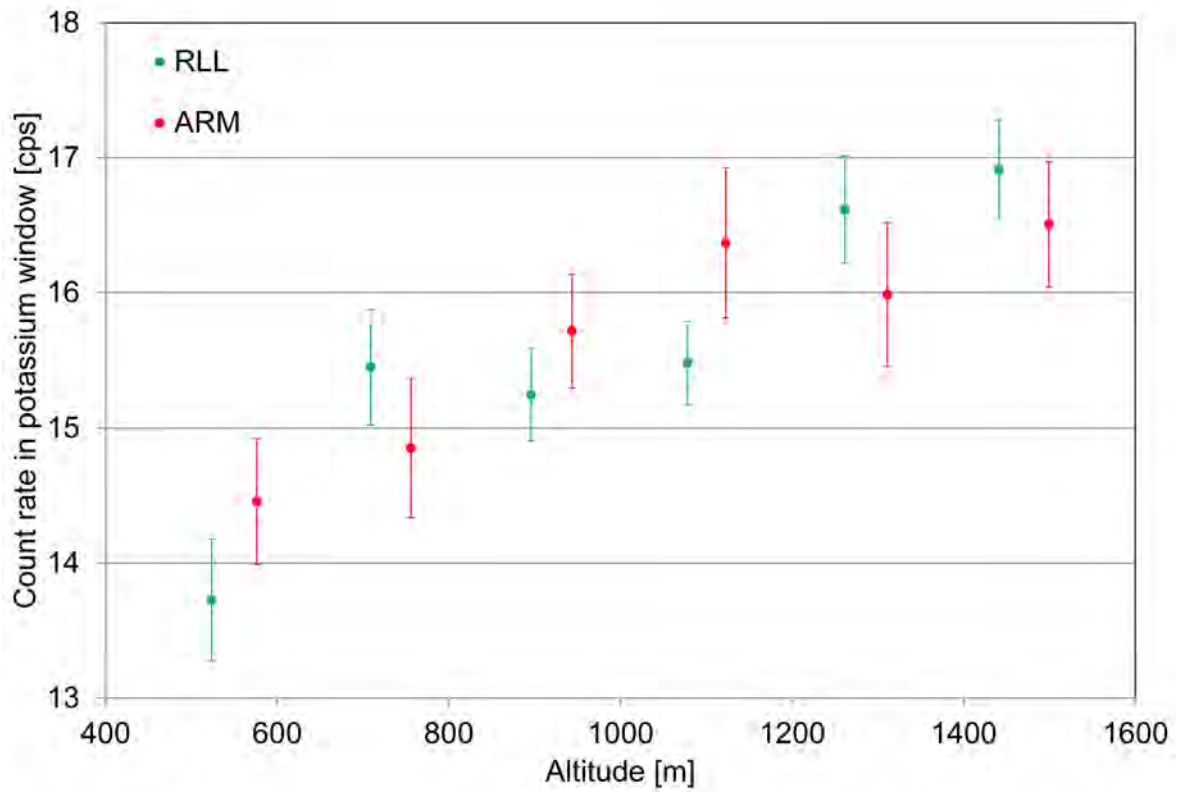
Figure 40: Count rate in the potassium window in dependence on flight altitude. The depicted error bars represent the standard deviation of the average.
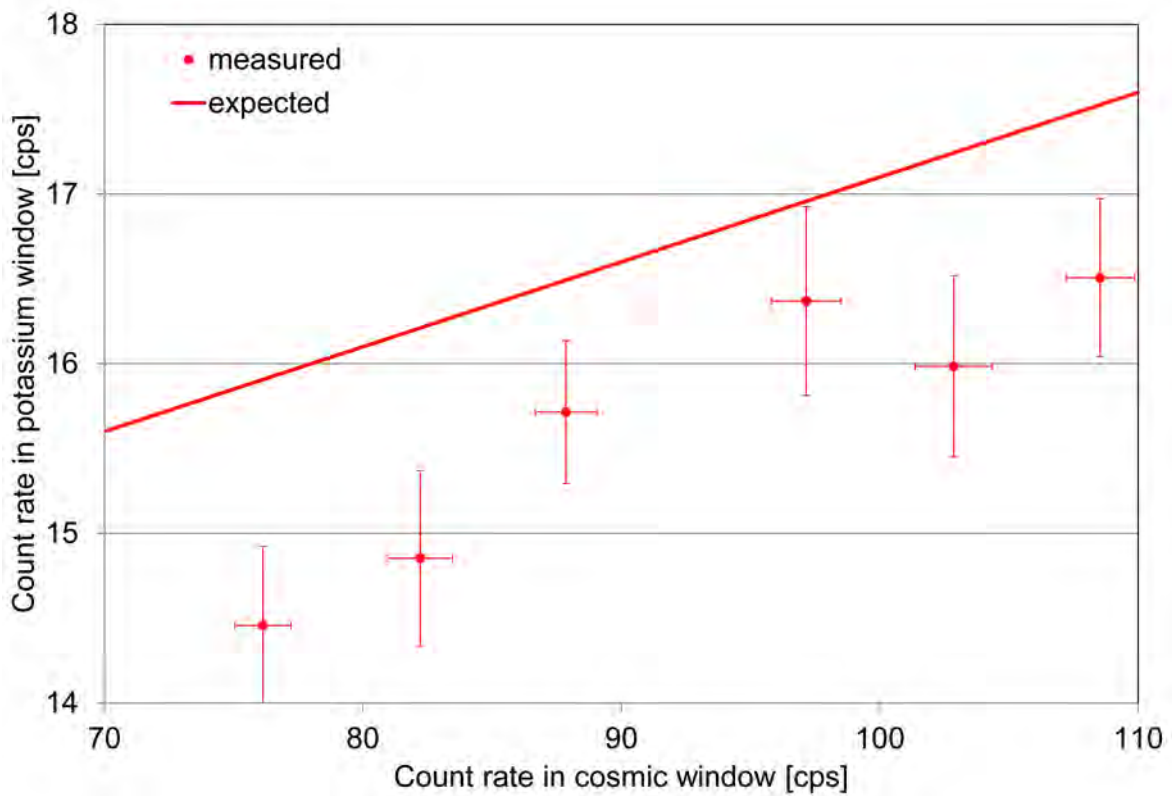
Figure 41: Count rate in the potassium window in dependence on the count rate in the cosmic window. The depicted error bars represent the standard deviation of the average.
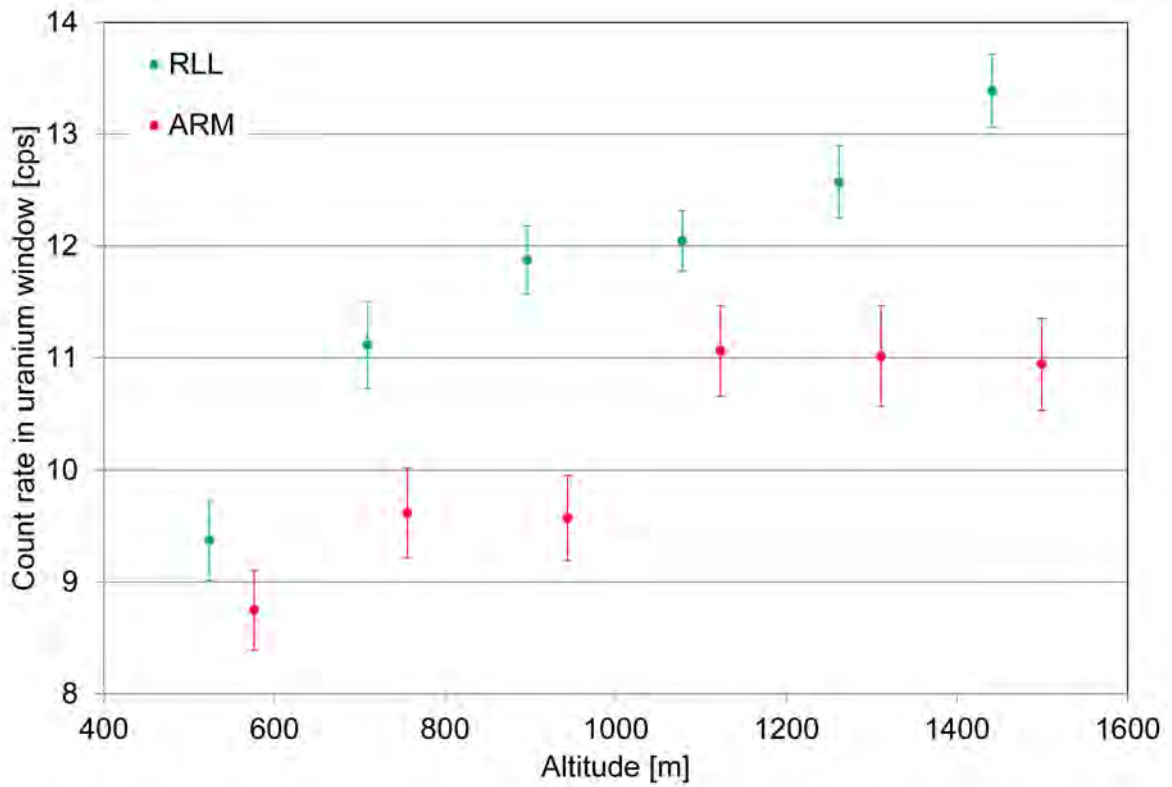
Figure 42: Count rate in the uranium window in dependence on flight altitude. The depicted error bars represent the standard deviation of the average.
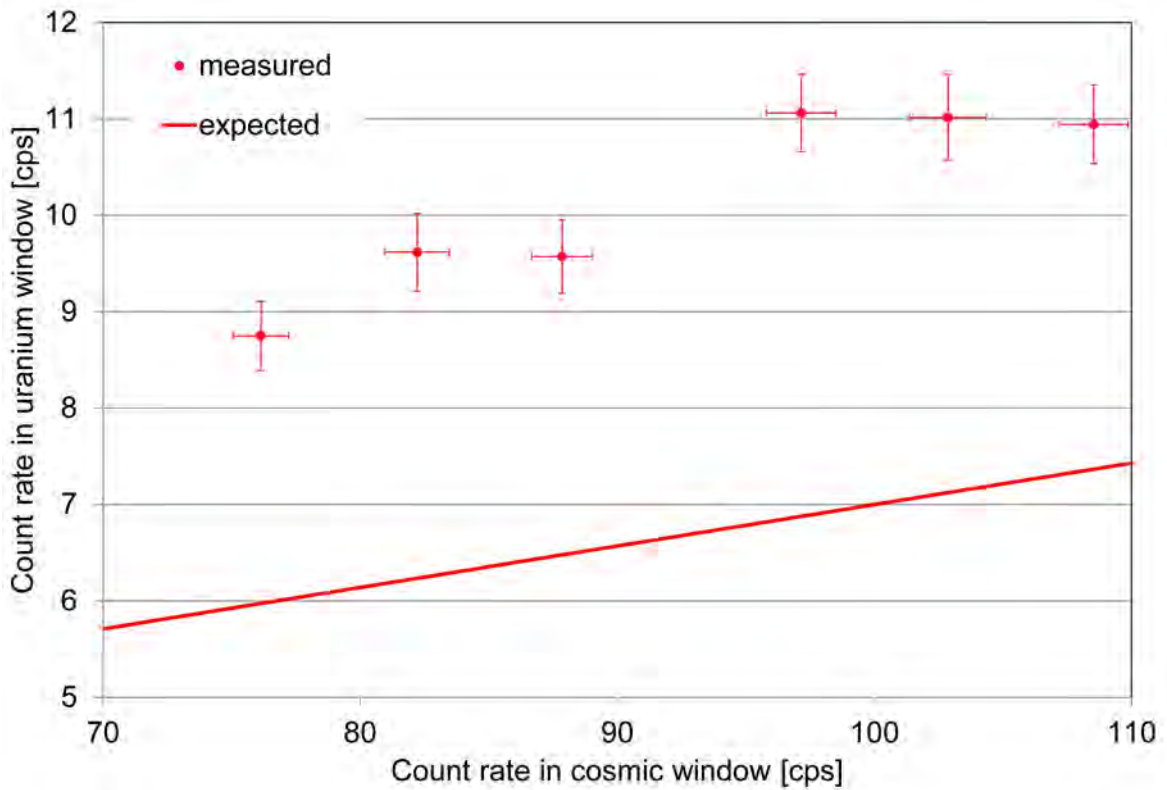
Figure 43: Count rate in the uranium window in dependence on the count rate in the cosmic window. The depicted error bars represent the standard deviation of the average.

37

Window	measured count rate RLL [cps]	measured count rate ARM [cps]	expected count rate ARM [cps]	relative deviation ARM [%]
Total	273	242	194	+20
Potassium (^{40}K)	15.6	15.6	16.7	-7
Uranium (^{214}Bi)	11.7	10.2	6.7	+34
Thorium (^{208}Tl)	8.7	7.0	7.5	-6
Caesium (^{137}Cs)	36.7	36.3	24.9	+31
Cobalt (^{60}Co)	28.1	26.1	23.2	+11
MMGC1	217	192	151	+21
MMGC2	56	51	44	+14

Table 4: Count rates averaged over altitudes.
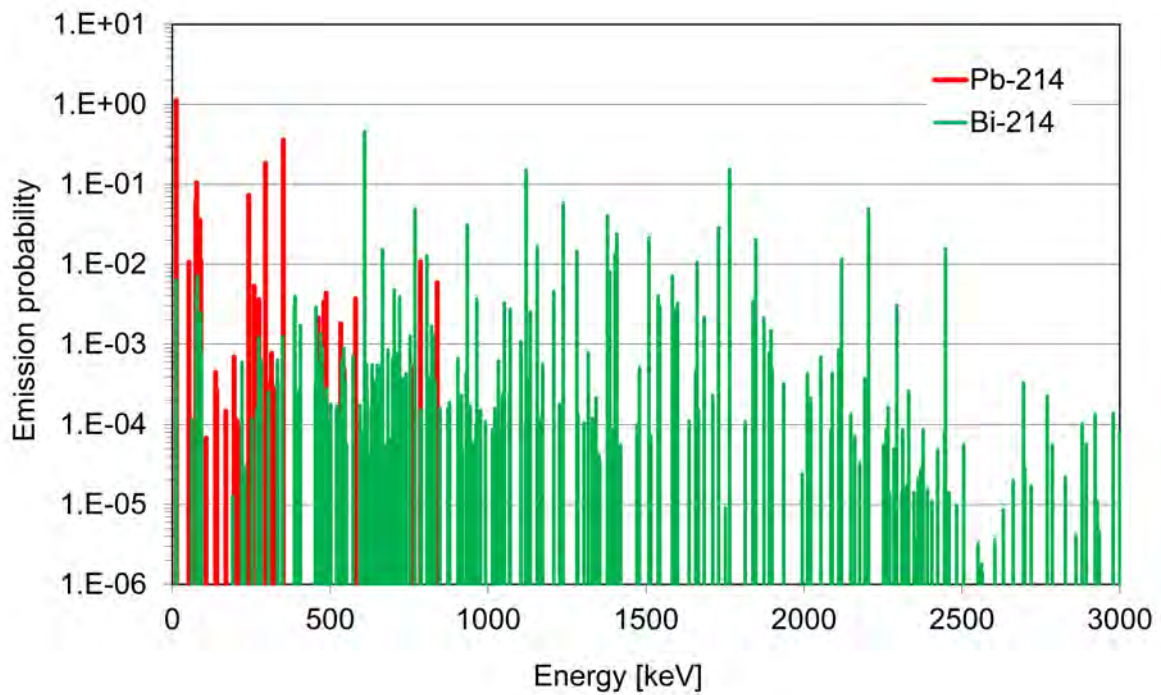
Figure 44: Photon emissions of the radon decay products ^{214}Pb and ^{214}Bi.

Window	Summed emission probabilities
Total	1.33
Potassium (^{40}K)	0.11
Uranium (^{214}Bi)	0.21
Thorium (^{208}Tl)	0.02
Caesium (^{137}Cs)	0.49
Cobalt (^{60}Co)	0.30
MMGC1	0.94
MMGC2	0.39

Table 5: Photon emissions of radon progeny in the different energy windows.
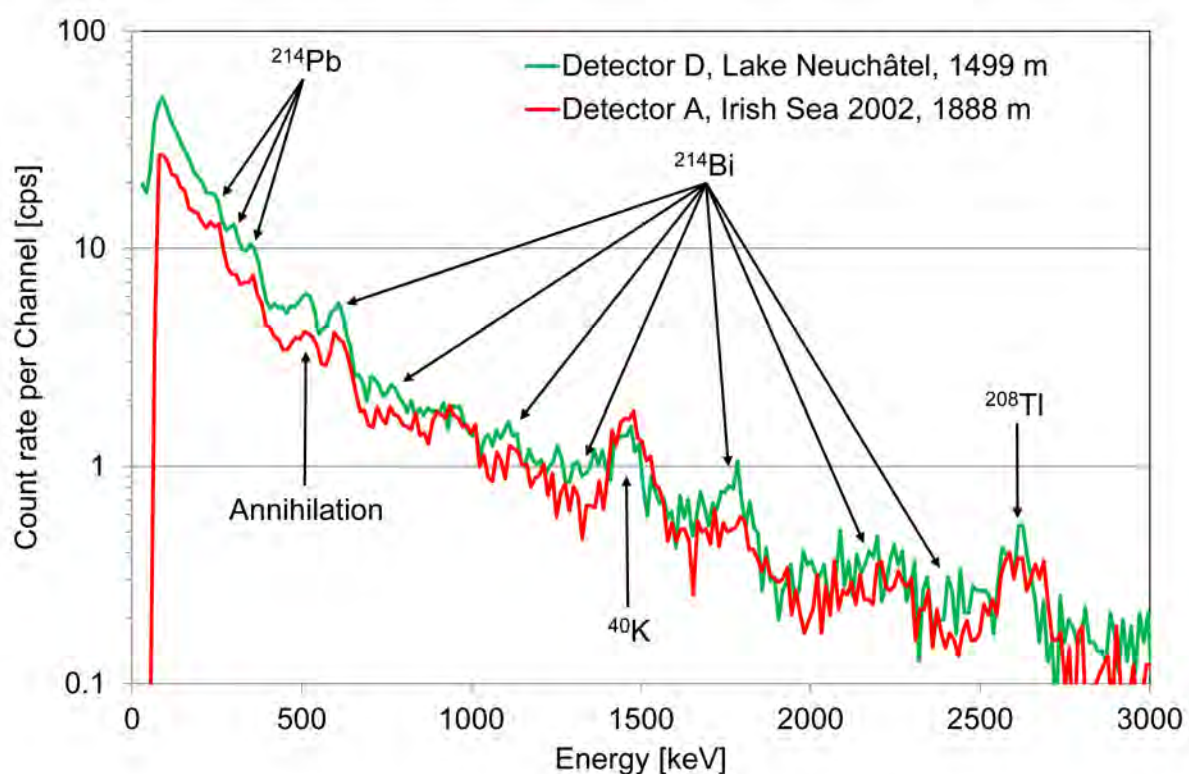
Figure 45: Photon spectra over Lake Neuchâtel and the Irish sea.

The third test of the influence of measuring height was located in the Limpach valley (Figure 46). A profile of 10 km length was measured in three different heights above ground (standard measuring height 90 m, 270 m and 540 m) with both ARM and RLL systems. Table 6 lists the results of the flights with both systems ARM and RLL averaged over the complete profile at the respective height above ground. The dose rate, which is the extrapolated value expected at one meter above ground, agrees well for the first two heights and deviates to higher values at the highest flight level for both systems. The averages of ^{40}K activity concentration show a different behaviour of decreasing values with increasing height above ground for both systems. Especially the negative value at the highest flight level for the ARM system indicates an over-correction of the gross counts in the potassium

energy window. As the flights over Lake Neuchâtel confirmed the background and cosmic correction in this energy window, the potential cause can be narrowed down to the height dependent stripping correction factors, potentially in combination with the influence of airborne radionuclides. The spectra averaged over the profile at the measuring heights are depicted in Figures 47 and 48. The spectrum of the RLL system is divided in 1024 channels compared to the 256 channels of the ARM system, thus reducing the count rates per channel by a factor of four. The RLL system shows between 15% and 20% higher count rates than the ARM system. The shape of the spectra measured with both system is nearly identical with a slight energy drift observed between the different spectra of the RLL system. The presence of photons from radon progeny is clearly visible in both spectra. For a further quantification, the net peak area of relevant photo-peaks in the spectra averaged over the profile at each height was analysed. Due to the low energy resolution of the NaI(Tl)-Detectors and the low count rates, these net peak areas have to be associated with a large uncertainty. Table 7 shows for the terrestrial radionuclides ^{40}K and ^{208}Tl a strong decrease of net peak areas with increasing height above ground. The decrease of the net peaks areas of two evaluated photo peaks of emissions from the radon decay product ^{214}Bi with measuring height is much less pronounced, indicating an interference of airborne radon progeny.
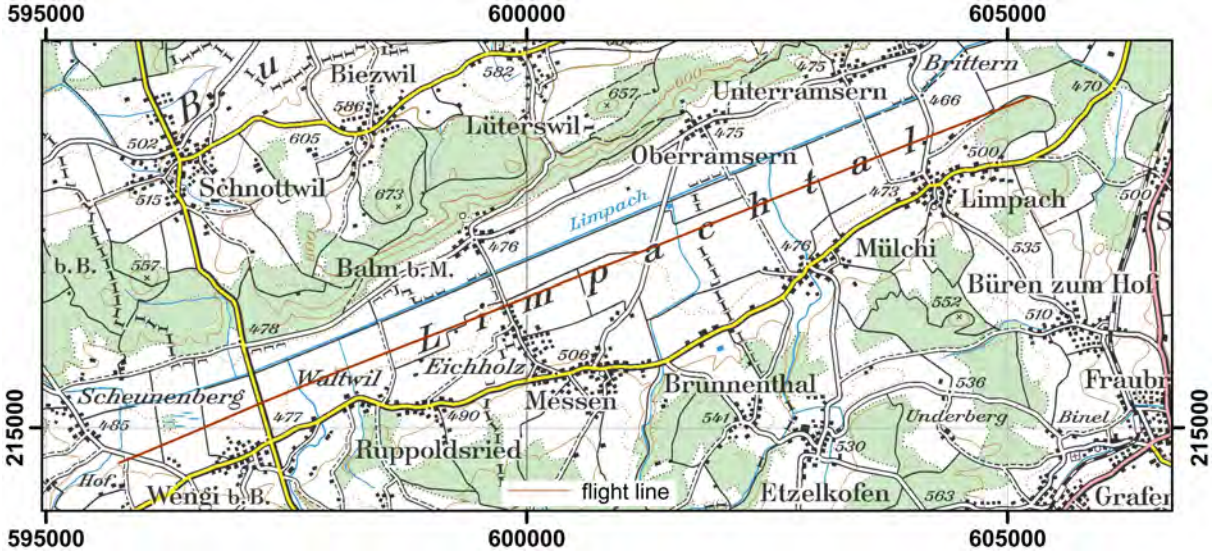
Figure 46: Flight line of the profile above Limpach Valley.
PK100 ©2016 swisstopo (JD100042).

Height above ground [m]	90	270	540
Average			
Dose rate ARM [nSv/h]	114	113	140
Dose rate RLL [nSv/h]	116	118	172
^{40}K activity concentration ARM [Bq/kg]	424	280	-81
^{40}K activity concentration RLL [Bq/kg]	309	289	181
^{232}Th activity concentration ARM [Bq/kg]	29	26	11
^{232}Th activity concentration RLL [Bq/kg]	25	31	58
^{238}U activity concentration ARM [Bq/kg]	48	63	132
^{238}U activity concentration RLL [Bq/kg]	30	49	129

Table 6: Results of the measuring flights averaged over the profile at different heights.
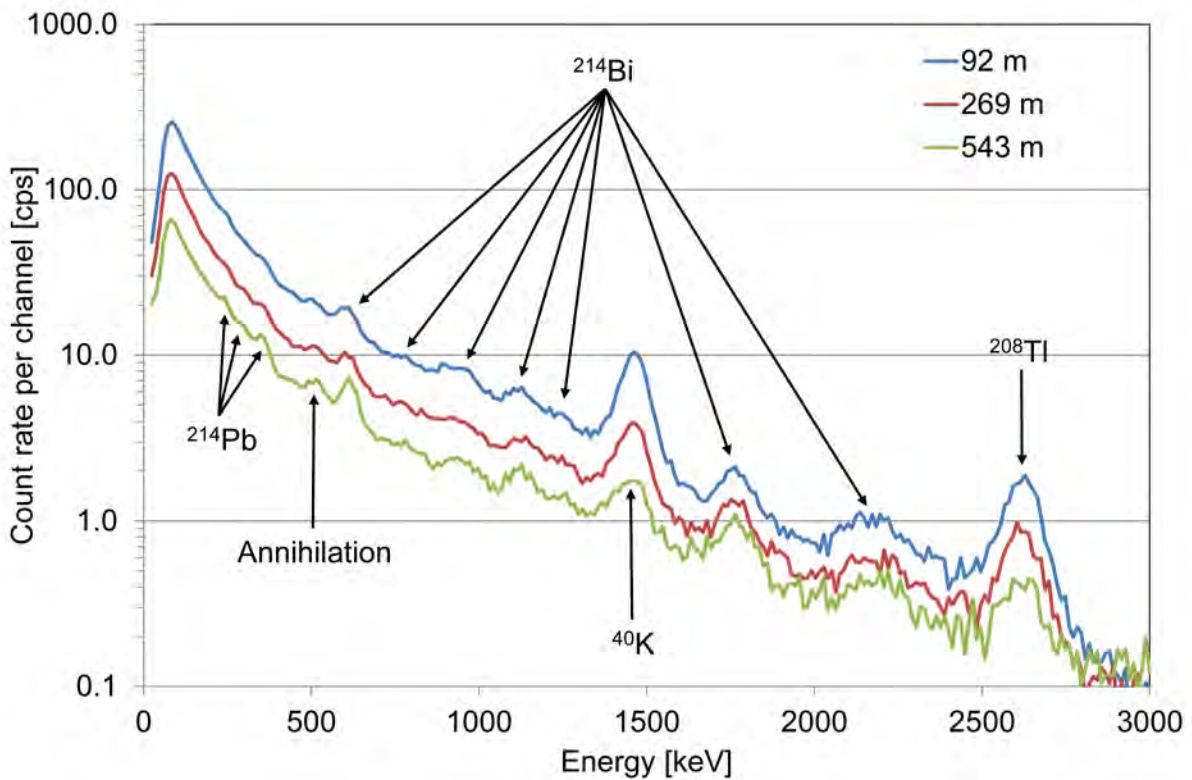
Figure 47: Photon spectra over Limpach valley in three heights above ground measured with the ARM system.
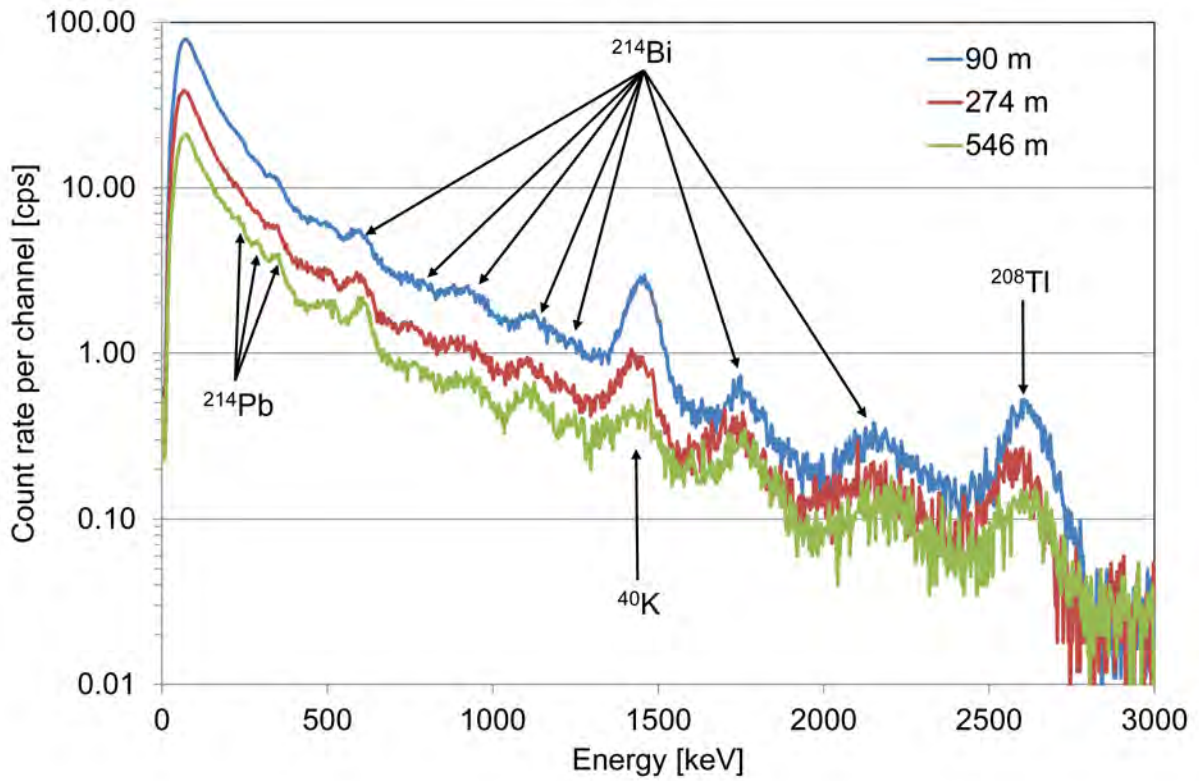
Figure 48: Photon spectra over Limpach valley in three heights above ground measured with the RLL system.

Height above ground [m]	90	270	540
Photon peak			
1460 keV (^{40}K) ARM	83	26	5.3
1460 keV (^{40}K) RLL	95	25	6.6
2615 keV (^{208}Tl) ARM	13	4.8	1.4
2615 keV (^{208}Tl) RLL	13	6.4	1.3
609 keV (^{214}Bi) ARM	24	10.9	12.0
609 keV (^{214}Bi) RLL	32	17.0	14.1
1765 keV (^{214}Bi) ARM	8.9	4.7	4.1
1765 keV (^{214}Bi) RLL	9.6	7.1	5.2

Table 7: Net peak areas in counts per second of photon peaks at different heights.

2.7 Intercomparison measurements ARM and RLL over PSI

The ARM system could prove during the last twenty years its merits in multiple intercomparisons with ground measurements and foreign airborne gamma-spectrometry systems, thus providing a reference for the assessment of the RLL system. The vicinity of the Paul Scherrer Institute was established as testing site in past intercomparisons of the systems. The accelerator and intermediate storage facilities located on the institute premises render photon emissions detectable with airborne gamma-spectrometry. Close to PSI at Rotbergegg, a known ^{232}Th-anomaly yields signals associated with elevated concentrations of natural radionuclides. Additionally, radioactive sources can be placed temporarily on the Institute premises by radiation protection staff of PSI to study the response of the airborne gamma-spectrometry systems to point source activity.

The dose rate maps of both systems (Figures 49 and 50) show very similar values with elevated values over the accelerator facility and the positions of two radioactive sources placed on the institute premises for this test. Slightly elevated values are observed over Rotbergegg. The different density of measuring points measured with the RLL and ARM system over this area does not influence the comparability of results. The maps of the MMGC-ratio (Figures 51 and 52), an indicator for the presence of artificial radionuclides, show normal values over the ^{232}Th-anomaly at Rotbergegg as expected. Over both parts of the institutes west and east of the river Aare elevated values of the MMGC-ratio are observed. These can be attributed to the airborne releases already described in subsection 2.1, the accelerator building, an intermediate storage facility and the two test radioactive sources. Maps of the activity estimated for ^{137}Cs-point sources (Figures 53 and 54) indicate the location of the placed source. The maximum of the point source activity determined with the RLL system is located slightly to the north of the real source position. Compared with the real activity of 3.4 GBq, the maximum point source activity of ^{137}Cs determined with the ARM system of 4.8 GBq overestimated the activity of the source by 40%, whereas the point source activity estimated with the RLL system of 1.8 GBq is 47% below the real value. The distribution of ^{60}Co-point source activity differs between the evaluations of the ARM and RLL systems (Figures 55 and 56). The ARM system indicates ^{60}Co activity over the ^{60}Co-point source, over the accelerator and over a storage building located at the eastern part of PSI.

The spectra are averaged for both systems for further information. Figure 57 shows spectra of both systems over areas without signals originating from elevated activities of natural or artificial radionuclides. Due to the different number of channels used storing spectra (ARM: 256 channels; RLL: 1024 channels), the count rate per channel of the ARM system is about four times larger compared to the value of the RLL system. The photo-peaks of the natural radionuclides ^{40}K and ^{208}Tl are clearly visible in both spectra. The spectrum of the ARM system shows additionally a small peak at 511 keV, which can be associated with the waste air of the accelerator located in the western part of PSI. The spectra measured over the location of the ^{60}Co-point source indicate the photon emissions at 1173 keV and 1332 keV of ^{60}Co for both systems (Figure 58). Over a storage building located in the eastern part of PSI, the ARM system detects a clear signal of ^{60}Co (Figure 59). The ^{60}Co-signal is much less pronounced in the spectrum measured at the same location with the RLL system. The spectra measured over the accelerator building (Figure 60) show clearly the annihilation radiation caused by short-lived positron emitters generated through activation. The spectrum accumulated with the RLL system shows a small elevation at the photon energy emitted by ^{137}Cs, which may be caused by the point source placed in the vicinity of the accelerator building. The count rate in the energy window used for the detection of ^{60}Co (1100 keV - 1400 keV) shows increased count rates for both systems, but the clear separation of the

photo peaks at 1173 keV and 1332 keV is missing. This may be caused by the radionuclide ^{41}Ar, an activation product of the accelerator, which is emitted from the stack of the accelerator building together with the already mentioned positron emitters. The main gamma emission of ^{41}Ar at 1294 keV obscures the minimum between the two ^{60}Co-photo peaks.

Thus, the interpretation as ^{60}Co activity derived by the ARM system can be judged valid according to the spectra. In contrast, the RLL system solely identifies ^{60}Co activity at the location of the placed source, even when slightly elevated count rates in the ^{60}Co-energy window can be identified in the spectrum. A possible reason for the missing ^{60}Co identifications at the two other locations besides the ^{60}Co-source may be the treatment of values below the decision threshold of the measurement system. It can be assumed from the data that values below the decision threshold were zeroised in the RLL software.

The ^{60}Co-point source activity determined with the ARM system was 300 MBq, about 15% larger than the real activity of the placed source of 260 MBq. The RLL system estimated the activity to about half the real value (120 MBq).

The ^{232}Th-anomaly at Rotbergegg is clearly visible in the respective maps of both systems (Figures 61 and 62). A scattergram of RLL versus ARM values for points with a distance less than twenty meters (Figure 63) shows in average about 18% lower values for the RLL system.
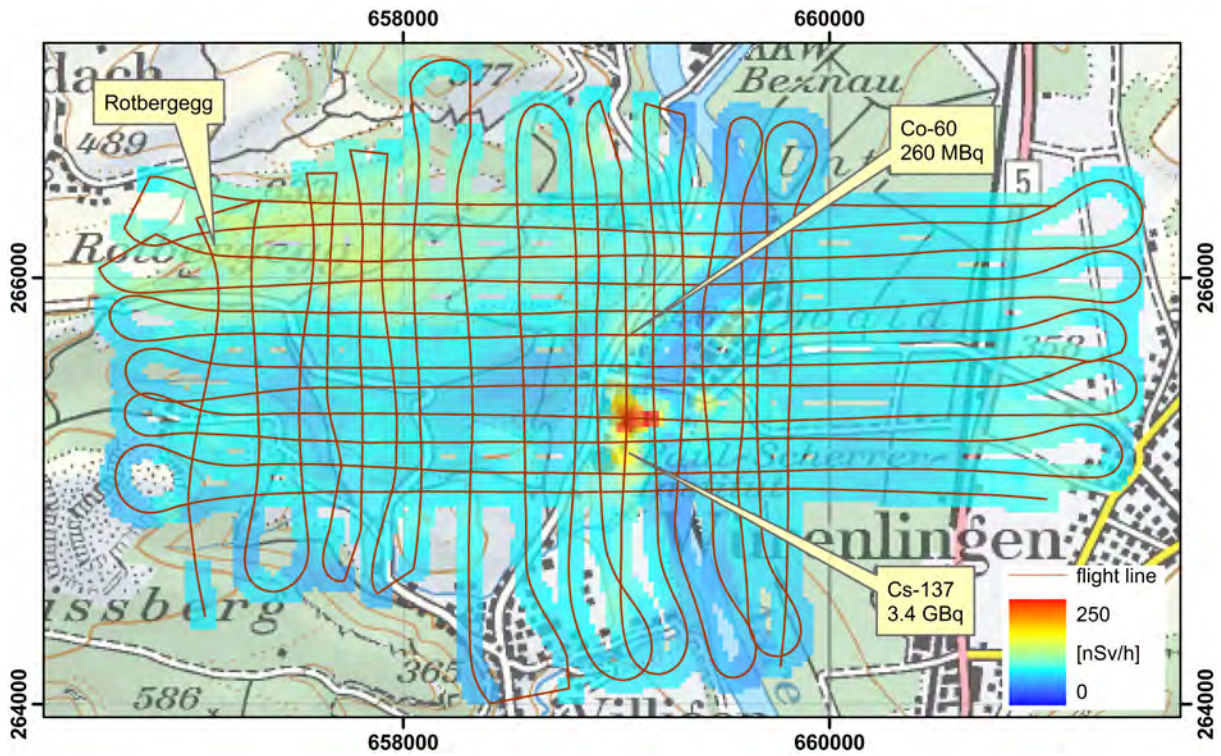
Figure 49: Dose rate of the test measurements over the vicinity of PSI measured with the ARM system.
PK100 ©2016 swisstopo (JD100042).
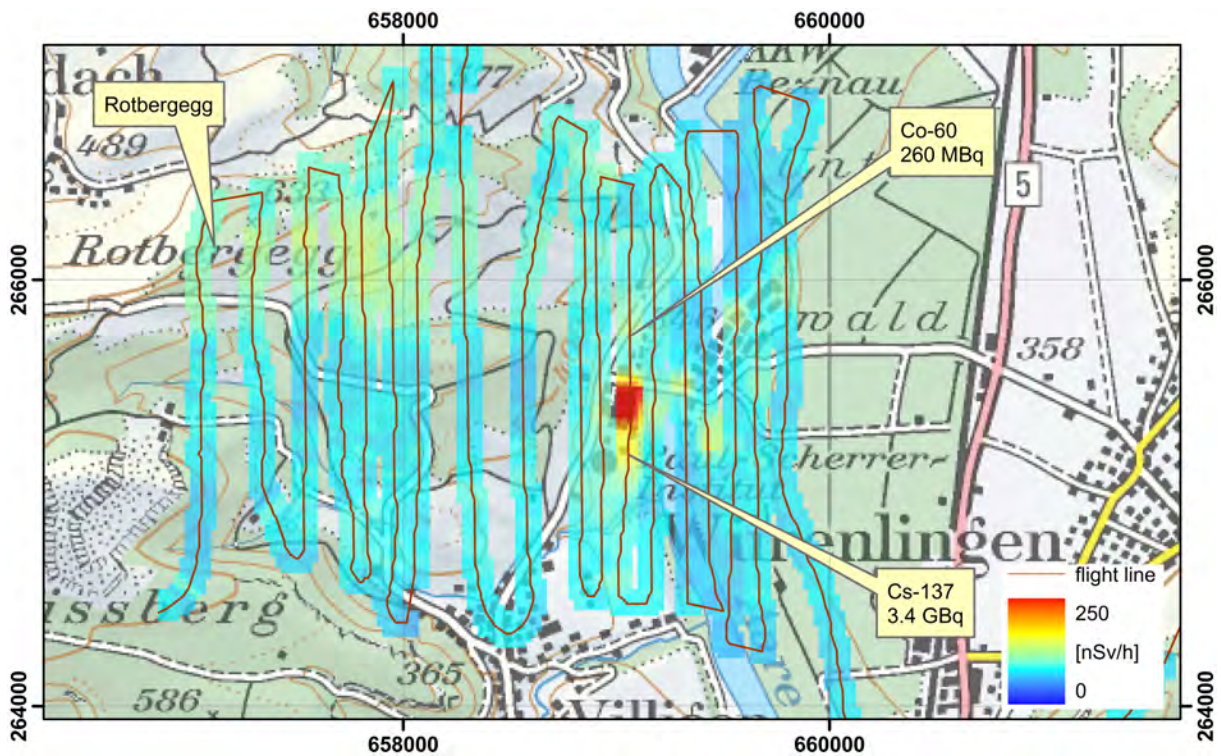
Figure 50: Dose rate of the test measurements over the vicinity of PSI measured with the RLL system.
PK100 ©2016 swisstopo (JD100042).
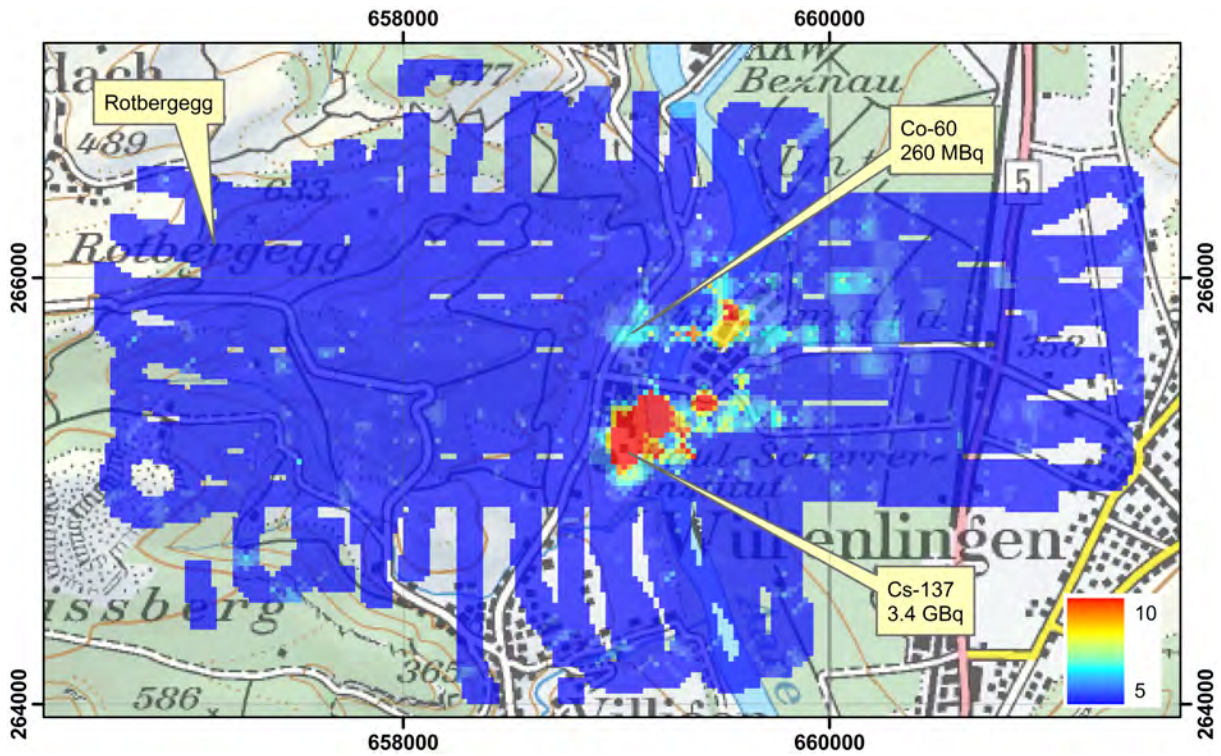
Figure 51: MMGC-ratio of the test measurements over the vicinity of PSI measured with the ARM system.
PK100 ©2016 swisstopo (JD100042).
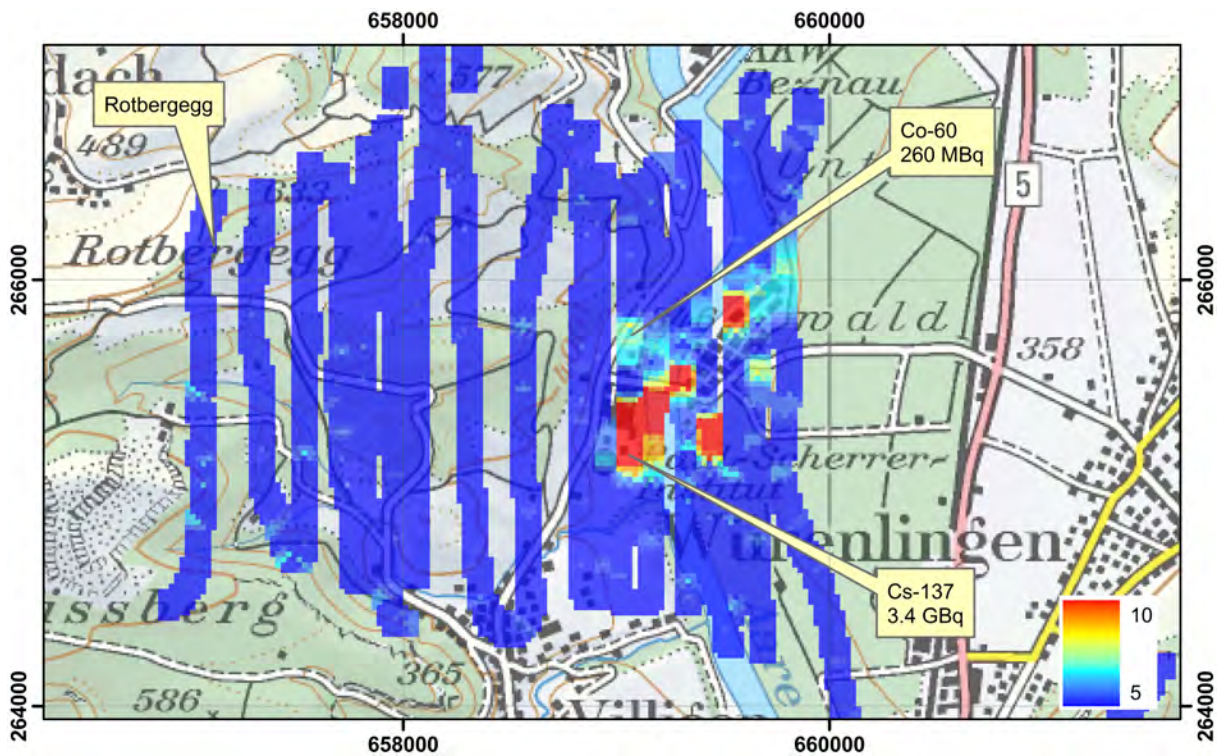
Figure 52: MMGC-ratio of the test measurements over the vicinity of PSI measured with the RLL system.
PK100 ©2016 swisstopo (JD100042).
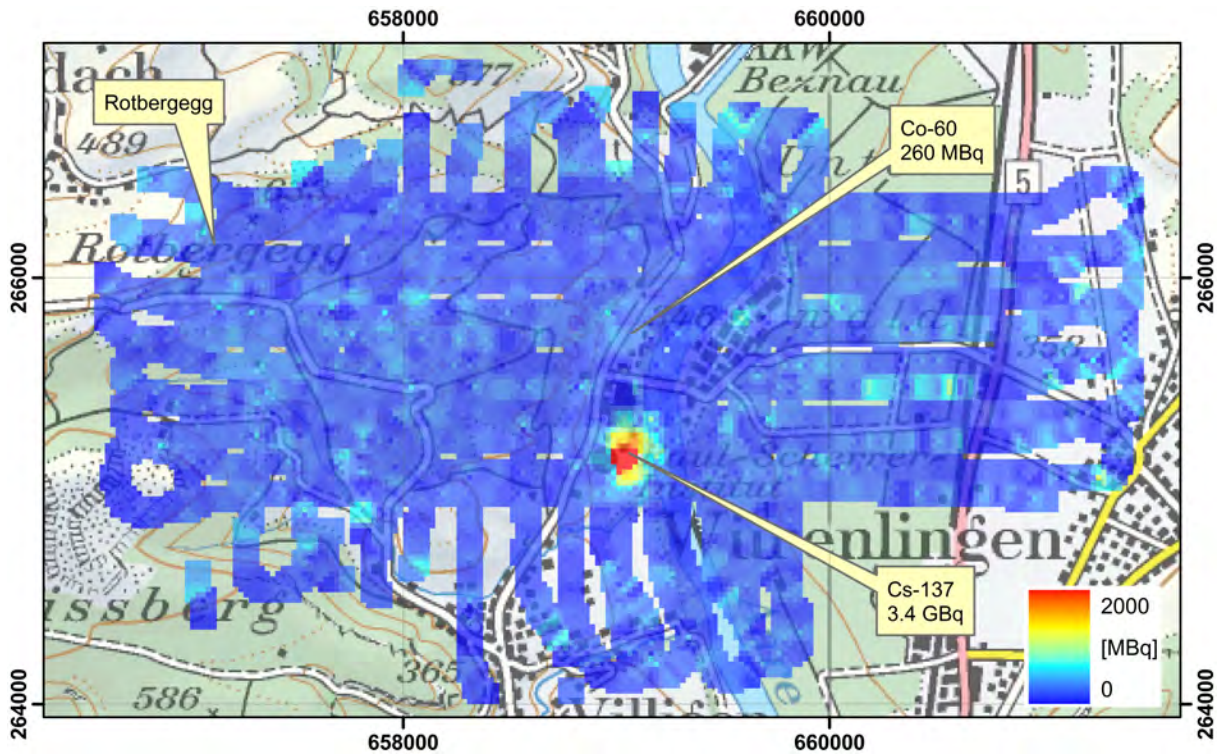
Figure 53: ^{137}Cs-point source activity of the test measurements over the vicinity of PSI measured with the ARM system.
PK100 ©2016 swisstopo (JD100042).
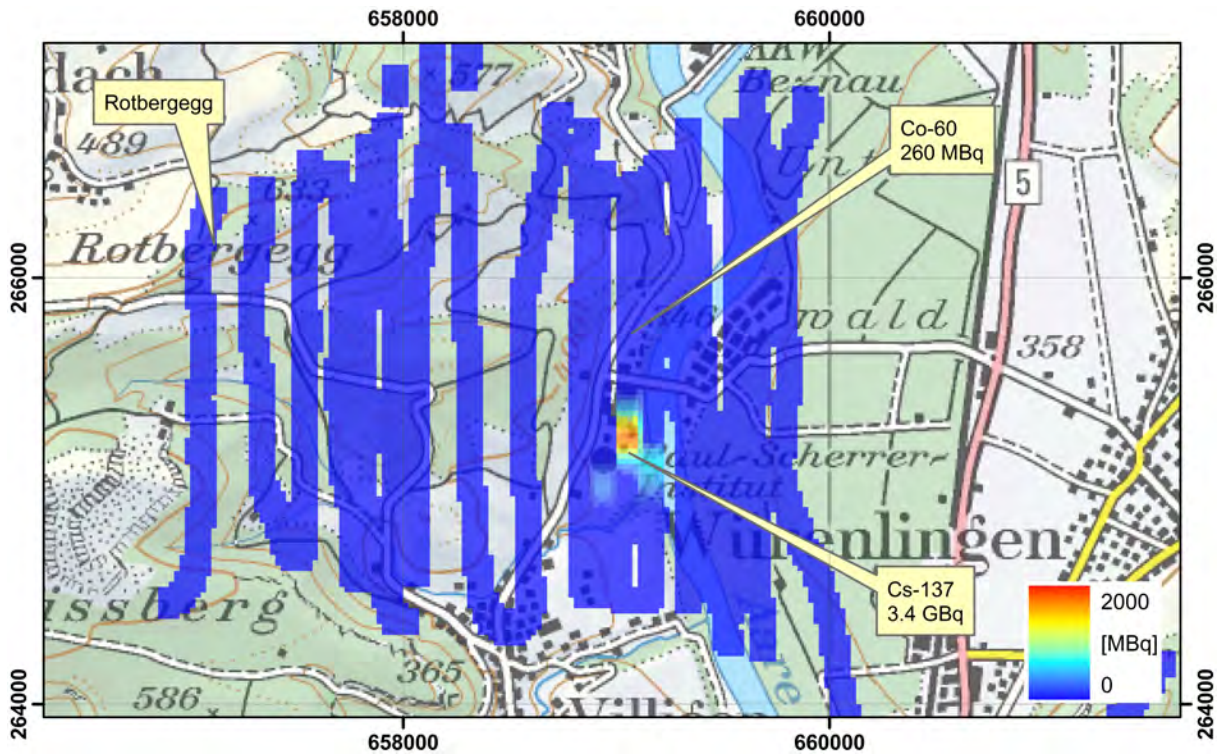
Figure 54: ^{137}Cs-point source activity of the test measurements over the vicinity of PSI measured with the RLL system.
PK100 ©2016 swisstopo (JD100042).
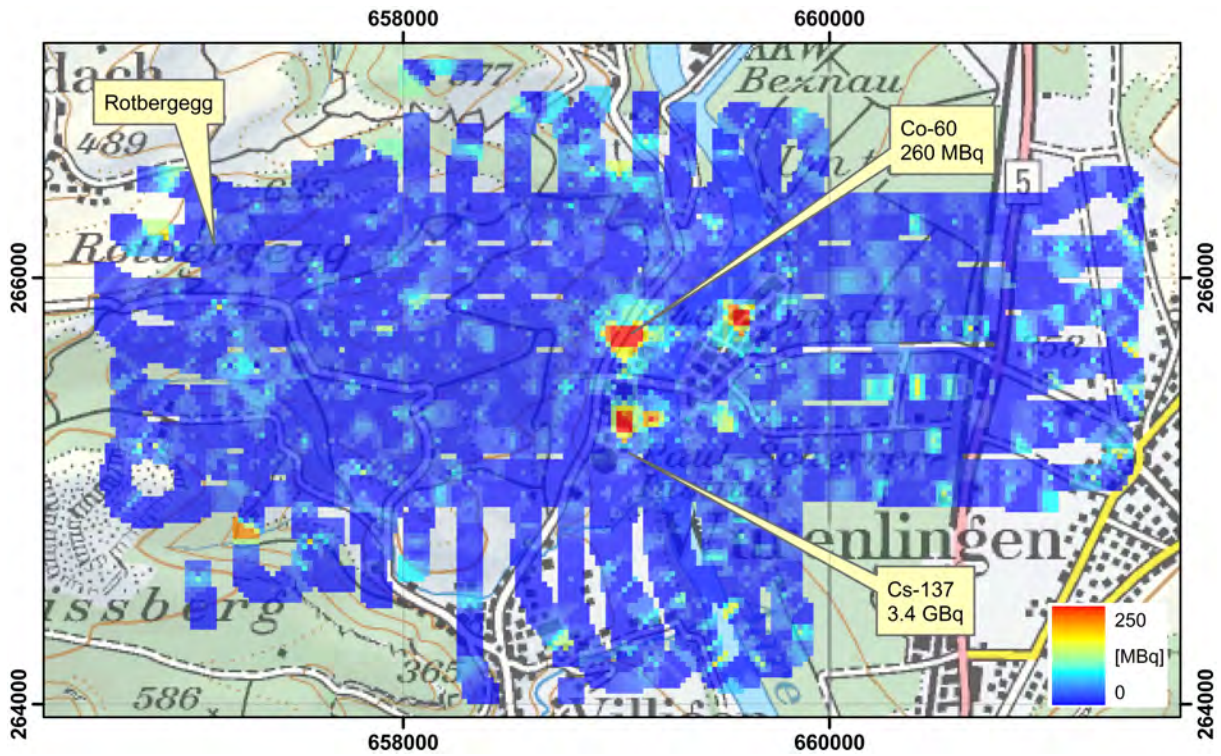
Figure 55: ^{60}Co-point source activity of the test measurements over the vicinity of PSI measured with the ARM system.
PK100 ©2016 swisstopo (JD100042).
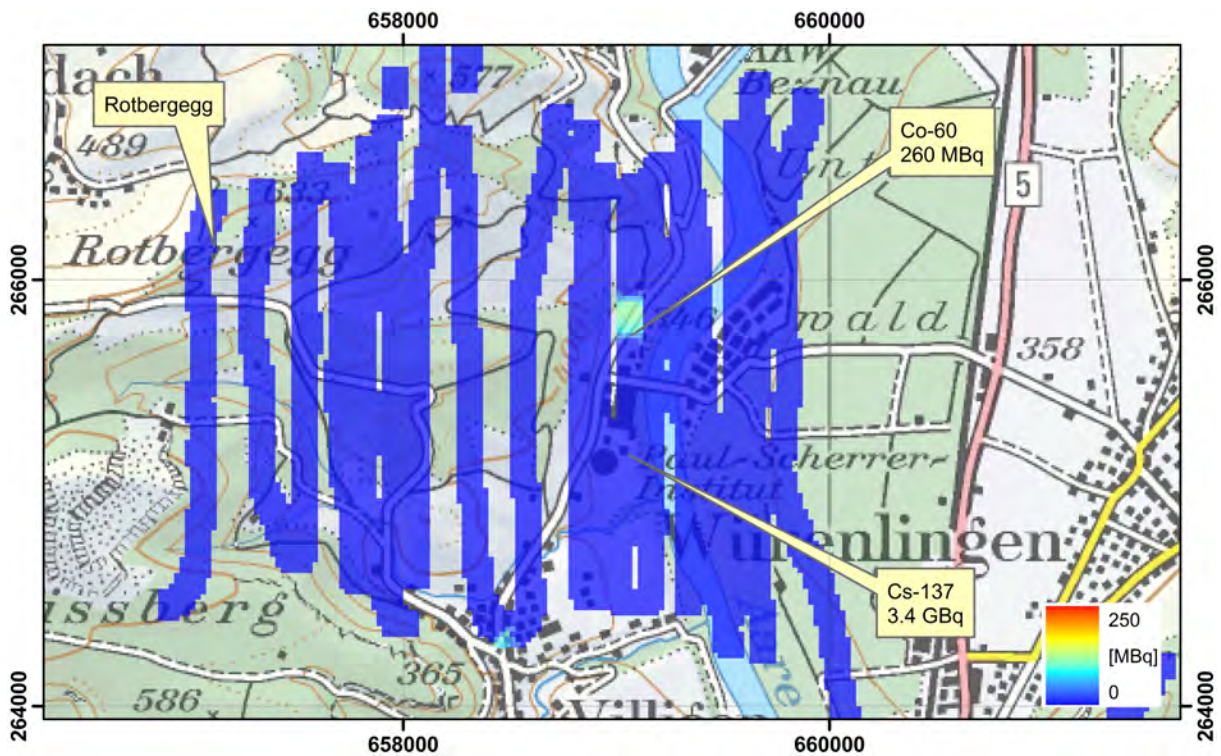
Figure 56: ^{60}Co-point source activity of the test measurements over the vicinity of PSI measured with the RLL system.
PK100 ©2016 swisstopo (JD100042).
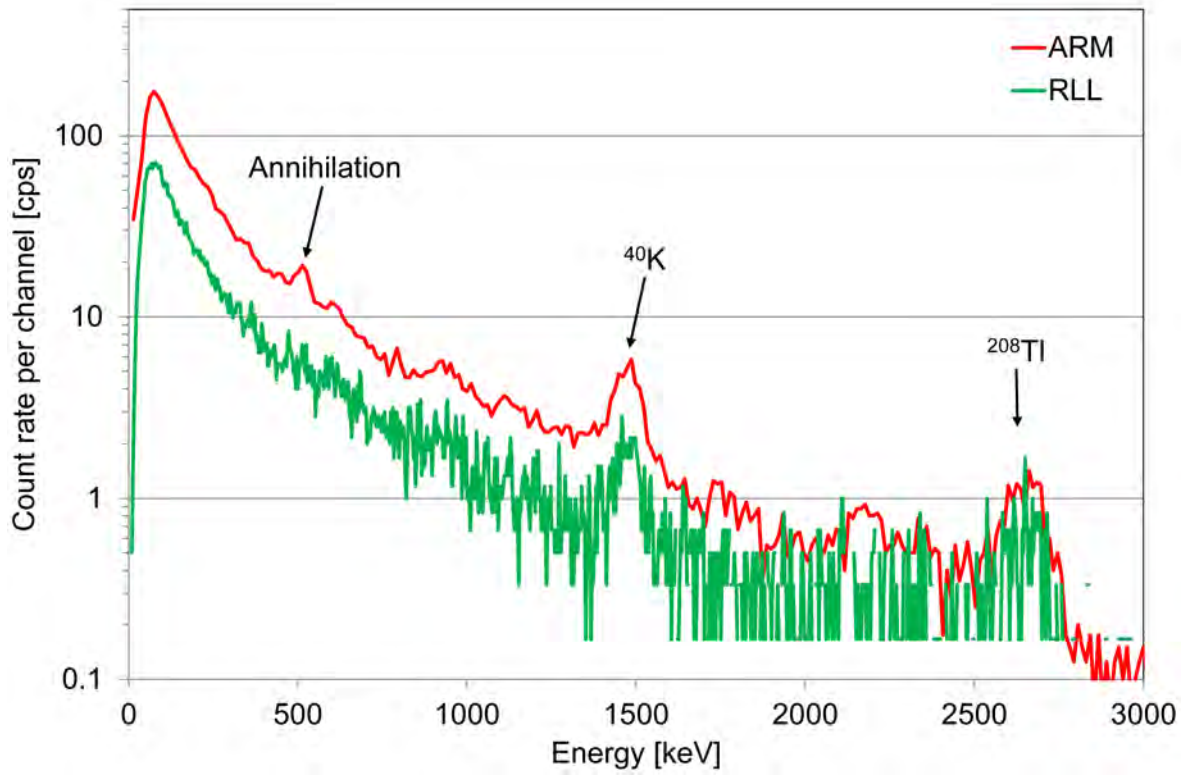
Figure 57: Photon spectra over areas with normal background radiation.
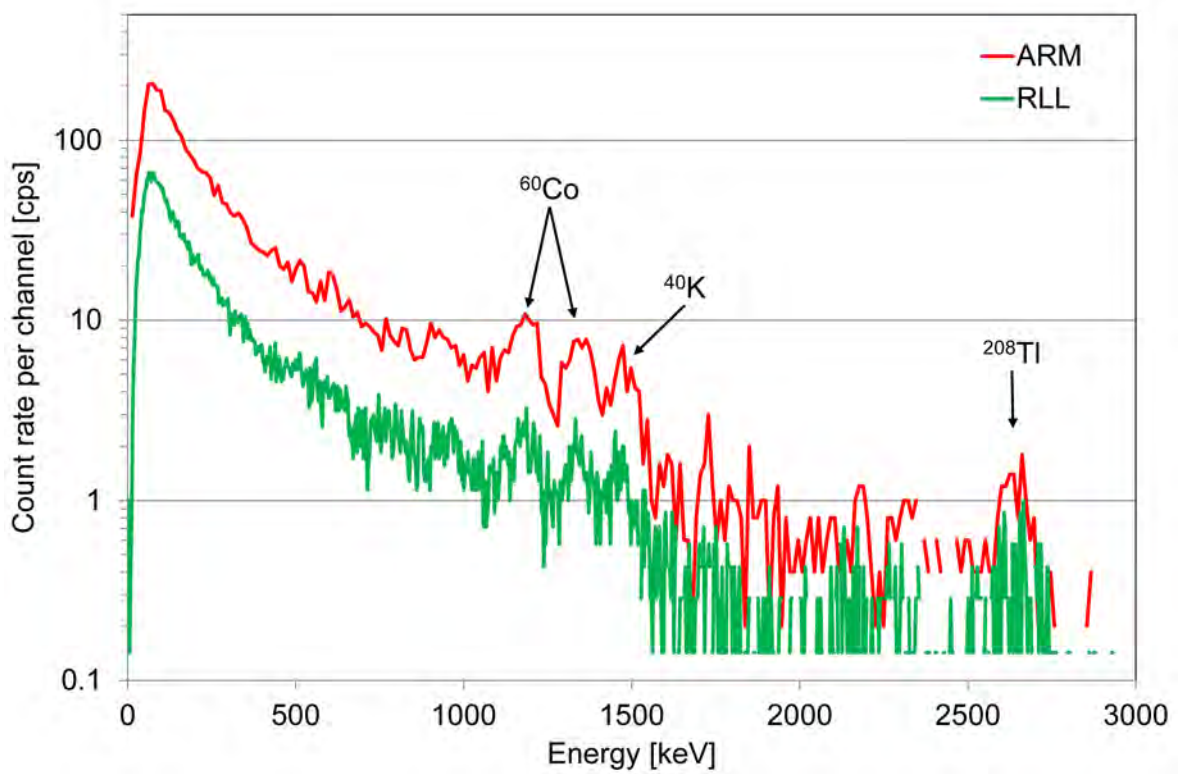
Figure 58: Photon spectra over the ^{60}Co-point source.
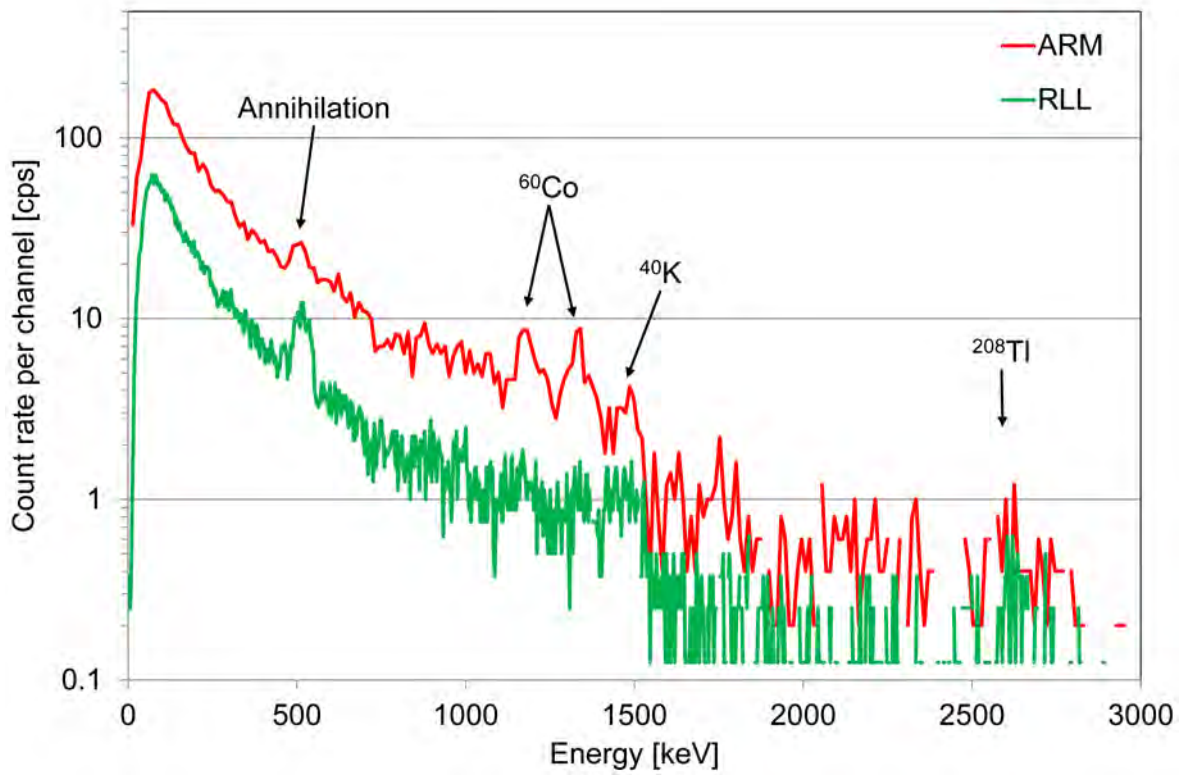
Figure 59: Photon spectra over a storage building at PSI East.
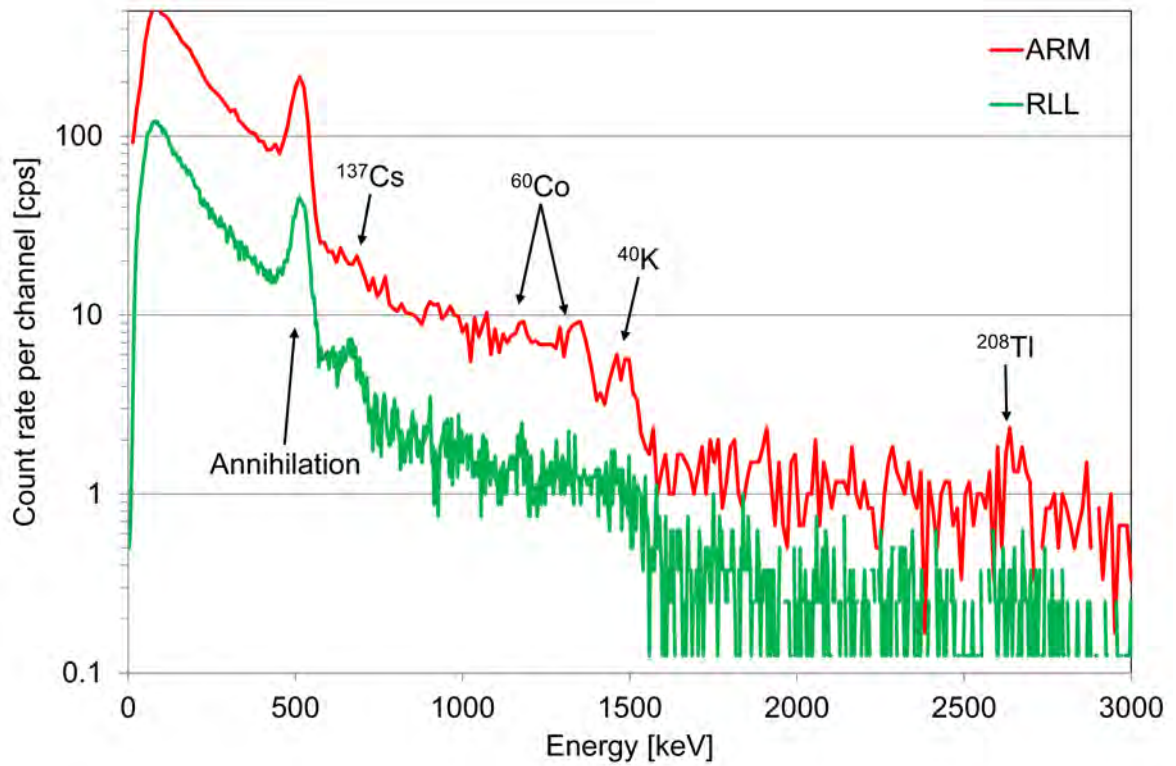
Figure 60: Photon spectra over the accelerator building.

50
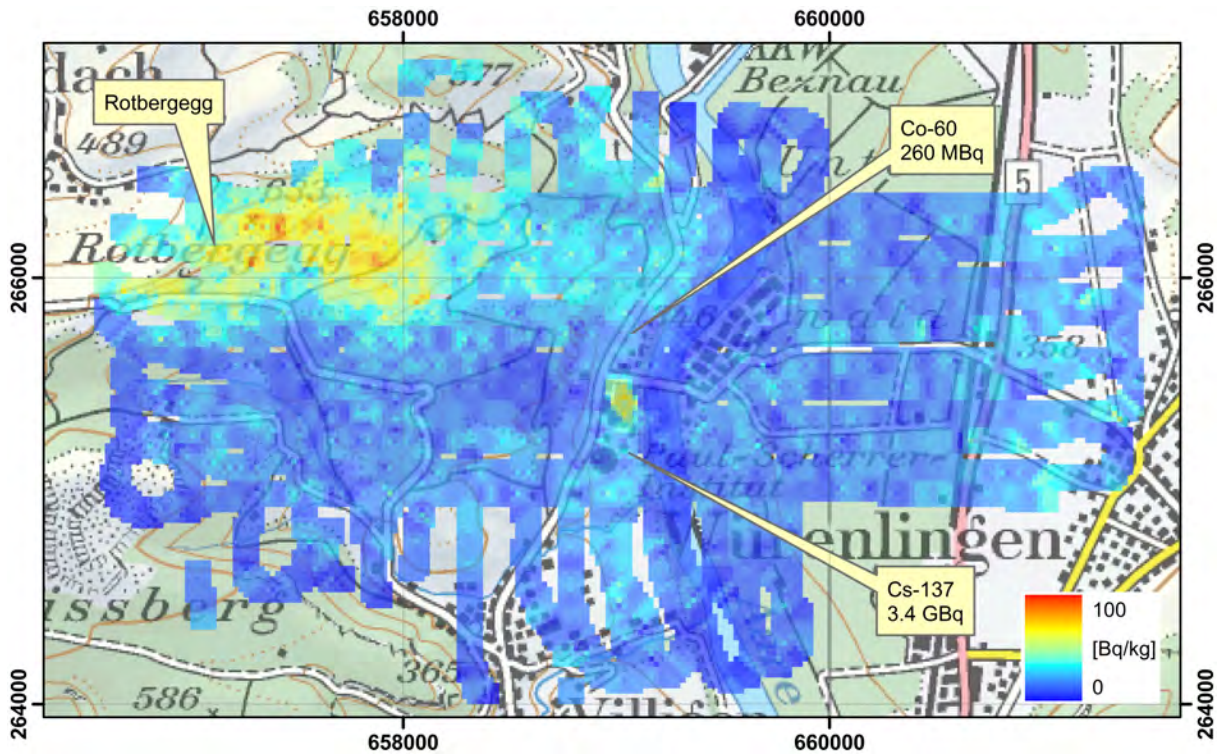
Figure 61: ^{232}Th activity concentration over the vicinity of PSI measured with the ARM system.
PK100 ©2016 swisstopo (JD100042).
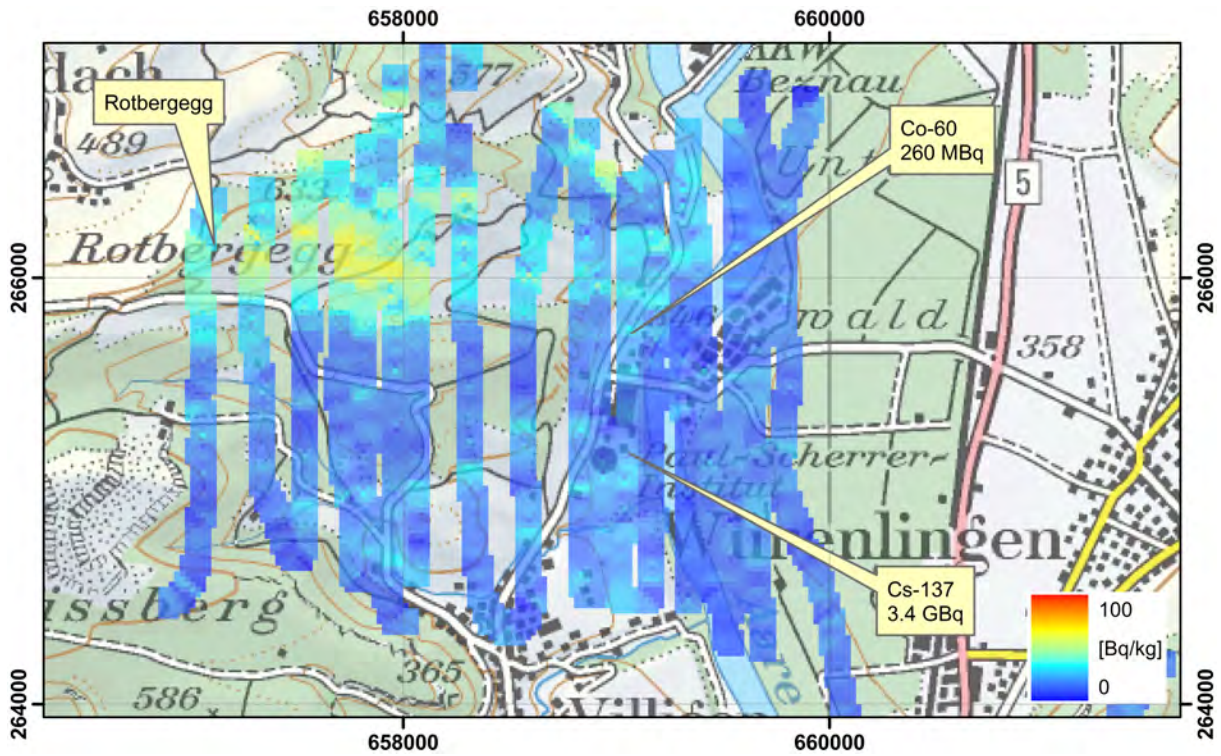
Figure 62: ^{232}Th activity concentration over the vicinity of PSI measured with the RLL system.
PK100 ©2016 swisstopo (JD100042).
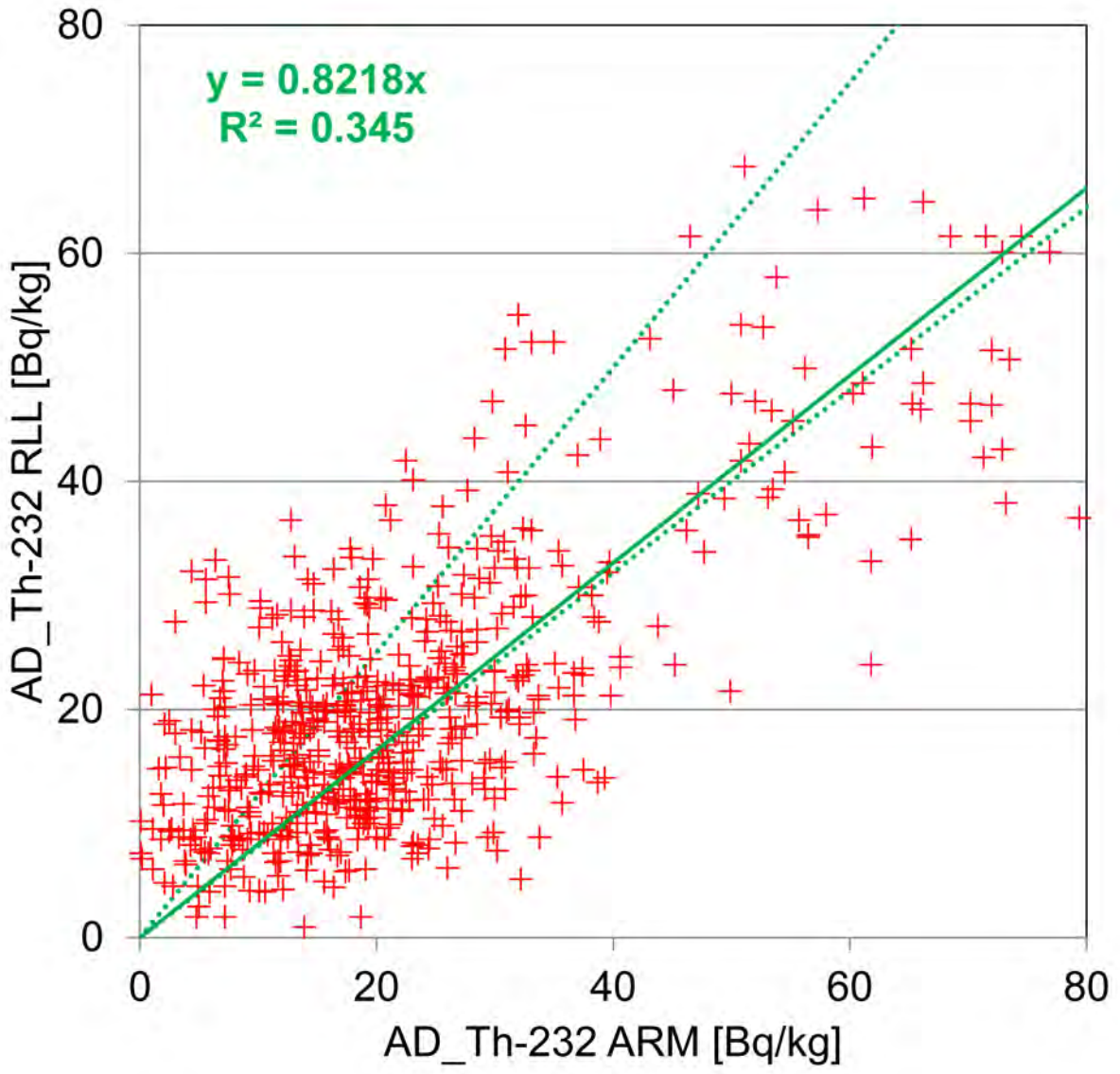
Figure 63: Scattergram of [232]Th activity concentrations measured with ARM and RLL systems. The solid green line represents proportionality; the dotted green lines indicate a range of ±25% around a proportionality of 1.

3 Conclusions

The survey of the environs of the Swiss nuclear power plants Beznau (KKB) and Leibstadt (KKL), the intermediate storage facility ZWILAG and the Paul Scherrer Institute showed no artificial radionuclides outside of the plant premises.

The measurements over the cities of Baar, Cham, Emmen, Luzern and Zug expanded the database of radiation background over Swiss cities. No unusual values of the radiological quantities were observed.

The location of a probe of the automated Swiss dose rate surveillance network NADAM with elevated readings was inspected both with the ARM and RLL system. The airborne measurements confirmed the readings of the NADAM probe and were able to associate the increased dose rate readings with elevated activity concentrations of natural radionuclides.

In the LAURA emergency exercise, the debris field of a plane crash including radioactive cargo was simulated at Emmen military airfield. Source search and retrieval was performed in cooperation with local first responders. The size of the exercise site was small relative to the field of view of the measuring system. Signals traceable to the placed radioactive source could be detected at all measured positions over the exercise area. Nevertheless, the location of a ^{137}Cs-source and several ^{60}Co-sources could be narrowed down and the summed source activity of each nuclide was estimated. A ^{99m}Tc-source with an activity of 100 MBq was not detected.

Several flights were dedicated to tests of the data evaluation and the associated parameters. The results showed that the parameters and algorithms of background, altitude and topographic corrections should be reviewed. A prerequisite to this review is the implementation of an adequate quantification of airborne radon decay products.

Comparison flights with the ARM and RLL systems showed good agreement for the derived dose rate values. The calibration of nuclide specific quantities should be further consolidated. The zeroing of values below the decision threshold performed by the RLL software should be reconsidered. The software used for the evaluation of the ARM raw data should be adapted to the raw data stored in the RLL system for extended analysis of the measurements. A prerequisite for this adaption is the determination of stripping correction factors for the RLL detectors using laboratory measurements.

4 Literature

Schwarz, G. F.: Methodische Entwicklungen zur Aerogammaspektrometrie. Beiträge zur Geologie der Schweiz, Geophysik Nr. 23, Schweizerische Geophysikalische Kommission, 1991.

Rybach, L., Schwarz, G. F. and Medici, F.: Construction of radioelement and dose-rate baseline maps by combining ground and airborne radiometric data. IAEA-Tecdoc-980, 33-44, Vienna, 1996.

Schwarz, G.F., Rybach, L. and Klingelé, E.: Design, calibration and application of an airborne gamma spectrometric system in Switzerland. Geophysics 62, 1369-1378, 1997.

Bucher, B.: Methodische Weiterentwicklungen in der Aeroradiometrie. Dissertation Nr. 13973, ETH Zürich, 2001.

Butterweck, G. and Bucher B.: Evaluation of the intercomparison flights of March 18th 2015 with airborne gamma-spectrometry systems ARM and RLL, TM 96-15-08, Paul Scherrer Institut, 2015.

5 Previous reports

Schwarz, G. F., Klingelé, E. E., Rybach, L.: Aeroradiometrische Messungen in der Umgebung der schweizerischen Kernanlagen. Bericht für das Jahr 1989 zuhanden der Hauptabteilung für die Sicherheit der Kernanlagen (HSK). Interner Bericht, Institut für Geophysik, ETH Zürich, 1990.

Schwarz, G. F., Klingelé, E. E., Rybach, L.: Aeroradiometrische Messungen in der Umgebung der schweizerischen Kernanlagen. Bericht für das Jahr 1990 zuhanden der Hauptabteilung für die Sicherheit der Kernanlagen (HSK). Interner Bericht, Institut für Geophysik, ETH Zürich, 1991.

Schwarz, G. F., Klingelé, E. E., Rybach, L.: Aeroradiometrische Messungen in der Umgebung der schweizerischen Kernanlagen. Bericht für das Jahr 1991 zuhanden der Hauptabteilung für die Sicherheit der Kernanlagen (HSK). Interner Bericht, Institut für Geophysik, ETH Zürich, 1992.

Schwarz, G. F., Klingelé, E. E., Rybach, L.: Aeroradiometrische Messungen in der Umgebung der schweizerischen Kernanlagen. Bericht für das Jahr 1992 zuhanden der Hauptabteilung für die Sicherheit der Kernanlagen (HSK). Interner Bericht, Institut für Geophysik, ETH Zürich, 1993.

Schwarz, G. F., Klingelé, E. E., Rybach, L.: Aeroradiometrische Messungen in der Umgebung der schweizerischen Kernanlagen. Bericht für das Jahr 1993 zuhanden der Hauptabteilung für die Sicherheit der Kernanlagen (HSK). Interner Bericht, Institut für Geophysik, ETH Zürich, 1994.

Schwarz, G. F., Rybach, L.: Aeroradiometrische Messungen im Rahmen der Übung ARM94. Bericht für das Jahr 1994 zuhanden der Fachgruppe Aeroradiometrie (FAR). Interner Bericht, Institut für Geophysik, ETH Zürich, 1995.

Schwarz, G. F., Rybach, L.: Aeroradiometrische Messungen im Rahmen der Übung ARM95. Bericht für das Jahr 1995 zuhanden der Fachgruppe Aeroradiometrie (FAR). Interner Bericht, Institut für Geophysik, ETH Zürich, 1996.

Schwarz, G. F., Rybach, L., Bärlocher, C.: Aeroradiometrische Messungen im Rahmen der Übung ARM96. Bericht für das Jahr 1996 zuhanden der Fachgruppe Aeroradiometrie (FAR). Interner Bericht, Institut für Geophysik, ETH Zürich, 1997.

Bucher, B., Rybach, L., Schwarz, G., Bärlocher, C.: Aeroradiometrische Messungen im Rahmen der Übung ARM97. Bericht für das Jahr 1997 zuhanden der Fachgruppe Aeroradiometrie (FAR). Interner Bericht, Institut für Geophysik, ETH Zürich, 1998.

Bucher, B., Rybach, L., Schwarz, G., Bärlocher, C.: Aeroradiometrische Messungen im Rahmen der Übung ARM98. Bericht für das Jahr 1998 zuhanden der Fachgruppe Aeroradiometrie (FAR). Interner Bericht, Institut für Geophysik, ETH Zürich, 1999.

Bucher, B., Rybach, L., Schwarz, G., Bärlocher, C.: Aeroradiometrische Messungen im Rahmen der Übung ARM99. Bericht für das Jahr 1999 zuhanden der Fachgruppe Aeroradiometrie (FAR). Interner Bericht, Institut für Geophysik, ETH Zürich, 2000.

Bucher, B., Rybach, L., Schwarz, G., Bärlocher, C.: Aeroradiometrische Messungen im Rahmen der Übung ARM00. Bericht für das Jahr 2000 zuhanden der Fachgruppe Aeroradiometrie (FAR). Interner Bericht, Institut für Geophysik, ETH Zürich, 2001.

Bucher, B., Rybach, L., Schwarz, G., Bärlocher, C.: Aeroradiometrische Messungen im Rahmen der Übung ARM01. Bericht für das Jahr 2001 zuhanden der Fachgruppe Aeroradiometrie (FAR). Interner Bericht, Paul Scherrer Institut, Villigen, Schweiz, 2002.

Bucher, B., Rybach, L., Schwarz, G., Bärlocher, C.: Aeroradiometrische Messungen im Rahmen der Übung ARM02. Bericht für das Jahr 2002 zuhanden der Fachgruppe Aeroradiometrie (FAR). Interner Bericht, Paul Scherrer Institut, Villigen, Schweiz, 2003.

Bucher, B., Rybach, L., Schwarz, G.: Aeroradiometrische Messungen im Rahmen der Übung ARM03. PSI-Bericht 04-14, ISSN 1019-0643, Paul Scherrer Institut, Villigen, Schweiz, 2004.

Bucher, B., Butterweck, G., Rybach, L., Schwarz, G.: Aeroradiometrische Messungen im Rahmen der Übung ARM04. PSI-Bericht 05-10, ISSN 1019-0643, Paul Scherrer Institut, Villigen, Schweiz, 2005.

Bucher, B., Butterweck, G., Rybach, L., Schwarz, G.: Aeroradiometrische Messungen im Rahmen der Übung ARM05. PSI-Bericht 06-06, ISSN 1019-0643, Paul Scherrer Institut, Villigen, Schweiz, 2006.

Bucher, B., Butterweck, G., Rybach, L., Schwarz, G.: Aeroradiometrische Messungen im Rahmen der Übung ARM06. PSI-Bericht 07-02, ISSN 1019-0643, Paul Scherrer Institut, Villigen, Schweiz, 2007.

Bucher, B., Guillot, L., Strobl, C., Butterweck, G., Gutierrez, S., Thomas, M., Hohmann, C., Krol, I., Rybach, L., Schwarz, G.: International Intercomparison Exercise of Airborne Gammaspectrometric Systems of Germany, France and Switzerland in the Framework of the Swiss Exercise ARM07. PSI-Bericht Nr. 09-07, ISSN 1019-0643, Paul Scherrer Institut, Villigen, Schweiz, 2009.

Bucher, B., Butterweck, G., Rybach, L., Schwarz, G.: Aeroradiometrische Messungen im Rahmen der Übung ARM08. PSI-Bericht Nr. 09-02, ISSN 1019-0643, Paul Scherrer Institut, Villigen, Schweiz, 2009.

Bucher, B., Butterweck, G., Rybach, L., Schwarz, G., Strobl, C.: Aeroradiometrische Messungen im Rahmen der Übung ARM09. PSI-Bericht Nr. 10-01, ISSN 1019-0643, Paul Scherrer Institut, Villigen, Schweiz, 2010.

Bucher, B., Butterweck, G., Rybach, L., Schwarz, G., Mayer, S.: Aeroradiometrische Messungen im Rahmen der Übung ARM10. PSI-Bericht Nr. 11-02, ISSN 1019-0643, Paul Scherrer Institut, Villigen, Schweiz, 2011.

Bucher, B., Butterweck, G., Rybach, L., Schwarz, G., Mayer, S.: Aeroradiometric Measurements in the Framework of the Swiss Exercise ARM11. PSI-Report No. 12-04, ISSN 1019-0643, Paul Scherrer Institut, Villigen, Switzerland, 2012.

Butterweck, G., Bucher, B., Rybach, L., Schwarz, G., Hödlmoser, H., Mayer, S., Danzi, C. Scharding, G.: Aeroradiometric Measurements in the Framework of the Swiss Exercise ARM12. PSI-Report No. 13-01, ISSN 1019-0643, Paul Scherrer Institut, Villigen, Switzerland, 2013.

Butterweck, G., Bucher, B., Rybach, L., Schwarz, G., Hohmann, E., Mayer, S., Danzi, C. Scharding, G.: Aeroradiometric Measurements in the Framework of the Swiss Exercise ARM13. PSI-Report No. 15-01, ISSN 1019-0643, Paul Scherrer Institut, Villigen, Switzerland, 2015.

Butterweck, G., Bucher, B., Rybach, L., Schwarz, G., Hohmann, E., Mayer, S., Danzi, C. Scharding, G.: Aeroradiometric Measurements in the Framework of the Swiss Exercises ARM14 and FTX14. PSI-Report No. 15-02, ISSN 1019-0643, Paul Scherrer Institut, Villigen, Switzerland, 2015.

Butterweck, G., Bucher, B., Rybach, L., Schwarz, G., Hofstetter-Boillat, B., Hohmann, E., Mayer, S., Danzi, C. Scharding, G.: Aeroradiometric Measurements in the Framework of the Swiss Exercises ARM15, GNU15 and the International Exercise AGC15. PSI-Report No. 15-04, ISSN 1019-0643, Paul Scherrer Institut, Villigen, Switzerland, 2015.

The reports since 1994 can be found and downloaded from the FAR website `http://www.far.ensi.ch`.

6 Evaluation parameter files

The parameter files used for the evaluation of raw data in this report are listed below to improve the traceability of the presented results. The detector definition files have been re-evaluated for all detectors in 2014. A software modification was performed to take into account different formats of terrain model files used for topographic correction, leading to a change in the detector definition file.

6.1 DefinitionFile_Processing_ch.txt

This file defines the standard parameters used for the gridding of measured data used througout this report.

```
Definition file Swiss MGS32
"Windows"
10
Total    401.   2997.      0.   0
K-40    1369.   1558.   1460.   1
U-238   1664.   1853.   1765.   1
Th-232  2407.   2797.   2615.   1
Cs-137   600.    720.    660.   2
Co-60   1100.   1400.      0.   2
MMGC1    400.   1400.      0.   0
MMGC2   1400.   2997.      0.   0
LOW       40.    720.      0.   0
MID      720.   2997.      0.   0
"Ratios"
3
MMGCVerhältnis   MMGC1  MMGC2  Ratio_MMGC
LOWHigh          LOW    MMGC2  RatioLowHigh
LowMid           LOW    MID    RatioLowMid
"Conversion factors Activity to Dose Rate"
8
Total       0        NoCalibration   "    "   0
AD_K-40     0.044    DHSR            "nSv/h"  1
AD_U-238    0.55     DHSR            "nSv/h"  1
AD_Th-232   0.77     DHSR            "nSv/h"  1
AD_Cs-137   0.2      DHSR            "nSv/h"  2
Co-60       0        NoCalibration   "    "   0
MMGC1       0        NoCalibration   "    "   0
MMGC2       0        NoCalibration   "    "   0
"Typ des Darstellungsgrenzwertes"
1
Nachweistyp  0
"counts of spectra to stack"
1
Counts 1
"Auszugebende Werte"
```

```
30
"DHSR TOT            ","DHSR_TOT","nSv/h        ",0.00,250.00
"AP_Co-60            ","AP_Co-60","MBq          ",0.00,150.00
"AP_Cs-137           ","AP_Cs-137","MBq          ",0.00,40.00
"Terr. DL            ","DHSR_TOT","nSv/h         ",0.00,250.00
"CR_Caesium          ","CR_Cs-137","cps          ",20.00,120.00
"CR_Cobalt           ","CR_Co-60","cps           ",0.00,100.00
"NR_Caesium          ","NR_Cs-137","cps          ",0.00,120.00
"NR_Cobalt           ","NR_Co-60","cps           ",0.00,100.00
"Total_CR_corr       ","NR_Total","cps           ",200.00,1200.00
"K-40                ","AD_K-40","Bq/kg         ",0.00,1000.00
"U-238               ","AD_U-238","Bq/kg         ",0.00,120.00
"Th-232              ","AD_Th-232","Bq/kg         ",0.00,120.00
"Cs-137              ","AD_Cs-137","Bq/kg         ",0.00,240.00
"Cobalt_CR           ","NR_Co-60","cps           ",0.00,120.00
"Nat.Terr.DL         ","DHSR_NAT","nSv/h         ",0.00,250.00
"Künst.DL            ","DHSR_ANT","nSv/h         ",0.00,250.00
"MMGC_Ratio          ","&MMGC_Ratio","%          ",4.00,6.00
"Cosmic DL           ","DHSR_COS","nSv/h         ",20.00,60.00
"Cosmic              ","CR_COS","cps            ",000.00,400.00
"Radar               ","PH","m             ",0.00,300.00
"ODL                 ","DHSR","nSv/h          ",0.00,250
"AD_UT_K-40          ","AD_UT_K-40","Bq/kg        ",0.00,200
"AD_UT_U-238         ","AD_UT_U-238","Bq/kg         ",0.00,50
"AD_UT_Th-232        ","AD_UT_Th-232","Bq/kg         ",0.00,40
"AD_UT_Cs-137        ","AD_UT_Cs-137","Bq/kg         ",0.00,20
"Err_Co-60           ","NR_UT_Co-60","cps          ",0.00,40
"Nachweis_Cs-137     ","CR_LD_Cs-137","cps          ",0.00,100.00
"Nachweis_Co-60      ","CR_LD_Co-60","cps           ",0.00,100.00
"Cs-137 beta=0       ","AA_Cs-137","Bq/m2         ",0.00,20000.00
"AA_UT_Cs-137        ","AA_UT_Cs-137","Bq/m2        ",0.00,20
```

6.2   Processing_Quellensuche.txt

This file defines the parameters used for a source search.

```
Definition file Swiss MGS32
"Windows"
10
Total    401.   2997.      0.   0
K-40    1369.   1558.   1460.   1
U-238   1664.   1853.   1765.   1
Th-232  2407.   2797.   2615.   1
Cs-137   600.    720.    660.   2
Co-60   1100.   1400.      0.   2
MMGC1    400.   1400.      0.   0
MMGC2   1400.   2997.      0.   0
```

```
LOW         40.      720.       0.    0
MID        720.     2997.       0.    0
"Ratios"
3
MMGCVerhältnis    MMGC1    MMGC2   Ratio_MMGC
LOWHigh           LOW      MMGC2   RatioLowHigh
LowMid            LOW      MID     RatioLowMid
"Conversion factors Activity to Dose Rate"
8
Total        0         NoCalibration    "      "   0
AD_K-40          0.044    DHSR             "nSv/h"   1
AD_U-238         0.55     DHSR             "nSv/h"   1
AD_Th-232        0.77     DHSR             "nSv/h"   1
AD_Cs-137        0.2      DHSR             "nSv/h"   2
Co-60        0         NoCalibration    "      "   0
MMGC1        0         NoCalibration    "      "   0
MMGC2        0         NoCalibration    "      "   0
"Typ des Darstellungsgrenzwertes"
1
Nachweistyp  0
"counts of spectra to stack"
1
Counts 1
"Auszugebende Werte"
30
"DHSR TOT            ","DHSR_TOT","nSv/h         ",0.00,250.00
"AP_Co-60            ","AP_Co-60","MBq           ",0.00,150.00
"AP_Cs-137           ","AP_Cs-137","MBq          ",0.00,40.00
"Terr. DL            ","DHSR_TOT","nSv/h         ",0.00,250.00
"CR_Caesium          ","CR_Cs-137","cps          ",20.00,120.00
"CR_Cobalt           ","CR_Co-60","cps           ",0.00,100.00
"NR_Caesium          ","NR_Cs-137","cps          ",0.00,120.00
"NR_Cobalt           ","NR_Co-60","cps           ",0.00,100.00
"AP_UT_Cs-137        ","AP_UT_Cs-137","MBq        ",0.00,5000.00
"K-40                ","AD_K-40","Bq/kg          ",0.00,1000.00
"U-238               ","AD_U-238","Bq/kg         ",0.00,120.00
"Th-232              ","AD_Th-232","Bq/kg         ",0.00,120.00
"Cs-137              ","AD_Cs-137","Bq/kg         ",0.00,240.00
"Cobalt_CR           ","NR_Co-60","cps           ",0.00,120.00
"Nat.Terr.DL         ","DHSR_NAT","nSv/h         ",0.00,250.00
"Künst.DL            ","DHSR_ANT","nSv/h         ",0.00,250.00
"MMGC_Ratio          ","&MMGC_Ratio","%          ",4.00,6.00
"Cosmic DL           ","DHSR_COS","nSv/h         ",20.00,60.00
"Cosmic              ","CR_COS","cps            ",000.00,400.00
"Radar               ","PH","m                   ",0.00,300.00
"ODL                 ","DHSR","nSv/h            ",0.00,250
"AD_UT_K-40          ","AD_UT_K-40","Bq/kg       ",0.00,200
"AD_UT_U-238         ","AD_UT_U-238","Bq/kg      ",0.00,50
"AD_UT_Th-232        ","AD_UT_Th-232","Bq/kg     ",0.00,40
```

```
"AD_UT_Cs-137        ","AD_UT_Cs-137","Bq/kg     ",0.00,20
"AP_UT_Co-60         ","AP_UT_Co-60","MBq       ",0.00,1000
"Nachweis_Cs-137     ","CR_LD_Cs-137","cps       ",0.00,100.00
"Nachweis_Co-60      ","CR_LD_Co-60","cps       ",0.00,100.00
"Cs-137 beta=0       ","AA_Cs-137","Bq/m2     ",0.00,20000.00
"AA_UT_Cs-137        ","AA_UT_Cs-137","Bq/m2     ",0.00,20
```

6.3 DefinitionFile_DetD.txt

This file defines the parameter set used for detector D.

```
Definition file System
"Koordinaten"
WGS84
"Non-linearity"
4
a0  1.8745
a1  0.082009
a2  0.00000012708
a3  0.0
"Recorder old RDT-Files"
8
Radar  0.00    -61.00
Baro   0.74    457.14
Cosm   0.00    1.00
Dead   5.00    0.00
Time   0.00    1.00
Temp   0.00    1.00
Pitch  0.00    76.20
Roll   0.00    90.91
"Background/Cosmic"
10
Total      98.1000      1.041       0.032
K-40       12.100       0.050       0.004
U-238       2.700       0.043       0.002
Th-232      3.400       0.044       0.001
Cs-137     15.500       0.102       0.005
Co-60      13.900       0.100       0.004
MMGC1      79.540       0.771       0.019
MMGC2      18.500       0.270       0.007
LOW         0.          0.          0.
MID         0.          0.          0.
"Stripping Coefficients"
10
1.000  0.000  0.000  0.000  0.000  0.000  0.000  0.000  0.000  0.000
0.000  1.000  1.025  0.461  0.000  0.106  0.000  0.000  0.000  0.000
0.000 -0.029  1.000  0.347  0.000  0.004  0.000  0.000  0.000  0.000
```

```
0.000 -0.020  0.055  1.000  0.000  0.002  0.000  0.000  0.000  0.000
0.000  0.328  3.235  1.604  1.000  0.202  0.000  0.000  0.000  0.000
0.000  0.637  2.485  0.670  0.001  1.000  0.000  0.000  0.000  0.000
0.000  0.000  0.000  0.000  0.000  0.000  1.000  0.000  0.000  0.000
0.000  0.000  0.000  0.000  0.000  0.000  0.000  1.000  0.000  0.000
0.000  0.000  0.000  0.000  0.000  0.000  0.000  0.000  1.000  0.000
0.000  0.000  0.000  0.000  0.000  0.000  0.000  0.000  0.000  1.000
```
"Converted Stripping Coefficients Matrix"
10
```
1.000  0.000  0.000  0.000  0.000  0.000  0.000  0.000  0.000  0.000
0.000  1.042 -0.795 -0.133  0.000 -0.106  0.000  0.000  0.000  0.000
0.000  0.026  1.007 -0.358  0.000 -0.006  0.000  0.000  0.000  0.000
0.000  0.021 -0.067  1.016  0.000 -0.005  0.000  0.000  0.000  0.000
0.000 -0.310 -2.498 -0.488  1.000 -0.158  0.000  0.000  0.000  0.000
0.000 -0.742 -1.950  0.294 -0.001  1.085  0.000  0.000  0.000  0.000
0.000  0.000  0.000  0.000  0.000  0.000  1.000  0.000  0.000  0.000
0.000  0.000  0.000  0.000  0.000  0.000  0.000  1.000  0.000  0.000
0.000  0.000  0.000  0.000  0.000  0.000  0.000  0.000  1.000  0.000
0.000  0.000  0.000  0.000  0.000  0.000  0.000  0.000  0.000  1.000
```
"Sigma of Converted Stripping Coefficients Matrix"
10
```
0.000  0.000  0.000  0.000  0.000  0.000  0.000  0.000  0.000  0.000
0.000  0.000 -0.040 -0.017  0.000 -0.016  0.000  0.000  0.000  0.000
0.000  0.000  0.000 -0.028  0.000  0.000  0.000  0.000  0.000  0.000
0.000  0.000 -0.009  0.000  0.000  0.000  0.000  0.000  0.000  0.000
0.000 -0.080 -0.103 -0.037  0.000 -0.008  0.000  0.000  0.000  0.000
0.000 -0.140 -0.068  0.013  0.000  0.000  0.000  0.000  0.000  0.000
0.000  0.000  0.000  0.000  0.000  0.000  0.000  0.000  0.000  0.000
0.000  0.000  0.000  0.000  0.000  0.000  0.000  0.000  0.000  0.000
0.000  0.000  0.000  0.000  0.000  0.000  0.000  0.000  0.000  0.000
0.000  0.000  0.000  0.000  0.000  0.000  0.000  0.000  0.000  0.000
```
"Attenuation Coefficients"
10
```
Total       0.00600    1.00000    0.0003
K-40        0.00800    1.00000    0.0008
U-238       0.00550    1.00000    0.0114
Th-232      0.00600    1.00000    0.0044
Cs-137      0.01000    1.00000    0.0100
Co-60       0.00800    1.00000    0.0080
MMGC1       0.00600    1.00000    0.0060
MMGC2       0.00650    1.00000    0.0065
LOW         0.02000    1.00000    0.01
MID         0.01500    1.00000    0.005
```
"3D Attenuation Coefficients"
10
```
Total       0.00350    2.00000
K-40        0.00420    2.00000
U-238       0.00320    2.00000
Th-232      0.00350    2.00000
```

```
Cs-137      0.00800     2.00000
Co-60       0.00800     1.00000
MMGC1       0.00600     1.00000
MMGC2       0.00650     1.00000
LOW         0.02000     1.00000
MID         0.01500     1.00000
"Conversion factors Counts to Activity"
11
Total       0           NoCalibration    "       "
K-40        7.95        AD_K-40          "Bq/kg"
U-238       3.87        AD_U-238         "Bq/kg"
Th-232      1.62        AD_Th-232        "Bq/kg"
Cs-137      1.88        AD_Cs-137        "Bq/kg"
Cs-137      32.96       AA_Cs-137        "Bq/m2"
Cs-137      7.2         AP_Cs-137        "MBq  "
Co-60       2.5         AP_Co-60         "MBq  "
Co-60       0           NoCalibration    "       "
MMGC1       0           NoCalibration    "       "
MMGC2       0           NoCalibration    "       "
"Radon"
1
0           0
"Höhenkorrektur"
4
AltMethod    1
GroundAltDGM 1
DGMType      0
PfadDHM25    C:\DATEN\Benno\Aeroradiometrie\Daten\DHM25\
"SDI Constants"
7
Aten        0.0053
Convert     0.00096
CosmicKorr  95.5
Back        12640.0
Gain        12.0
referenz_alt 100.0
Threshold   240.0
```